An Analysis of Frictional Effects in Non-stationary Contact Problems for Metal Forming Simulations

KEVIN COLVILLE

A thesis presented for the degree of
Doctor of Philosophy

Department of Mathematics and Applied Mathematics
University of Cape Town
Republic of South Africa
2019

Acknowledgements

I would like to thank my supervisors: Dr Henri Laurie, University of Cape Town, for his guidance, help and patience; and Prof. Jacek Rońda (Dr.Sc.) of Akademia Górniczo-Hutnicza, Poland, for his advice and expertise, and support of this research from its start. Thanks are also owed to the anonymous referees who provided valuable feedback, especially the examiner whose 12 page report was initially daunting but was exceedingly helpful and improved this work.

Declaration

I, Kevin Colville, hereby declare that the work on which this thesis is based is my original work (except where acknowledgements indicate otherwise) and that neither the whole work nor any part of it has been, is being, or is to be submitted for another degree in this or any other university. I authorise the University to reproduce for the purpose of research either the whole or any portion of the contents in any manner whatsoever.

Abstract

The finite element method (FEM) is widely used for the simulation of metal forming processes and has been successfully used in contact problems which arise in processes such as deep-drawing, punching, extrusion and rolling. All these processes involve friction between the contact surfaces: the sheet-metal workpiece and the toolpieces. The model of friction is thus an important part of any simulation of metal forming processes. Most FEM codes use a friction model that assumes that the contact surface is a plane.

Attempts to address this problem have focused on the convective description of deformation, which has the advantage of being naturally extended to numerical methods like the FEM at the expense of additional computation and numerical complexity. The convective description is used in this work, which focuses on the numerical implementation of the objective measure.

The effects of the rotation of the material contact point is taken into account by including objective time derivatives of the slipping (tangential) direction function. The objective rate of the direction function includes the surface spin induced by the rigid motion of a contact point sliding over the tool surface, and the material spin occurring during the elastic-plastic deformation of the blank. This is introduced by adapting the incremental relations of the friction slip.

This thesis presents the results of numerical experiment to determine the influence that the rotation and convection of contact points has on the frictional stresses and slipping energy.

Four different friction models are implemented within the finite element program ABAQUS and applied to simulations of standard metal forming benchmark processes: the square-cup and s-rail deep drawing benchmarks of the Numisheet conferences, for which several experimental and numerical results are available to compare with the solution of a finite element simulation. The

results for each metal-forming simulation are calculated for different friction models, and are compared and a choice made as to which is the “best” friction model for the process. Further, the reverse problem of determining the values of friction parameters by comparison of simulation and experimental results is performed for these benchmark problems. As there is yet no ideal friction model for all processes that are modelled, finding the most appropriate friction model by numerical means is proposed to improve the quality of a simulation.

Contents

Chapter 1

Introduction

The finite element method (FEM) is widely used for the simulation of metal forming processes [26, 29]. It has been successfully used in contact problems which arise in processes such as deep-drawing, punching, extrusion and rolling. All these processes involve friction between the contact surfaces: the sheet-metal workpiece and the toolpieces. The toolpieces, being made of stiffer metal than the more ductile workpiece, are modelled by rigid surfaces and are considered the master surface in contact imposing a shape the deformable workpiece must conform to. The model of friction is thus an important part of any simulation of metal forming processes. Most FEM codes use a friction model based upon the 'elastic-plastic' model of Michalowski and Mroz [37]. This model, and all its variations, however, assumes that the contact surface is a plane. Usually, the tangent plane at the point of contact is used. This assumption is made for ease of calculation, especially within the FEM where contact occurs at discrete points, namely the between the nodes of the element mesh and the rigid surface of a toolpiece. Thus, the actual contact *surface* is not completely modelled, but is replaced by a set of contact points, with the contact surface used for calculation assumed to be the tangent plane

at each contact point. However, the contact surfaces are more complicated than that where the rigid bodies representing the toolpieces contain curved surfaces. These rigid surfaces are modelled by low order (linear flat) facets to higher order (cubic) parametric surfaces which retain the curvature to provide more accurate representation. The solution of the contact problem involves imposing the contact conditions on the deformable body which is moving over the tools.

Attempts to solve this problem have focused on the convected description of deformation [29, 31], which has the advantage of being naturally extended to numerical methods like the FEM. Klarbring [29] develops a formulation with objective measures of nearness (distance to contact) and tangential slip. Laursen [31] uses the Lie derivative to maintain frame indifference in the formulation of the contact conditions. A disadvantage of these approaches is the complications introduced by the formulations make the numerical implementation difficult and computationally expensive. The convective description is also followed here, but this new formulation uses the Jaumann objective derivative and focuses on the numerical implementation of the objective measure. This is similar to the model of Anand [3] which uses a co-rotational rate to formulate an objective model of friction.

The classical constitutive model of Amontons-Coulomb friction with the interpretation of Michalowski and Mroz is based on the 'elastic-plastic' analogy, and here is adapted to take into account the rotation of a point in the contact region.

The effects of the rotation of the material contact point is taken into account by including objective time derivatives of the slipping (tangential) direction function, $(\mathbf{T}_T/|\mathbf{T}_T|)(\mathbf{y})$, where the position vector of a contact point, $\mathbf{y} \in \Gamma_S$, can be measured in the current (Eulerian), $\mathbf{y} = \mathbf{x}$, or the reference (La-

grangian) configuration, $\mathbf{y} = \mathbf{X}$. The objective rate of the direction function includes the surface spin induced by the rigid motion of a contact point sliding over the tool surface, and the material spin occurring during the elastic-plastic deformation of the blank. This is introduced by adapting the incremental relations of the friction slip. Another approach to introducing a new time integration method is presented in [2].

This thesis presents the results of numerical experiment to determine the influence that the rotation and convection of contact points has on the frictional stresses and slipping energy.

1.1 Constitutive model

In most finite element method (FEM) programs friction is implemented by the classic Amontons-Coulomb model. This has undoubtedly led to low quality of results for some contact problems, for which the conditions on the contact surface can be a significant contribution to the solution of the entire problem. In this dissertation an attempt is made to rectify the situation by considering the implementation of different friction models in a FEM package.

Three different friction models are implemented using the standard convective formulation and the new corotational formulation within the finite element program ABAQUS (version 6.x), which allows a user to write a FORTRAN subroutine describing the frictional stresses, sliding and other properties on a point of contact between a rigid toolpiece, which defines the contact surface, and the deformable workpiece, which is discretised by finite elements. The friction subroutine will be called during the analysis of the whole problem. This feature allows existing simulations to be run with different friction models by only changing the aforementioned subroutine.

The simulations chosen were two standard benchmark processes: the square-cup and s-rail deep drawing benchmarks of the NUMISHEET '93 and NUMISHEET '96 conferences, respectively. These metal working processes all involve large plastic deformation over a tool and would thus be dependent on frictional effects. There has been much work published on these processes and experimental and numerical results are available ([56, 61]) to compare with the solution of a finite element simulation. Once results for a particular simulation are calculated for different friction models and they are compared, to identify which is the "best" friction model for the process. Further, the reverse problem of determining the values of friction parameters by comparison of simulation and experimental results can be performed. Friction models take into consideration different state variables and discovering which variables are significant for the forming process that is modelled would help improve the quality of its simulation.

The chosen problems were modelled within continuum mechanics using the updated Lagrangian formulation. The resulting equations of motion and boundary conditions were then cast in variational form and this could be discretised and solved numerically using the finite element method (FEM). To simplify the solution the tools were modelled as rigid bodies, and the work pieces were modelled as elastic-plastic materials.

Simulation of metal working problems requires the accurate modelling of the material behaviour and the interface conditions. The most difficult part of solving a contact problem is the determination of the contact surface and the stresses, forces and displacements on it. It is here that only a few papers have been published on including more realistic models of friction within the FEM. Most finite element programs utilise the classic Amontons-Coulomb model of friction.

1.2 Friction Phenomena

Research has been done in friction, both in physics (seeking the basic mechanisms) [9, 10, 65] and engineering (quantifying the effects on processes), and on the associated phenomena of abrasion and wear [30, 59]. Work has also been done on evaluating and describing the real surface of contact. This information, particularly mathematical models of friction, can be used to include new models of friction within the FEM.

By friction we mean the resistance to tangential motion experienced by two bodies in contact. We are concerned with describing this resistance as frictional forces or stresses on the contact surface. We also consider how this affects the relative tangential motion (sliding) on the contact surface. We will not consider the phenomena of wear.

Friction consists of several phenomena which contribute to the total frictional resistance. These will be mentioned briefly here, and those phenomena which are incorporated into the friction models studied will be described in detail in chapter 2.

Real surfaces are not smooth, but consist of asperities and valleys on the microscopic scale. The asperities are the main contributors to friction. When two surfaces come into contact this will occur on the peaks of asperities. As contact appears on isolated points, not over the whole surface, the real contact area will differ from the nominal contact area [30].

Adhesion takes place owing to the natural molecular attraction from van der Waals forces or chemical bonding, or from micro-welds as a result of the high pressures which develop over the small contact area between asperities. Adhesion depends on the strength of the bond and on the area of bonding. Friction would then arise from the stress needed to break a bond.

Asperities can interlock if the peak of one asperity lies in the valley of the other surface. This means that sliding could only occur if the asperities shear. Asperities that have bonded could also shear rather than break the bond. Thus, friction would arise from the shear strength of the materials.

Rather than shear, interlocking asperities could plough into the base material, deforming the shape of the surface. Then friction would arise from the work needed to deform the material plastically. Plowing and shearing would also result in separate pieces of material being deposited between the contacting surfaces. As this debris is usually much harder than the parent material owing to oxidation and/or work hardening, the debris contributes by ploughing into the main bodies. Friction then arises from surface cutting, plastic deformation and fracture.

The contacting asperities could deform into flatter shapes, smoothing the surfaces. This friction would result from elastic and plastic deformation of the asperities. A consequence of this is that the topology of the surface changes, affecting the real contact area and material properties.

The Amonton-Coulomb model uses a linear relationship between the contact stress and the frictional traction, up to a maximum value, $\tau_{\max} = \mu p$, determined by the contact pressure (normal component of the contact stress), $p = \sigma_N$ and the parameter μ. See Chapter 2 for details. In effect, μ summarizes the average resistance due to the interacting asperities, debris and surface properties. Use of a single parameter relies on several reasonable assumptions, but are a first order approximation of experimental observations. Coulomb made extensive experiments [46] which revealed several second-order effects but the simplicity of the single parameter is appealing as those additional dependencies are weaker and it is the most widely used friction model for metal-metal contact, for which it is a good approximation. In the

standard AC model μ is a constant but can be extended by including dependence on other state variables as described below.

The Levanov model [33] replaces the linear relationship between contact shear and frictional traction with a non-linear model avoiding the discontinuity at the maximum frictional traction as shown in the figure

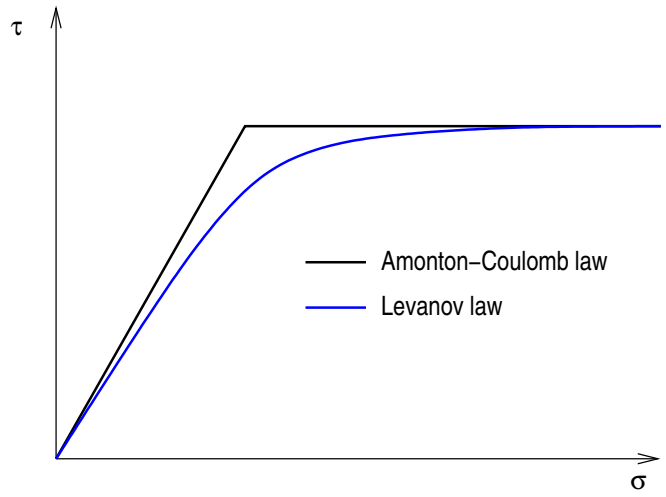

Removing the discontinuity has some attractable numerical properties which are of benefit for numerical convergence, at the expense of the slower exponential function calculation. Fortunately, modern computers have fast floating-point processors which can calculate e^x quickly in hardware (12 cycles *vs* 1 cycle for multiplication *vs* 30 cycles to load a variable from memory).

The first set of extensions of the AC model relate the frictional resistance to the material properties of the contacting bodies. Siebel's law [5] uses the shear strength of the material to determine the maximum frictional traction, in effect modelling the shearing of the contacting asperities in the thin contact layer, $\tau = m\sigma_c$, where σ_c is the shear yield limit within the contacting sub-layer and m is the friction factor (similar to μ) which depends on the contact

surface condition. The shortcoming is that this ignores frictional resistance from surface features, e.g., debris particles, that do not have the same shear properties as the body material.

For example, a more complex model using material properties can be derived from the surface interaction of two metal bodies under quasi-steady-state sliding [78]. Then, by combining the proportion of material deformation from asperity adhesion, asperity ploughing, and debris ploughing, the model is able to determine, assuming the interactions reach a steady-state, the frictional resistance from the material shear strengths, hardness, and the adhesive strength of micro-welded asperities. This has the advantage that μ can be calculated from known material properties which may make it more accurate. However, the model does rely on average areas of contact which have to be estimated as they are more difficult to derive from experimental data.

Wriggers, vu Van and Stein have proposed a friction model for use within finite element analysis with a nonlinear relation between the frictional yield function and the normal force between surfaces [76]. The WVS model (*qv.* Chapter 2) is derived from two empirical relationships: (1) between nominal and real contact areas; and (2) between shear stress and the contact pressure. The resultant model has three parameters and one non-linear term. The advantage of this model is that it accounts for the difference between nominal and effective contact area, however, the shortcoming is that this parameter is unknown and harder to estimate as it depends on the degree of polish of the surface finish. A natural extension of this model would be to account for dynamic smoothing during sliding, similarly to the WH model presented in Chapter 2.

The above description of surface interaction assumes that there is no lubricant between surfaces. The presence of a lubricant complicates matters

as the behaviour of the lubricant must be considered. In the case of a liquid lubricant we can model it using fluid dynamics provided the lubricant film is thick enough [13].

When the lubricant is thick enough to completely separate the surfaces so that there is no contact between asperities, then friction will be due to viscous shear within the fluid. The case when surface roughness effects are negligible is known as **thick film** lubrication. Then the smooth Reynolds equation is used to model the lubricant and provide a relationship between the thickness of the film and the contact pressure.

The case when the two surfaces are still completely separated, and the surface roughness effects are no longer small, the friction is due to viscous shear but this must be modified to account for the contribution of roughness. This is usually due to the change in fluid velocity near the asperities. This is known as **thin film** lubrication. The Reynolds equation can be modified to accommodate the average roughness of the surface [43].

The main disadvantage of including the lubricant in the thick and thin film cases is the need to make a separate computation to solve the Reynolds equation. This can can considerable complexity and time to the total solution of the simulation.

Should the lubricant be thin enough to allow asperity contacts, the phenomena described for dry friction will operate, as well as the fluid shear. Lubricant will tend to be trapped in valleys in the surfaces, and so limit the contact area from expanding under increasing pressure as the entrapped pools of lubricant support the normal load. A very thin boundary layer of lubricant will exist between some of the asperity contacts, and others will be dry. This is known as **mixed film** lubrication. The frictional stress is now composed of the contributions from viscous shear in the pools of entrapped lubricant, the

shear strength of the boundary film, and the frictional stress of the areas in dry contact [71].

When the film is very thin (a few molecules thick) and merely coats the surface asperities, there will be no pools of entrapped lubricant. Then the dry frictional phenomena will act along with the effect of the thin boundary film. This case is known as **boundary film** lubrication [70].

More advanced friction models, e.g. [72], have been proposed which take into account the above phenomena. These more realistic models consider the individual contribution of each separate interaction.

Most implementations of friction within the FEM have used the Coulomb model. Extensive work was done by Oden and Pires [38, 39, 40] and Kikuchi [26] within elasticity on nonlinear and non-local dry models of friction. However, these models have not proved as useful for simulating real contact. Other models of dry friction have been implemented by Wriggers, et al. [76], Peric and Owen [44], Rodic and Owen [49] and Buczkowski and Klieber [12]. All these have used a version of the plasticity formulations described below (section 1.3, coupled with empirical or theoretical relations for the frictional stresses and displacements. In chapter 2 a theoretical model of friction due to Zhang, et al. [78, 79] is incorporated within the FEM using the plasticity approach. It is thus possible to easily include new models of friction. For example, a new friction model which takes accounts the wear of the surface of coated steels by using a "work-hardening" type of model [45].

More advanced models which account for the change in the surface during forming have been recently proposed [24], where the changes to the surface micro-structure are modelled to determine the change to the frictional macro-state. This resulted in a more accurate physical model with improved numerical result when stretching occurred but not much change for simple

flattening of the micro-structure of the surface. The advantage of this model the smoothing or polishing effect of the sheet metal sliding over the harder toolpieces is calculated to determine the effective frictional coefficient. It is not clear that the proposed model has much advantage over the simpler WH model which also accounts for smoothing. There is a need for more models that can accurately describe smoothing effects as many products manufactured by deep-drawing require repeated formings (draw reductions) to achieve the final shape, for example, beverage cans, and the workpiece is polished by each step altering the friction.

Friction models with lubrication have been implemented within the FEM by Wilson, et al. [72, 74]. In [15] the Wilson model is described and implemented for two dimensional axisymmetric processes. There it was found that the increased computational time was not too large (on average 30% to 50% longer) but the improved accuracy of the simulation for deep-drawing made it worth while. However, for rolling, the improvement in accuracy was modest and not worth the additional time spent.

There are other FEM implementations of lubricated friction. Hol, *et al.* extended their micro-structure model [24] to include lubrication [25] and this more advanced friction model accounts for the change in surface topography and the evolution of friction in the boundary lubrication regime. The main weakness of this approach is that the accuracy of the boundary lubrication friction model depends on a proper determination of input parameters for which additional experiments are needed for every new work material and lubricant combination. The advantage of the extra work is that the work demonstrated that one can achieve greater predictive accuracy in simulation with this model.

The advantages of improving the realistic accuracy of the modelling must

be balanced by the increased computation time. It is for this reason that simpler models that accommodate the dominant effects are preferred as other effects display a weaker contribution to friction [46].

1.3 Friction and the Finite Element Method

The frictional contact problem is formulated as a minimisation problem, which is solved numerically by the FEM. Such a simulation of contact requires that the FEM include procedures and algorithms for determining: when and where contact occurs, the conditions of contact (stresses, displacements), and friction and other interface contributions (wear). Two approaches are used to include the contact constraints: Lagrange multipliers and penalty function methods. As contact algorithms are not the focus of this research report, it was decided to use an existing FEM package which can simulate contact problems. The FEM program ABAQUS [1] was chosen, which uses a Lagrange multiplier method.

Three models of friction in two formulations will be presented in this dissertation. Each model is coded in FORTRAN and implemented within ABAQUS. The models are tested by using each to solve a metal forming simulation. The results are compared in order to seek information on the most appropriate model for a particular manufacturing process.

The most successful approach to incorporating friction within the FEM is the "plasticity" theory of friction, which was proposed by Friedriksson, and also Michalowski and Mroz, and Curnier (see [16, 44]). This theory constructs an analogy between friction and plasticity from the similarities in Table 1.3.

The stick state of friction is comparable to the elastic state of elasto-plasticity

Friction	**Plasticity**
Decomposition of sliding into stick and slip	Decomposition of strain into elastic and plastic parts
Laws of stick and wear	Laws of elastic, kinematic and isotropic hardening
A slip criterion	A yield criterion
Slip rules	Yield rules

Table 1.1: Friction exhibits similar phenomena to plasticity.

as any displacement which occurs during sticking is owing to the elastic deformation of asperities. Similarly the slip state of friction is due partly to plastic deformation of asperities (and also debris particles, if present) and mostly due to the breaking of the bonds formed between contacting asperities.

The theory for the plasticity approach to friction will be presented in Chapter 2, along with the algorithms used. The algorithm that results from this approach is quite general, and can accommodate different models of friction which consider contact pressure, interface temperature, or work hardening and wear effects on the frictional stresses. The further advantage of this approach is that the numerical integration algorithms developed for plasticity can be used.

Chapter 2

Formulation of friction models

Notation

In this report scalars are represented by italic letters, vectors and second-order tensors are represented by bold letters. For ease of calculation, vectors will be considered to be column matrices and second-order tensors will be square matrices. Then the possible products are:

$$\begin{aligned}
\boldsymbol{A}\mathbf{x} &= A_{ij}x_j & \mathbf{x}^{\mathrm{t}}\boldsymbol{A} &= x_iA_{ij} & \mathbf{x}\cdot\mathbf{y} &= x_iy_i \\
\mathbf{x}\otimes\mathbf{y} &= x_iy_j & \boldsymbol{A}\boldsymbol{B} &= A_{ij}B_{jk} & \boldsymbol{A}{:}\boldsymbol{B} &= A_{ij}B_{ij} \\
& & \mathrm{Tr}\,\boldsymbol{A} &= A_{ii} &&
\end{aligned}$$

where repeated indices imply summation, and $\mathbf{x}^{\mathrm{t}}$ denotes the transpose of $\mathbf{x}$. When necessary tensor relations will be given in index notation for clarity.

2.1 Friction model description

2.1.1 Preliminaries

The initial configuration (material coordinates) of a body is denoted by **X**, and the current configuration by **x**. The displacement is then

$$\mathbf{u} = \mathbf{x} - \mathbf{X}. \tag{2.1}$$

Considering the current configuration of a small surface element dA_t with normal **n** subject to Cauchy stress $\boldsymbol{\sigma}$, the surface traction is

$$\mathbf{T} = \boldsymbol{\sigma}\mathbf{n} \tag{2.2}$$

which is separated into normal and tangential parts

$$\begin{aligned} \mathbf{T} &= \mathbf{T}_T + T_N\mathbf{n}, && (2.3)\\ T_N &= (\mathbf{n}^{\mathrm{t}}\boldsymbol{\sigma}\mathbf{n}), && (2.4)\\ \mathbf{T}_T &= \mathbf{T} - T_N\mathbf{n} = (\boldsymbol{I} - \mathbf{n}\otimes\mathbf{n})\boldsymbol{\sigma}\mathbf{n}, && (2.5) \end{aligned}$$

where **n** is the normal vector at the contact point, and $\boldsymbol{I}$ is the unit tensor.

2.1.2 Basic model of friction

The new model of friction presented in this analysis is developed from the "plasticity" model proposed by Michalowski and Mroz [37] based on the analogy between friction phenomena and elastic-plastic phenomena (Table 1.3).

The model for the stick state of friction is similar to the elastic state of elasto-plasticity as any displacement which occurs during sticking is mainly due to the elastic deformation of asperities which are micro-welded. Similarly the model of the slip state of friction is due partly to plastic deformation of asperities (and also debris particles, if present) and mostly due to the breaking of the bonds formed between contacting asperities.

Consider two bodies, one the *main* body and the other the *secondary* body. All friction measurements occur on the surface boundary of the main body, and $\mathbf{n}$ is the outward unit normal on this surface. If the material point $\mathbf{X}_M$ on the main surface is in contact with the material point $\mathbf{X}_S$ of the secondary surface, then the subsequent relative displacement $\mathbf{u}_C$ between the contacting surfaces

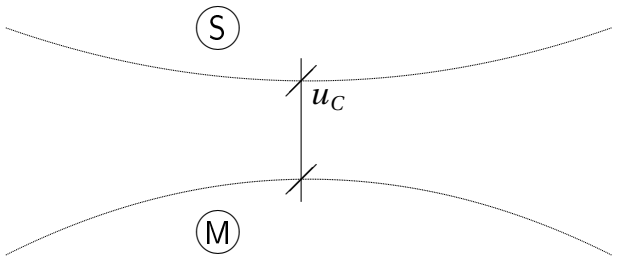

is defined as

$$\mathbf{u}_C = \mathbf{X}_M - \mathbf{X}_S, \tag{2.6}$$

and is separated into the tangential displacement $\mathbf{u}_T$, called *slide*, and the normal displacement u_N:

$$\mathbf{u}_C = \mathbf{u}_T + u_N\mathbf{n}, \quad u_N = \mathbf{u}_C \cdot \mathbf{n}, \quad \mathbf{u}_T = (\boldsymbol{I} - \mathbf{n}\otimes\mathbf{n})\mathbf{u}_C. \tag{2.7}$$

The rate of the *sliding displacement* $\mathbf{u}_T$ is decomposed into *adhesive* and *slipping* states

$$\dot{\mathbf{u}}_T = \dot{\mathbf{u}}_T^{\mathrm{ad}} + \dot{\mathbf{u}}_T^{\mathrm{sl}}. \tag{2.8}$$

The relationship between the frictional traction, $\mathbf{T}_T^{\mathrm{ad}}$, and the displacement in the adhesive state, $\mathbf{u}_T^{\mathrm{ad}}$, is assumed to be linear elastic and is given by

$$\mathbf{T}_T^{\mathrm{ad}} = k\mathbf{u}_T^{\mathrm{ad}}, \tag{2.9}$$

where k is the "stiffness in stick" elastic coefficient for the adhesive state. This is the first parameter of this model, which has two parameters. The second parameter is described below. The k parameter provides a linear transition between the sticking and slipping states and can thus be interpreted as a regularization parameter for this transition. Equation (2.9) defines the admissible displacement during adhesion.

In the slipping state of friction, in analogy to a plastic flow rule, a nonassociated slip rule is defined

$$\dot{\mathbf{u}}_T^{\mathrm{sl}} = -\dot{\gamma}\frac{\partial \phi}{\partial \mathbf{T}_T}, \tag{2.10}$$

where γ is a real function that gives the magnitude of slip and $\phi(\mathbf{T}_T)$ is the slip potential which determines the direction of slip. Further, we define, in analogy to a plastic yield function, the slip function ψ which determines the state of friction:

$$\begin{aligned} \psi \leq 0 \quad &\Rightarrow \quad \text{adhesive state,} \\ \psi > 0 \quad &\Rightarrow \quad \text{slipping state.} \end{aligned} \tag{2.11}$$

The slip potential and slip function for isotropic Amontons-Coulomb friction are given by:

$$\phi(\mathbf{T}_T) = |\mathbf{T}_T|, \tag{2.12}$$

$$\psi(\mathbf{T}_T, T_N) = |\mathbf{T}_T| - \mu T_N, \tag{2.13}$$

where μ is the coefficient of friction, which is the second parameter of this friction model. During slipping the slip condition $\psi = 0$ is enforced, i.e.

$$\mathbf{T}_T^{\mathrm{sl}} = \mu T_N. \tag{2.14}$$

The "loading" condition is $\psi = 0$ and $\gamma > 0$, and the "unloading" condition is $\psi < 0$ and $\gamma = 0$.

"loading" $\longrightarrow$ transition from sticking to slipping state
"unloading" $\longrightarrow$ transition from slipping to sticking state

By keeping μ general it is possible to include more advanced constitutive models alternative to the Amontons-Coulomb (AC) model.

2.1.3 WVS model

Wriggers, vu Van and Stein [76] used physical arguments to model the frictional interaction based on the properties of the bulk material. In particular using the shear yield of the bulk material to determine the force needed to shear asperities and micro-welds.

The frictional slip function becomes

$$\psi(\mathbf{T}_T, T_N) = |\mathbf{T}_T| - \alpha T_N^{\nu} - \beta T_N, \tag{2.15}$$

where ν is a parameter estimating the difference between nominal contact area and actual contact area (at the tips of asperities), and parameters α and β are derived from the shear strength of the bulk material.

Equation 2.15 implies the non-constant coefficient of friction is

$$\mu(T_N) = \beta + \alpha T_N^{\nu-1}. \tag{2.16}$$

2.1.4 Work hardening friction model

The friction model proposed by de Souza-Neto, et al. [63] extends the basic AC model by including the concept of work hardening (WH) from plasticity. The frictional slip function becomes

$$\psi(\mathbf{T}_T, T_N, \omega) = |\mathbf{T}_T| - \mu(\omega) T_N, \tag{2.17}$$

where the coefficient of friction, $\mu(\omega)$, is now a function of the internal state variable ω, which is the density of frictional work,

$$\dot{\omega} = -\mathbf{T}_T \cdot \dot{\mathbf{u}}_T^{\mathrm{sl}}, \qquad \Delta\omega = -\mathbf{T}_T \cdot \Delta\mathbf{u}_T^{\mathrm{sl}}. \tag{2.18}$$

This is also an isotropic model and the slip potential is $\phi(\mathbf{T}_T) = |\mathbf{T}_T|$.

The state variable ω is evaluated at each increment and then the coefficient of friction μ is calculated from the friction function $\mu(\omega)$. This model is successfully used in [63] to describe the change in μ for coated steels, where surface wear can be significant, and also the change in surface roughness during slipping. Choosing a polynomial fit to experimental data, $\mu(\omega)$ has the form

$$\mu(\omega) = \alpha_0 + \alpha_1\omega + \alpha_2\omega^2 + \alpha_3\omega^3 + \alpha_4\omega^4. \tag{2.19}$$

Values for the coefficients α_i, calculated from least-square fits to experimental measurements, are given in [63].

2.1.5 Incremental friction model

The formulations of the co-rotational friction model, Eulerian and Lagrangian, are given here, with the updated Lagrangian formulation utilised in the FEM code ABAQUS [1].

In a numerical procedure, the increments, derived from rate equations of the contact traction and displacement relationships are used. The formulation of the equations should be objective with respect to the imposed rotation of the reference frame during deformation and this objectivity is preserved when the local reference frame at the contact surface (or contact point in a discretised system) is used. The co-rotational rates are expressed with respect to a reference frame moving with the particle along the contacting surface. The rotation of the reference frame, when a particle flows along the surface of a tool, is expressed in terms of the *velocity vector* and the *curvature tensor* of the tool surface. Consider the surface $F(\mathbf{x}) = 0$ for which the normal vector $\mathbf{N} = \partial F / \partial \mathbf{x}$ is a differentiable function.

In the "main-secondary" approach used in contact model, the main surface is the rigid toolpiece and is defined by the function $F(\mathbf{x})$. As we require F to have the appropriate continuity and be differentiable, these rigid surfaces are modelled with bi-cubic piece-wise surfaces. Several approaches are available: Bézier surfaces [22], Hermite patches [21], and NURBS [60].

The model presented here overlaps with the model proposed by Anand [3]. Where the new model differs is in the choice of objective rate as described below.

Differentiating the surface equation twice, the following relations are obtained

$$\dot{F}(\mathbf{x}) = N_k v_k \tag{2.20}$$

$$\ddot{F}(\mathbf{x}) = \left(\frac{\partial N_l}{\partial x_k} v_k + N_k L_{kl} \right) v_l \tag{2.21}$$

where N_k and L_{kl} are the surface gradient (the normal vector) and the velocity gradient, respectively. The second equation implies the relation

$$\dot{N}_l = \frac{\partial N_l}{\partial x_k} v_k = -N_k L_{kl}, \quad \text{or} \quad \dot{\mathbf{N}} = -\boldsymbol{L}^{\mathrm{t}} \mathbf{N} \tag{2.22}$$

Introducing the *unit* normal vector, $\mathbf{n} = \mathbf{N}/|\mathbf{N}|$, its rate is calculated by

$$\dot{\mathbf{n}} = (\boldsymbol{I} - \mathbf{n} \otimes \mathbf{n}) \frac{\dot{\mathbf{N}}}{|\mathbf{N}|} = (\boldsymbol{I} - \mathbf{n} \otimes \mathbf{n}) \boldsymbol{L}^{\mathrm{t}} \mathbf{n}. \tag{2.23}$$

The spin tensor $\boldsymbol{\Omega}$ of the contact reference frame can be expressed as follows

$$\boldsymbol{\Omega} = \dot{\mathbf{n}} \otimes \mathbf{n} = -(\boldsymbol{I} - \mathbf{n} \otimes \mathbf{n}) \boldsymbol{L}^{\mathrm{t}} \mathbf{n} \otimes \mathbf{n} \tag{2.24}$$

and is specified by the "external" portion of the velocity gradient $\boldsymbol{L}^{\mathrm{t}} \mathbf{n}$.

Consider the transformation from the local reference frame to a global system specified by the orthogonal tensor $\boldsymbol{Q}$. Transforming the traction vector $\mathbf{T}$ to the global frame and differentiating, we obtain the traction rate with respect to the local system,

$$\overset{\circ}{\mathbf{T}} = \boldsymbol{Q} \frac{d}{dt} (\boldsymbol{Q}^{\mathrm{t}} \mathbf{T}) = \boldsymbol{Q} (\dot{\boldsymbol{Q}}^{\mathrm{t}} \mathbf{T} + \boldsymbol{Q}^{\mathrm{t}} \dot{\mathbf{T}}) = \dot{\mathbf{T}} - \boldsymbol{\Omega} \mathbf{T} \tag{2.25}$$

where

$$\boldsymbol{\Omega} = \dot{\boldsymbol{Q}}\boldsymbol{Q}^{\mathrm{t}} - \boldsymbol{Q}\dot{\boldsymbol{Q}}^{\mathrm{t}} \tag{2.26}$$

is the spin of the local frame.

Anand uses the co-rotational rate $\overset{\circ}{\mathbf{T}} = \dot{\mathbf{T}} - \boldsymbol{\omega}\mathbf{T}$ where $\boldsymbol{\omega}$ is the twist tensor defined by the rotation of co-ordinate frames $\boldsymbol{R}$ similarly to equation 2.25.

To simplify notation, we use

$$(\cdots)^{\bullet} = \frac{d}{dt}(\cdots) \tag{2.27}$$

to denote the ordinary time derivative.

Another co-rotational rate can be specified by using the *material spin* generated by the deformation of the elastic-plastic body, specified by the velocity gradient,

$$\boldsymbol{W} = \tfrac{1}{2}(\boldsymbol{L} - \boldsymbol{L}^{\mathrm{t}}) \tag{2.28}$$

and the co-rotational rate is given by Jaumann's derivative ([8] §3.7.3), which, for a scalar, a vector and a second-order tensor, is given by:

Type	**Jaumann's derivative**		
scalar	$\overset{\triangledown}{\gamma}$	$=$	$\dot{\gamma}$
vector	$\overset{\triangledown}{\mathbf{T}}$	$=$	$\dot{\mathbf{T}} - \boldsymbol{W}\mathbf{T}$
tensor	$\overset{\triangledown}{\boldsymbol{S}}$	$=$	$\dot{\boldsymbol{S}} - \boldsymbol{W}\boldsymbol{S} + \boldsymbol{S}\boldsymbol{W}$

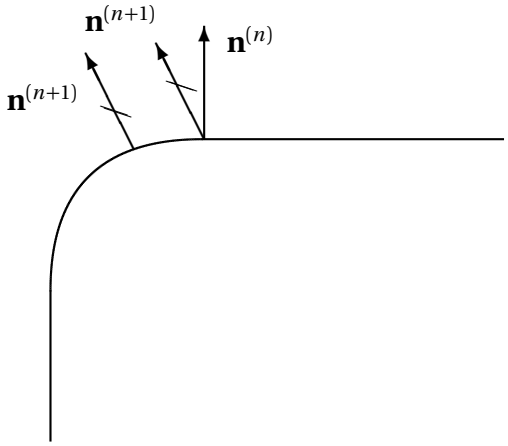

Figure 2.1: Incremental change in *direction* of surface normal at point of contact.

Using the co-rotational rate, the constitutive equation for the shear stress rate can be written as

$$\overset{\nabla}{\mathbf{T}}_T = k(\dot{\mathbf{u}}_T - \dot{\mathbf{u}}_T^{\mathrm{sl}}) = k\dot{\mathbf{u}}_T + k\dot{\gamma}\frac{\mathbf{T}_T}{|\mathbf{T}_T|} \tag{2.29}$$

where $\dot{\gamma}$ is specified from the consistency condition $\Psi(T_N, \mathbf{T}_T) = 0$.

Eulerian frame

In the current configuration the slip function is given by

$$\begin{aligned}
\psi &= |\mathbf{T}_T| - \mu T_N && (2.30)\\
&= [\mathbf{T}_T \cdot \mathbf{T}_T]^{1/2} - \mu T_N && (2.31)\\
&= [(\mathbf{T} - T_N\mathbf{n}) \cdot (\mathbf{T} - T_N\mathbf{n})]^{1/2} - \mu T_N && (2.32)\\
&= [\mathbf{T}\cdot\mathbf{T} - 2\mathbf{T}\cdot T_N\mathbf{n} + T_N^2]^{1/2} - \mu T_N && (2.33)\\
&= [\mathbf{T}\cdot\mathbf{T} - T_N^2]^{1/2} - \mu T_N && (2.34)
\end{aligned}$$

which, after substituting relations (2.4) and (2.5), becomes

$$\psi = [(\boldsymbol{\sigma}\mathbf{n})^{\mathrm{t}}(\boldsymbol{\sigma}\mathbf{n}) - (\mathbf{n}^{\mathrm{t}}\boldsymbol{\sigma}\mathbf{n})^2]^{1/2} - \mu(\mathbf{n}^{\mathrm{t}}\boldsymbol{\sigma}\mathbf{n}), \tag{2.35}$$

and the slip potential becomes

$$\phi = [(\boldsymbol{\sigma}\mathbf{n})^{\mathrm{t}}(\boldsymbol{\sigma}\mathbf{n}) - (\mathbf{n}^{\mathrm{t}}\boldsymbol{\sigma}\mathbf{n})^2]^{1/2}. \tag{2.36}$$

For the given slip potential (2.12), the slip rule (2.10) becomes

$$\dot{\mathbf{u}}_T^{\mathrm{sl}} = -\dot{\gamma}\frac{\mathbf{T}_T}{|\mathbf{T}_T|}. \tag{2.37}$$

The rate-type equations of the friction constitutive model need to be replaced by incremental equations for the numerical solution procedure. This is done by a simple backward difference scheme. In plasticity it is necessary to perform a similar incremental formulation, and we make use of the analogy between stick-slip friction and elasto-plasticity to adapt the algorithms from plasticity for friction. This is necessary because friction is too unlike the continuous nature of elasticity where the discontinuous transition between two unlike states does not occur. Further, the standard use of the backward difference scheme assumes a linear motion along the tangent plane to the contact surface. The method presented below improves this by using a more sophisticated objective rate measure in the incremental scheme.

The value of the rate of slipping $\dot{\mathbf{u}}_T^{\mathrm{sl}}$ at the *current* increment $n+1$ (time $t+\Delta t$) can be written as

$$\dot{\mathbf{u}}_T^{\mathrm{sl}}|^{(n+1)} = \left[-\dot{\gamma}\frac{\partial \phi}{\partial \mathbf{T}_T}\right]^{(n+1)} \tag{2.38}$$

which, in incremental (updated) form, consists of the slip measured at the *previous* step n (time t) plus the increment in the slip that updates the slip to the current step

$$\dot{\mathbf{u}}_T^{\mathrm{sl}}|^{(n+1)} = \left[-\dot{\gamma}\frac{\partial \phi}{\partial \mathbf{T}_T}\right]^{(n)} + \Delta t \left[-\dot{\gamma}\frac{\partial \phi}{\partial \mathbf{T}_T}\right]^{\nabla}\Bigg|^{(n)} \tag{2.39}$$

$$= \left[-\dot{\gamma}\frac{\partial \phi}{\partial \mathbf{T}_T}\right]^{(n)} + \Delta t \left[-\ddot{\gamma}\frac{\partial \phi}{\partial \mathbf{T}_T} - \dot{\gamma}\left(\frac{\partial \phi}{\partial \mathbf{T}_T}\right)^{\nabla}\right]^{(n)} \tag{2.40}$$

$$= \left[-\dot{\gamma}\frac{\mathbf{T}_T}{|\mathbf{T}_T|}\right]^{(n)} + \left[-\Delta\dot{\gamma}\frac{\mathbf{T}_T}{|\mathbf{T}_T|} - \Delta\gamma\left(\frac{\mathbf{T}_T}{|\mathbf{T}_T|}\right)^{\nabla}\right]^{(n)} \tag{2.41}$$

$$= -\dot{\gamma}^{(n)}\frac{\mathbf{T}_T}{|\mathbf{T}_T|}\Bigg|^{(n)} - \Delta\dot{\gamma}^{(n)}\frac{\mathbf{T}_T}{|\mathbf{T}_T|}\Bigg|^{(n)} - \Delta\gamma^{(n)}\left[\left(\frac{\mathbf{T}_T}{|\mathbf{T}_T|}\right)^{\nabla}\right]^{(n)} \tag{2.42}$$

where the objective time increment of the vector function $\varphi = \mathbf{T}_T/|\mathbf{T}_T|$ of tensor arguments $\mathbf{T}$, $\mathbf{T}_T$, T_N and time t, is given by

$$\overset{\nabla}{\varphi} \approx \frac{1}{\Delta t}(\varphi^{(n+1)} - \varphi^{(n)}) \tag{2.43}$$

with $\overset{\nabla}{\varphi}$ representing the objective Jaumann derivative of the function $\varphi(t)$. The superscripts $^{(n)}$ and $^{(n+1)}$ denote the previous and the current time step respectively. The key feature of this incremental form is that we are isolating the rotational terms and can identify the contribution of the normal vector rotation as illustrated in figure 2.1. The usual formulation of the AC model does not refine the rotation of the normal vector for the incremental time-step, where it is assumed that only a linear change takes place, i.e., pure translational motion.

Substituting the full expressions for $\mathbf{T}_T$ and $|\mathbf{T}_T|$ gives for the slipping di-

rection at increment n as:

$$\left.\frac{\mathbf{T}_T}{|\mathbf{T}_T|}\right|^{(n)} = \frac{\mathbf{T}_T^{(n)}}{|\mathbf{T}_T^{(n)}|} = \frac{\boldsymbol{\sigma}^{(n)}\mathbf{n}^{(n)} - ([\mathbf{n}^{(n)}]^{\mathrm{t}}\,\boldsymbol{\sigma}^{(n)}\mathbf{n}^{(n)})\mathbf{n}^{(n)}}{\sqrt{[\mathbf{n}^{(n)}]^{\mathrm{t}}\,\boldsymbol{\sigma}^{(n)}\boldsymbol{\sigma}^{(n)}\mathbf{n}^{(n)} - ([\mathbf{n}^{(n)}]^{\mathrm{t}}\,\boldsymbol{\sigma}^{(n)}\mathbf{n}^{(n)})^2}}. \tag{2.44}$$

Substituting this in the incremental equation (2.42) gives the final result:

$$\begin{aligned}
&\left.\left(\frac{\mathbf{T}_T}{|\mathbf{T}_T|}\right)^{\nabla}\right|^{(n)} \\
&= \frac{\boldsymbol{W}^{(n)}\mathbf{T}_T^{(n)}}{|\mathbf{T}_T^{(n)}|} + \tfrac{1}{2}|\mathbf{T}_T^{(n)}|^{-3}\Big\{2|\mathbf{T}_T|(\dot{\mathbf{n}}^{\mathrm{t}}\boldsymbol{\sigma}\mathbf{n})\mathbf{n} \\
&\quad + (\dot{\mathbf{n}}^{\mathrm{t}}\boldsymbol{\sigma}\boldsymbol{\sigma}\mathbf{n})\mathbf{T}_T - (\mathbf{n}^{\mathrm{t}}\boldsymbol{\sigma}\mathbf{n})(\dot{\mathbf{n}}^{\mathrm{t}}\boldsymbol{\sigma}\mathbf{n})\mathbf{T}_T - 2|\mathbf{T}_T|\dot{\boldsymbol{\sigma}}\mathbf{n} \\
&\quad + (\mathbf{n}^{\mathrm{t}}\dot{\boldsymbol{\sigma}}\boldsymbol{\sigma}\mathbf{n})\mathbf{T}_T - 2(\mathbf{n}^{\mathrm{t}}\boldsymbol{\sigma}\mathbf{n})(\mathbf{n}^{\mathrm{t}}\dot{\boldsymbol{\sigma}}\mathbf{n})\mathbf{T}_T + 2|\mathbf{T}_T|(\mathbf{n}^{\mathrm{t}}\dot{\boldsymbol{\sigma}}\mathbf{n})\mathbf{n} \\
&\quad + 2|\mathbf{T}_T|(\mathbf{n}^{\mathrm{t}}\boldsymbol{\sigma}\dot{\mathbf{n}})\mathbf{n} + (\mathbf{n}^{\mathrm{t}}\boldsymbol{\sigma}\dot{\boldsymbol{\sigma}}\mathbf{n})\mathbf{T}_T + 2|\mathbf{T}_T|(\mathbf{n}^{\mathrm{t}}\boldsymbol{\sigma}\mathbf{n})\dot{\mathbf{n}} \\
&\quad + (\mathbf{n}^{\mathrm{t}}\boldsymbol{\sigma}\mathbf{n})[2(\mathbf{n}^{\mathrm{t}}\boldsymbol{\sigma}\mathbf{n}) - \mathbf{n}^{\mathrm{t}}\boldsymbol{\sigma}\boldsymbol{\sigma}\dot{\mathbf{n}}]\mathbf{n} + (\mathbf{n}\boldsymbol{\sigma}\boldsymbol{\sigma}\dot{\mathbf{n}})\boldsymbol{\sigma}\mathbf{n} \\
&\quad - 2\Big((\mathbf{n}^{\mathrm{t}}\boldsymbol{\sigma}\boldsymbol{\sigma}\mathbf{n})\boldsymbol{\sigma}\dot{\mathbf{n}} + (\mathbf{n}^{\mathrm{t}}\boldsymbol{\sigma}\mathbf{n})[(\mathbf{n}\boldsymbol{\sigma}\dot{\mathbf{n}})\boldsymbol{\sigma}\mathbf{n} - (\mathbf{n}^{\mathrm{t}}\boldsymbol{\sigma}\mathbf{n})\boldsymbol{\sigma}\dot{\mathbf{n}}]\Big)\Big\}^{(n)}.
\end{aligned} \tag{2.45}$$

The time derivative of the unit surface normal $\dot{\mathbf{n}}$ can be expressed in terms of $\mathbf{n}$ as

$$\dot{\mathbf{n}} = (\mathbf{n}^{\mathrm{t}}\boldsymbol{L}\mathbf{n})\mathbf{n} - \boldsymbol{L}^{\mathrm{t}}\mathbf{n} \tag{2.46}$$

where $\boldsymbol{L}$ is the velocity gradient tensor: $\boldsymbol{L} = \nabla\dot{\mathbf{u}}$. Substitution of this into equation (2.45) produces the result:

$$\begin{aligned}
\left.\left(\frac{\mathbf{T}_T}{|\mathbf{T}_T|}\right)^{\nabla}\right|^{(n)} &= \frac{\boldsymbol{W}^{(n)}\mathbf{T}_T^{(n)}}{|\mathbf{T}_T^{(n)}|} + \tfrac{1}{2}|\mathbf{T}_T^{(n)}|^{-3}\Big\{2\dot{\boldsymbol{\sigma}}|\mathbf{T}_T| \\
&\quad + 2|\mathbf{T}_T|(\mathbf{n}\boldsymbol{L}^{\mathrm{t}}\boldsymbol{\sigma}\mathbf{n})\mathbf{n} + (\mathbf{T}\boldsymbol{L}\boldsymbol{\sigma}\boldsymbol{\sigma}\mathbf{n})\mathbf{T}_T - 2(\mathbf{n}^{\mathrm{t}}\boldsymbol{\sigma}\mathbf{n})(\mathbf{n}^{\mathrm{t}}\boldsymbol{L}\boldsymbol{\sigma}\mathbf{n})\mathbf{T}_T \\
&\quad - 2\mathbf{T}_T(\mathbf{n}^{\mathrm{t}}\dot{\boldsymbol{\sigma}}\mathbf{n})\mathbf{n} - (\mathbf{n}^{\mathrm{t}}\dot{\boldsymbol{\sigma}}\boldsymbol{\sigma}\mathbf{n})\mathbf{T}_T + 2(\mathbf{n}^{\mathrm{t}}\boldsymbol{\sigma}\mathbf{n})(\mathbf{n}^{\mathrm{t}}\dot{\boldsymbol{\sigma}})\mathbf{T}_T
\end{aligned}$$

$$
\begin{aligned}
&-2\mathbf{T}_T(\mathbf{n}^{\mathrm{t}}\boldsymbol{L}\mathbf{n})(\mathbf{n}^{\mathrm{t}}\boldsymbol{\sigma}\mathbf{n})\mathbf{n}-(\mathbf{n}^{\mathrm{t}}\boldsymbol{L}\mathbf{n})(\mathbf{n}^{\mathrm{t}}\boldsymbol{\sigma}\boldsymbol{\sigma}\mathbf{n})\mathbf{T}_T\\
&+2(\mathbf{n}^{\mathrm{t}}\boldsymbol{\sigma}\mathbf{n})^2(\mathbf{n}^{\mathrm{t}}\boldsymbol{L}\mathbf{n})\mathbf{T}_T-(\mathbf{n}^{\mathrm{t}}\dot{\boldsymbol{\sigma}}\boldsymbol{\sigma}\mathbf{n})\mathbf{T}_T+2|\mathbf{T}_T|(\mathbf{n}^{\mathrm{t}}\boldsymbol{\sigma}\boldsymbol{L}^{\mathrm{t}}\mathbf{n})\mathbf{n}\\
&-(\mathbf{n}^{\mathrm{t}}\boldsymbol{\sigma}\mathbf{n})(\mathbf{n}^{\mathrm{t}}\boldsymbol{\sigma}\boldsymbol{L}^{\mathrm{t}}\mathbf{n})\mathbf{T}_T-2(\mathbf{n}^{\mathrm{t}}\boldsymbol{\sigma}\mathbf{n})^2(\mathbf{n}^{\mathrm{t}}\boldsymbol{L}\mathbf{n})\\
&+2|\mathbf{T}_T|(\mathbf{n}^{\mathrm{t}}\boldsymbol{\sigma}\mathbf{n})\boldsymbol{L}^{\mathrm{t}}\mathbf{n}-2|\mathbf{T}_T|(\mathbf{n}^{\mathrm{t}}\boldsymbol{\sigma}\mathbf{n})(\mathbf{n}^{\mathrm{t}}\boldsymbol{L}\mathbf{n})\mathbf{n}\\
&+2|\mathbf{T}_T|(\mathbf{n}^{\mathrm{t}}\boldsymbol{\sigma}\mathbf{n})\boldsymbol{L}^{\mathrm{t}}\mathbf{n}-2|\mathbf{T}_T|(\mathbf{n}^{\mathrm{t}}\boldsymbol{\sigma}\mathbf{n})(\mathbf{n}^{\mathrm{t}}\boldsymbol{L}\mathbf{n})\mathbf{n}\\
&+(\mathbf{n}^{\mathrm{t}}\boldsymbol{\sigma}\mathbf{n})[(\mathbf{n}^{\mathrm{t}}\boldsymbol{\sigma}\boldsymbol{\sigma}\mathbf{n})(\mathbf{n}^{\mathrm{t}}\boldsymbol{L}\mathbf{n})-\mathbf{n}^{\mathrm{t}}\boldsymbol{\sigma}\boldsymbol{\sigma}\boldsymbol{L}^{\mathrm{t}}\mathbf{n}]\mathbf{n}\\
&+(\mathbf{n}^{\mathrm{t}}\boldsymbol{\sigma}\boldsymbol{\sigma}\boldsymbol{L}^{\mathrm{t}}\mathbf{n})\boldsymbol{\sigma}\mathbf{n}-(\mathbf{n}^{\mathrm{t}}\boldsymbol{\sigma}\boldsymbol{\sigma}\mathbf{n})(\mathbf{n}^{\mathrm{t}}\boldsymbol{L}\mathbf{n})\boldsymbol{\sigma}\mathbf{n}\\
&-2|\mathbf{T}_T|[\boldsymbol{\sigma}\boldsymbol{L}^{\mathrm{t}}\mathbf{n}-(\mathbf{n}^{\mathrm{t}}\boldsymbol{L}\mathbf{n})\boldsymbol{\sigma}\mathbf{n}]\Big\}^{(n)}
\end{aligned}
\tag{2.47}
$$

Lagrangian frame

An alternative approach is to use a fixed reference frame and replace the Eulerian constitutive measures and vector by the Lagrangian measures. The Cauchy stress tensor and normal vector in terms of the second Piola-Kirchhoff stress tensor, **S**, and the normal to the contact surface, **N**, are given by

$$
\boldsymbol{\sigma}=J^{-1}\boldsymbol{F}\mathbf{S}\boldsymbol{F}^{\mathrm{t}},\quad\text{and}\quad\mathbf{n}\,dA_t=J\boldsymbol{F}^{-\mathrm{t}}\mathbf{N}\,dA_0\quad\Rightarrow\quad\mathbf{n}=J\boldsymbol{F}^{-\mathrm{t}}\mathbf{N}\Lambda,\tag{2.48}
$$

where $\boldsymbol{F}$ is the gradient tensor, $J=\det(\boldsymbol{F})$ is the Jacobian of $\boldsymbol{F}$, dA_0 is the contact surface in the initial configuration reference frame, and $\Lambda=dA_0/dA_t$. Further, since **n** is a unit vector, we have

$$
|\mathbf{n}|=1=J|\boldsymbol{F}^{-\mathrm{t}}\mathbf{N}|\Lambda\quad\Rightarrow\quad\Lambda=1/J|\boldsymbol{F}^{-\mathrm{t}}\mathbf{N}|.\tag{2.49}
$$

Then, using the above transformations, the tractions are expressed by

$$
\begin{aligned}
\mathbf{T}&=\boldsymbol{\sigma}\mathbf{n}=J^{-1}\boldsymbol{F}\mathbf{S}\boldsymbol{F}^{\mathrm{t}}\;J\boldsymbol{F}^{-\mathrm{t}}\mathbf{N}\Lambda=\boldsymbol{F}\mathbf{S}\mathbf{N}\Lambda,&(2.50)\\
\mathbf{T}_T&=\mathbf{T}-T_N\mathbf{n}=\boldsymbol{F}\mathbf{S}\mathbf{N}\Lambda-(J\mathbf{N}^{\mathrm{t}}\mathbf{S}\mathbf{N}\Lambda^2)J\boldsymbol{F}^{-\mathrm{t}}\mathbf{N}\Lambda,&(2.51)\\
T_N&=\mathbf{n}^{\mathrm{t}}\boldsymbol{\sigma}\mathbf{n}=J\mathbf{N}^{\mathrm{t}}\boldsymbol{F}^{-1}\Lambda\,J^{-1}\boldsymbol{F}\mathbf{S}\boldsymbol{F}^{\mathrm{t}}\;J\boldsymbol{F}^{-\mathrm{t}}\mathbf{N}\Lambda=J\mathbf{N}^{\mathrm{t}}\mathbf{S}\mathbf{N}\Lambda^2,&(2.52)
\end{aligned}
$$

where the scalar T_N is the *contact pressure*, $\mathbf{T}_T$ is the friction resistance in the contact plane, and

$$\mathbf{T}\cdot\mathbf{T} = \mathbf{T}^{\mathrm{t}}\mathbf{T} = \mathbf{N}^{\mathrm{t}}\mathbf{S}\boldsymbol{F}^{\mathrm{t}}\boldsymbol{F}\boldsymbol{S}\mathbf{N}\Lambda^2. \tag{2.53}$$

Using the above relations (2.50)–(2.51), the slip function and slip potential become

$$\Psi = [\mathbf{N}^{\mathrm{t}}\mathbf{S}\boldsymbol{F}^{\mathrm{t}}\boldsymbol{F}\boldsymbol{S}\mathbf{N}\Lambda^2 - (J\mathbf{N}^{\mathrm{t}}\mathbf{S}\mathbf{N}\Lambda^2)^2]^{1/2} - \mu J\mathbf{N}^{\mathrm{t}}\mathbf{S}\mathbf{N}\Lambda^2, \tag{2.54}$$

$$\Phi = [\mathbf{N}^{\mathrm{t}}\mathbf{S}\boldsymbol{F}^{\mathrm{t}}\boldsymbol{F}\boldsymbol{S}\mathbf{N}\Lambda^2 - (J\mathbf{N}^{\mathrm{t}}\mathbf{S}\mathbf{N}\Lambda^2)^2]^{1/2}. \tag{2.55}$$

Now the rate of slip can be written as

$$\dot{\mathbf{u}}_T^{\mathrm{sl}} = -\dot{\gamma}\frac{\mathbf{T}_T}{|\mathbf{T}_T|} = -\dot{\gamma}\frac{\boldsymbol{F}\mathbf{S}\mathbf{N}\Lambda - (J\mathbf{N}^{\mathrm{t}}\mathbf{S}\mathbf{N}\Lambda^2)J\boldsymbol{F}^{-\mathrm{t}}\mathbf{N}\Lambda}{[\mathbf{N}^{\mathrm{t}}\mathbf{S}\boldsymbol{F}^{\mathrm{t}}\boldsymbol{F}\boldsymbol{S}\mathbf{N}\Lambda^2 - (J\mathbf{N}^{\mathrm{t}}\mathbf{S}\mathbf{N}\Lambda^2)^2]^{1/2}}. \tag{2.56}$$

In the Lagrangian frame the incremental relationship for the rate of slip involves the use of the material derivative, denoted by a raised dot: $()^{\bullet}$. Then the value of the rate of slipping, $\dot{\mathbf{u}}_T^{\mathrm{sl}}$, at the current time $t+\Delta t$, increment $n+1$, can be written as

$$\dot{\mathbf{u}}_T^{\mathrm{sl}}|^{(n+1)} = \left[-\dot{\gamma}\frac{\partial\phi}{\partial\mathbf{T}_T}\right]^{(n+1)} = \left[-\dot{\gamma}\frac{\partial\phi}{\partial\mathbf{T}_T}\right]^{(n)} + \Delta t\left[-\dot{\gamma}\frac{\partial\phi}{\partial\mathbf{T}_T}\right]^{\bullet}\Bigg|^{(n)} \tag{2.57}$$

$$= -\dot{\gamma}^{(n)}\frac{\mathbf{T}_T}{|\mathbf{T}_T|}\Bigg|^{(n)} - \Delta\dot{\gamma}^{(n)}\frac{\mathbf{T}_T}{|\mathbf{T}_T|}\Bigg|^{(n)} - \Delta\gamma^{(n)}\left[\left(\frac{\mathbf{T}_T}{|\mathbf{T}_T|}\right)^{\bullet}\right]^{(n)}. \tag{2.58}$$

The last term in (2.58) above is given by

$$\left[\left(\frac{\mathbf{T}_T}{|\mathbf{T}_T|}\right)^{\bullet}\right]^{(n)} = \tfrac{1}{2}|\mathbf{T}_T^{(n)}|^{-3}\{\boldsymbol{C}_1\}^{(n)}, \tag{2.59}$$

where $\boldsymbol{C}_1$ is

$$\begin{aligned}
\boldsymbol{C}_1 \;=\; & \Lambda|\Lambda|(2\Lambda^2 J^2(\boldsymbol{N}^{\mathrm{t}}\boldsymbol{S}\boldsymbol{N})(\dot{\boldsymbol{F}}^{\mathrm{t}}/\boldsymbol{F}^{\mathrm{t}2}\boldsymbol{N})(\boldsymbol{N}^{\mathrm{t}}\boldsymbol{S}\boldsymbol{F}^{\mathrm{t}}\boldsymbol{F}\boldsymbol{S}\boldsymbol{N}-\Lambda^2 J^2(\boldsymbol{N}^{\mathrm{t}}\boldsymbol{S}\boldsymbol{N})^2) \\
& +\Lambda J(\boldsymbol{F}^{-\mathrm{t}}\boldsymbol{N})(\Lambda J(\boldsymbol{N}^{\mathrm{t}}\boldsymbol{S}\boldsymbol{N})(\boldsymbol{N}^{\mathrm{t}}\dot{\boldsymbol{S}}\boldsymbol{F}^{\mathrm{t}}\boldsymbol{F}\boldsymbol{S}\boldsymbol{N})-2\Lambda J(\boldsymbol{N}^{\mathrm{t}}\boldsymbol{S}\boldsymbol{F}^{\mathrm{t}}\boldsymbol{F}\boldsymbol{S}\boldsymbol{N})(\boldsymbol{N}^{\mathrm{t}}\dot{\boldsymbol{S}}\boldsymbol{N}) \\
& +(\boldsymbol{N}^{\mathrm{t}}\boldsymbol{S}\boldsymbol{N})(\Lambda J(\boldsymbol{N}^{\mathrm{t}}\boldsymbol{S}\dot{\boldsymbol{F}}^{\mathrm{t}}\boldsymbol{F}\boldsymbol{S}\boldsymbol{N})+\Lambda J(\boldsymbol{N}^{\mathrm{t}}\boldsymbol{S}\boldsymbol{F}^{\mathrm{t}}\dot{\boldsymbol{F}}\boldsymbol{S}\boldsymbol{N})+\Lambda J(\boldsymbol{N}^{\mathrm{t}}\boldsymbol{S}\boldsymbol{F}^{\mathrm{t}}\boldsymbol{F}\dot{\boldsymbol{S}}\boldsymbol{N}) \\
& -2(\dot{\Lambda}J+\dot{J}\Lambda)(2(\boldsymbol{N}^{\mathrm{t}}\boldsymbol{S}\boldsymbol{F}^{\mathrm{t}}\boldsymbol{F}\boldsymbol{S}\boldsymbol{N})-\Lambda^2 J^2(\boldsymbol{N}^{\mathrm{t}}\boldsymbol{S}\boldsymbol{N})^2))) \\
& -(\boldsymbol{F}\boldsymbol{S}\boldsymbol{N}))(\boldsymbol{N}^{\mathrm{t}}\dot{\boldsymbol{S}}\boldsymbol{F}^{\mathrm{t}}\boldsymbol{F}\boldsymbol{S}\boldsymbol{N}) \\
& +2\Lambda^2 J^2(\boldsymbol{F}\boldsymbol{S}\boldsymbol{N})(\boldsymbol{N}^{\mathrm{t}}\boldsymbol{S}\boldsymbol{N})(\boldsymbol{N}^{\mathrm{t}}\dot{\boldsymbol{S}}\boldsymbol{N})-(\boldsymbol{F}\boldsymbol{S}\boldsymbol{N})(\boldsymbol{N}^{\mathrm{t}}\boldsymbol{S}\dot{\boldsymbol{F}}^{\mathrm{t}}\boldsymbol{F}\boldsymbol{S}\boldsymbol{N}) \\
& -(\boldsymbol{F}\boldsymbol{S}\boldsymbol{N})(\boldsymbol{N}^{\mathrm{t}}\boldsymbol{S}\boldsymbol{F}^{\mathrm{t}}\dot{\boldsymbol{F}}\boldsymbol{S}\boldsymbol{N})-(\boldsymbol{F}\boldsymbol{S}\boldsymbol{N})(\boldsymbol{N}^{\mathrm{t}}\boldsymbol{S}\boldsymbol{F}^{\mathrm{t}}\boldsymbol{F}\dot{\boldsymbol{S}}\boldsymbol{N}) \\
& +2((\boldsymbol{N}^{\mathrm{t}}\boldsymbol{S}\boldsymbol{F}^{\mathrm{t}}\boldsymbol{F}\boldsymbol{S}\boldsymbol{N})(\dot{\boldsymbol{F}}\boldsymbol{S}\boldsymbol{N}+\boldsymbol{F}\dot{\boldsymbol{S}}\boldsymbol{N})-\Lambda J(\boldsymbol{N}^{\mathrm{t}}\boldsymbol{S}\boldsymbol{N})^2(\Lambda J(\dot{\boldsymbol{F}}\boldsymbol{S}\boldsymbol{N}) \\
& +\Lambda J(\boldsymbol{F}\dot{\boldsymbol{S}}\boldsymbol{N})-(\dot{\Lambda}J+\dot{J}\Lambda)(\boldsymbol{F}\boldsymbol{S}\boldsymbol{N})))) \\
& /(2\sqrt{(\boldsymbol{N}^{\mathrm{t}}\boldsymbol{S}\boldsymbol{F}^{\mathrm{t}}\boldsymbol{F}\boldsymbol{S}\boldsymbol{N}-\Lambda^2 J^2(\boldsymbol{N}^{\mathrm{t}}\boldsymbol{S}\boldsymbol{N})^2)}) \qquad (2.60)
\end{aligned}$$

The formidable expression for $\boldsymbol{C}_1$ was generated by use of the symbolic computer algebra package DERIVE [48].

Updated Lagrangian frame

In the *updated* Lagrangian formulation the reference configuration is now the configuration at time t, increment n, with the current configuration being time $t+\Delta t$, increment $n+1$. The reference variables are the same as for the Lagrangian formulation and now are denoted by $\mathbf{X}^{(n)}$, $\mathbf{S}^{(n)}$, $\mathbf{N}^{(n)}$, $\boldsymbol{F}^{(n)}$, and $J^{(n)}$. This is illustrated in Fig. 2.2.

The advantage of the *updated* Lagrangian formulation is that, since Δt is small for dynamic-explicit simulations, we have

$$\boldsymbol{F}=\boldsymbol{F}^{\mathrm{t}}=\mathbf{1}, \quad J=1, \quad \Lambda=1 \qquad (2.61)$$

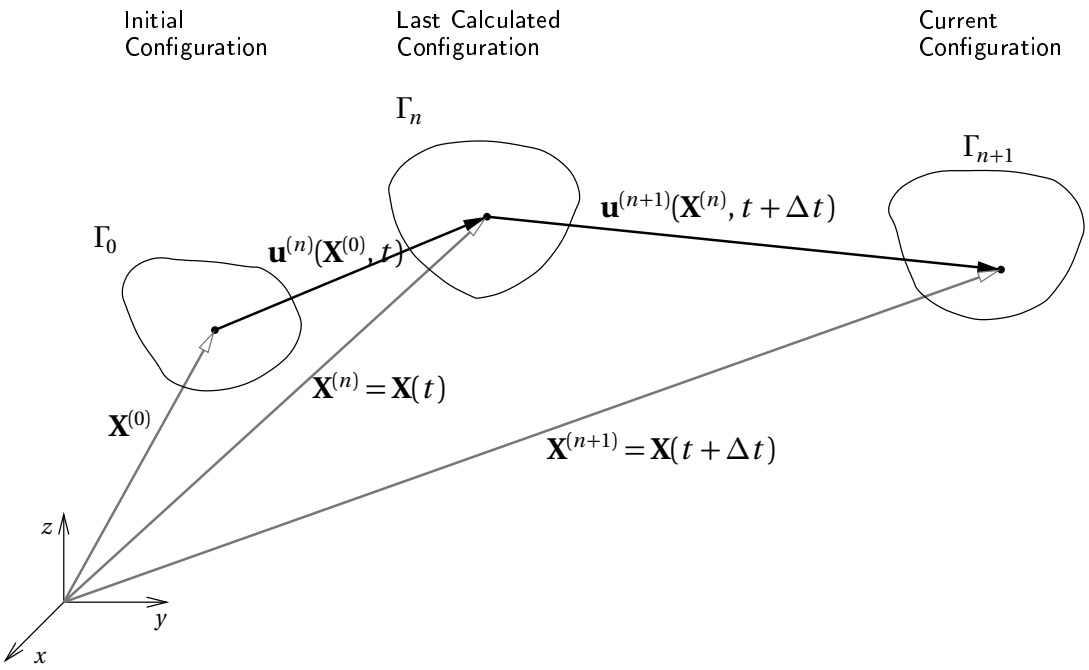

Figure 2.2: The updated Lagrangian formulation uses the variables at time step n as the reference configuration.

which is used to simplify the result.

Substituting for the slip potential (2.55) into the slip rule, and taking the material time derivative for the increment, then making the substitutions in (2.61), the final result is obtained:

$$\dot{\mathbf{u}}_T^{\mathrm{sl}}|^{(n+1)} = \left[-\dot{\gamma}\frac{\mathbf{T}_T}{|\mathbf{T}_T|}\right]^{(n)} + \left[-\Delta\dot{\gamma}\frac{\mathbf{T}_T}{|\mathbf{T}_T|} - \Delta\gamma\left(\frac{\mathbf{T}_T}{|\mathbf{T}_T|}\right)^{\bullet}\right]^{(n)} \tag{2.62}$$

$$= -\dot{\gamma}^{(n)}\frac{\mathbf{T}_T}{|\mathbf{T}_T|}\bigg|^{(n)} + -\Delta\dot{\gamma}^{(n)}\frac{\mathbf{T}_T}{|\mathbf{T}_T|}\bigg|^{(n)} + \mathit{Conv} \tag{2.63}$$

where *Conv* denotes the convectional terms:

$$\mathit{Conv} = -\tfrac{1}{2}|\mathbf{T}_T^{(n)}|^{-3}\left\{\boldsymbol{C}_2\right\}^{(n)}\Delta\gamma \tag{2.64}$$

where $\boldsymbol{C}_2$ is

$$\begin{aligned}
\boldsymbol{C}_2 = {} & (2(\boldsymbol{N}^{\mathrm{t}}\boldsymbol{S}\boldsymbol{N})(\dot{\boldsymbol{F}}^{\mathrm{t}}\boldsymbol{N})(\boldsymbol{N}^{\mathrm{t}}\boldsymbol{S}\boldsymbol{S}\boldsymbol{N}-(\boldsymbol{N}^{\mathrm{t}}\boldsymbol{S}\boldsymbol{N})^2) \\
& +(\boldsymbol{N}^{\mathrm{t}}\dot{\boldsymbol{S}}\boldsymbol{S}\boldsymbol{N})(\boldsymbol{N}(\boldsymbol{N}^{\mathrm{t}}\boldsymbol{S}\boldsymbol{N})-\boldsymbol{S}\boldsymbol{N})-2(\boldsymbol{N}^{\mathrm{t}}\dot{\boldsymbol{S}}\boldsymbol{N})(\boldsymbol{N}(\boldsymbol{N}^{\mathrm{t}}\boldsymbol{S}\boldsymbol{S}\boldsymbol{N}) \\
& -(\boldsymbol{S}\boldsymbol{N})(\boldsymbol{N}^{\mathrm{t}}\boldsymbol{S}\boldsymbol{N})) \\
& +(\boldsymbol{N}^{\mathrm{t}}\boldsymbol{S}\dot{\boldsymbol{F}}^{\mathrm{t}}\boldsymbol{S}\boldsymbol{N})(\boldsymbol{N}(\boldsymbol{N}^{\mathrm{t}}\boldsymbol{S}\boldsymbol{N})-\boldsymbol{S}\boldsymbol{N})+(\boldsymbol{N}^{\mathrm{t}}\boldsymbol{S}\dot{\boldsymbol{F}}\boldsymbol{S}\boldsymbol{N})(\boldsymbol{N}(\boldsymbol{N}^{\mathrm{t}}\boldsymbol{S}\boldsymbol{N}) \\
& -\boldsymbol{S}\boldsymbol{N})+(\boldsymbol{N}^{\mathrm{t}}\boldsymbol{S}\dot{\boldsymbol{S}}\boldsymbol{N})(\boldsymbol{N}(\boldsymbol{N}^{\mathrm{t}}\boldsymbol{S}\boldsymbol{N})-\boldsymbol{S}\boldsymbol{N}) \\
& -2((\boldsymbol{N}^{\mathrm{t}}\boldsymbol{S}\boldsymbol{S}\boldsymbol{N})(2\boldsymbol{N}(\dot{\Lambda}+\dot{j})(\boldsymbol{N}^{\mathrm{t}}\boldsymbol{S}\boldsymbol{N})-\dot{\boldsymbol{F}}\boldsymbol{S}\boldsymbol{N}-\dot{\boldsymbol{S}}\boldsymbol{N}) \\
& -(\boldsymbol{N}^{\mathrm{t}}\boldsymbol{S}\boldsymbol{N})^2(\boldsymbol{N}(\dot{\Lambda}+\dot{j})(\boldsymbol{N}^{\mathrm{t}}\boldsymbol{S}\boldsymbol{N}) \\
& -\dot{\boldsymbol{F}}(\boldsymbol{S}\boldsymbol{N})-\dot{\boldsymbol{S}}\boldsymbol{N}+(\dot{\Lambda}+\dot{j})(\boldsymbol{S}\boldsymbol{N})))) \\
& /(2\sqrt{(\boldsymbol{N}^{\mathrm{t}}\boldsymbol{S}\boldsymbol{S}\boldsymbol{N}-(\boldsymbol{N}^{\mathrm{t}}\boldsymbol{S}\boldsymbol{N})^2)})
\end{aligned} \tag{2.65}$$

The formidable expression for $\boldsymbol{C}_2$ was generated by use of the symbolic computer algebra package DERIVE [48].

2.1.6 Algorithm for friction model implementation

The friction model constitutive equations are integrated using a backward difference method for implementation into the FEM code. Given an increment in the slide, $\Delta\mathbf{u}_T$, the increment in friction traction, $\Delta\mathbf{T}_T^{\text{ad}}$, is

$$\Delta\mathbf{T}_T^{\text{ad}} = k\Delta\mathbf{u}_T. \tag{2.66}$$

The increment in slipping, $\Delta\mathbf{u}_T^{\text{sl}}$, is given by integrating the slip rule over Δt

$$\Delta\mathbf{u}_T^{\text{sl}}|^{(n+1)} = \left[-\Delta\gamma\frac{\mathbf{T}_T}{|\mathbf{T}_T|}\right]^{(n)} + \left[-\Delta^2\gamma\frac{\mathbf{T}_T}{|\mathbf{T}_T|} - \Delta\gamma\Delta t\left(\frac{\mathbf{T}_T}{|\mathbf{T}_T|}\right)^{\bullet}\right]^{(n)}. \tag{2.67}$$

The second order difference $\Delta^2\gamma$ is small and that term can be neglected, then $\Delta\gamma$ is found by enforcing the slipping condition $\Psi = 0$. This results in the predictor-corrector type algorithm shown in Fig. 2.3. The algorithm updates the frictional variables given at the start of the time increment n to the variables at the end of the increment $n+1$. The derivative information $\partial\mathbf{T}_T/\partial\mathbf{u}_T$ and $\partial\mathbf{T}_T/\partial T_N$ is also provided as this is needed for the Jacobian matrix used by the Newton-Raphson method which is used in the FEM program to solve the resulting nonlinear FEM equations. The slipping displacement, $\mathbf{u}_T^{\text{sl}}$, contributes to the sliding displacement, $\mathbf{u}_T$.

2.2 Identification of Friction Parameters

In this chapter non-linear constitutive models for friction have been presented. All are advancements of the classic Amontons-Coulomb model with its single parameter. The WVS model has three parameters: α, β and ν. The WH model

(i) Input: the current increment displacement and pressure
$\Delta\mathbf{u}^{(n+1)}$, ${T_N}^{(n+1)}$

(ii) Elastic predictor: $\mathbf{T}_T^{\mathrm{el}(n+1)} = \mathbf{T}_T^{(n)} - k\Delta\mathbf{u}_T^{(n+1)}$
Slip function: $\Psi = |\mathbf{T}_T^{\mathrm{el}(n+1)}| - \mu T_N^{(n+1)}$

(iii) If $\Psi \leq 0$ then: adhesion
set ${\mathbf{T}_T}^{(n+1)} = \mathbf{T}_T^{\mathrm{el}(n+1)}$
set $\partial\mathbf{T}_T/\partial{\mathbf{u}_T}^{(n+1)} = k\boldsymbol{I}$
set $\partial\mathbf{T}_T/\partial{T_N}^{(n+1)} = \mathbf{0}$

(iv) Else: slipping
set ${\mathbf{T}_T}^{(n+1)} = \mu T_N^{(n+1)}\,\mathbf{T}_T^{\mathrm{el}(n+1)}/|\mathbf{T}_T^{\mathrm{el}(n+1)}|$
solve for $\Delta\gamma$: $|\mathbf{T}_T^{\mathrm{el}(n+1)}| - k\Delta\gamma - \mu {T_N}^{(n+1)} = 0$
set $\Delta\mathbf{u}_T^{\mathrm{sl}(n+1)} = -\Delta\gamma\,\mathbf{T}_T^{\mathrm{el}(n+1)}/|\mathbf{T}_T^{\mathrm{el}(n+1)}|$ + convectional term in (2.64)
set $\partial\mathbf{T}_T/\partial{\mathbf{u}_T}^{(n+1)} = \mathbf{0}$
set $\partial\mathbf{T}_T/\partial{T_N}^{(n+1)} = \mu\,\mathbf{T}_T^{\mathrm{el}(n+1)}/|\mathbf{T}_T^{\mathrm{el}(n+1)}|$

Figure 2.3: Algorithm for the friction model.

does not proscribe a specific functional form for $\mu(\omega)$ but polynomials are the easiest to fit to experimental data. In practice a linear $\mu(\omega) = \alpha_0 + \alpha_1\omega$ or a moderate order ($n \leq 5$) fit have been made [63].

Determination of these parameters from direct experimental data is not easy. The WVS parameters can be calculated from properties of the bulk material (shear strength, et al.) but the trickiest is ν the parameter arising from the difference between nominal and real contact areas.

For the WH model careful and painstaking experimental measurements can be performed, but care must be taken to measure ω, the amount of frictional work done, accurately.

Even for the AC model, values of μ represent an average over a wide range of experiments so that figures quoted for friction between mild sheet-metal and harder tool steel vary from 0.14 to 0.16 [4].

Given the paucity of specific measurement data for even AC friction, the expense of the time consuming WH measurements, and the financial and temporal constraints faced by users of simulations (simulation is mainly chosen as an alternative to expensive and slow experiment) it is necessary to look for an alternative approach to finding reliable values for friction parameters.

Fortunately there exist good data sets for metal forming benchmarks, exemplified by the NUMISHEET conference benchmarks.

It thus remains for an approach that will allow friction parameters to be deduced from the results of the entire process.

The determination of model parameter values from global final results is a classic *inverse problem*.

2.2.1 Inverse problem approaches

An inverse problem is defined simply as the determination of model parameters from results data [62]. There is a set of model parameters α_i, a set of observable data d_i, and the relation $d_i = d_i(\alpha_1, \ldots, \alpha_N)$ which solves the forward problem. This relation is the chosen mathematical model, and its numerical computation is called the 'simulation'.

The basic elements of the inverse problem are:

1. initial estimates of the model parameters;
2. experimental information on the observable data, and the results of numerical simulation;
3. the mathematical model underlying the simulation.

A typical deep-drawing simulation will involve several model parameters including the material model, the process parameters, and the friction model.

The experimental data will include error arising form the variation in results from several experiments and measurements. A probabilistic model can be assigned to describe this, usually an assumption of Gaussian distribution is made and the standard error used.

2.2.2 Objective function choice

The objective function used in the optimisation problem solution is crucial to a stable and accurate result. The tricky area here is that a good fit to several curves is required but experimental data only describes those curves at a small

number of discrete points. It is also desired to accommodate several sets of such curves to ameliorate experimental error.

Classic measures of error, that is difference between the current simulation results and the desired objective include: absolute error

$$\frac{1}{n}\sum_{i=1}^{n}\left|\varepsilon_i-\varepsilon_i^{\text{sim}}\right| \tag{2.68}$$

and relative error

$$\frac{1}{n}\sum_{i=1}^{n}\left|\frac{\varepsilon_i-\varepsilon_i^{\text{sim}}}{\varepsilon_i}\right| \tag{2.69}$$

The latter could be useful in the cases of drawing benchmarks because it eliminates the scale which varies significantly for the different cross section paths along which measurements are taken. However, the range of measured values include zero, and values near zero result in effective large weighting. The absolute error is used to avoid numerical issues.

Given several sets of experimental data the arithmetic mean of the differences is chosen,

$$\Phi=\frac{1}{m}\sum_{k=1}^{m}\left(\frac{1}{n}\sum_{i=1}^{n}\left|\varepsilon_i^k-\varepsilon_i^{\text{sim}}\right|\right) \tag{2.70}$$

for m sets of experimental data compared to the result of the current simulation run $\varepsilon_i^{\text{sim}}$, and n is the number of sample points along the cross-section path of interest.

Chapter 3

FEM Formulation

3.1 Nonstationary contact problem formulation

In this section index notation will be used to improve the clarity of the tensor relations.

3.1.1 Energy balance for Lagrangian description

The second Piola-Kirchhoff stress tensor $\boldsymbol{S} = S_{KL}$ and the Green-Lagrange strain tensor $\boldsymbol{E} = E_{KL}$ are conjugated constitutive variables in the Lagrangian description of motion of an elastic-plastic material. The reaction of an elastic-plastic blank is defined by the following relation

$$(S_{KL}\delta_{LI} + S_{KL}u_{LI})_{,K} + \rho_0 f_I - \rho_0\, t_I = 0 \qquad (\mathbf{X}, \xi) \in {}_t\Omega \times (t_n, t_{n+1}),\, u_I \in C^2 \quad (3.1)$$

with material coordinates $\mathbf{X}$, time t, body forces $\rho_0 t_I$, inertia forces $\rho_0 f_I$. Where the Green-Lagrange strain is defined by

$$E_{KL} = \tfrac{1}{2}(u_{K,L} + u_{L,K} + u_{K,M}\, u_{M,L}). \tag{3.2}$$

which gives the Elastic-plastic constitutive equation

$$\dot{S}_{IJ} = \mathbf{L}^{EP}_{IJKL} \dot{E}_{KL}. \tag{3.3}$$

Boundary conditions can be separated into:

1. Displacement conditions

$$u_I = \varphi_I(\mathbf{X}, \xi) \qquad \text{on } (\mathbf{X}, \xi) \in {}_t\Gamma_U \times (t_n, t_{n+1})$$

2. von Neumann homogeneous conditions

$$u_I = \varphi_I(\mathbf{X}, \xi) = 0 \quad \text{and} \quad \frac{\partial \varphi_I}{\partial N} = 0 \qquad \text{for } (\mathbf{P}, \xi) \in {}_t\Gamma_U \times (t_n, t_{n+1})$$

   for at least one point $\mathbf{P}$, where φ_I is a given displacement function

3. Stress and force conditions

$$(S_{KL}\delta_{LI} + S_{KL}\, u_{L,I}) N_K = F_I \qquad \text{on } {}_t\Gamma_F \times (t_n, t_{n+1})$$

4. Subdifferential contact conditions

$$\begin{array}{lll} \text{if } \Psi \le 0 \text{ then} & \mathbf{T}_T = k\mathbf{u}_T & \text{on } {}_t\Gamma_S \times (t_n, t_{n+1}) \\ \text{if } \Psi > 0 \text{ then} & \mathbf{u}_T = -\dot{\gamma}\left[\frac{\mathbf{T}_T}{|\mathbf{T}_T|} + \Delta t \left(\frac{\mathbf{T}_T}{|\mathbf{T}_T|}\right)^{\nabla}\right] & \\ & \mathbf{T}_T = \mu T_N \frac{\mathbf{T}_T}{|\mathbf{T}_T|} & \text{on } {}_t\Gamma_S \times (t_n, t_{n+1}) \end{array}$$

5. Initial conditions

$$\mathbf{u}(\mathbf{X},0)=0, \qquad \dot{\mathbf{u}}(\mathbf{X},0)=0 \qquad \text{in } {}_t\Omega\times(t_n,t_{n+1})$$

Sets used:

${}_t\Omega$	body at time t
${}_t\Gamma$	$\equiv\partial\,{}_t\Omega$ surface of body at t, ${}_t\Gamma={}_t\Gamma_T\cup{}_t\Gamma_U\cup{}_t\Gamma_S\cup{}_t\Gamma_{\text{fr}}$
${}_t\Gamma_T$	surface under force and stress loads
${}_t\Gamma_U$	surface with prescribed displacements
${}_t\Gamma_S$	contact surface
${}_t\Gamma_{\text{fr}}$	unconstrained surface.

Sets ${}_t\Gamma_T$ and ${}_t\Gamma_U$ can be empty.

Following Ronda [51, 55], the weak formulation of the von Neumann problem for the equation of motion is obtained by taking the scalar product of the differential operator expressed by the L.H.S. of the equation of motion and the difference $(\mathbf{v}-\dot{\mathbf{u}})$, and applying Green's integral theorem. The test function is $\mathbf{v}$ and $\dot{\mathbf{u}}(t)$ is an unknown rate of displacement function. The energy principle, which is the weak differential or the Gateaux differential of a functional appropriate to the weak formulation of von Neumann's problem, is expressed by the following formula:

$$\begin{aligned}
&\int_{{}_t\Omega} S_{KL}(\delta_{LI}+u_{L,I})(v_{I,K}-\dot{u}_{I,K})\,dV-\int_{{}_t\Gamma_T} F_I(v_I-\dot{u}_I)\,d\gamma\\
&-\int_{{}_t\Gamma_U} F_I(v_I-\dot{u}_I)\,d\gamma-\int_{{}_t\Gamma_S}[T_N(v_N-\dot{u}_N)+T_{T_I}(v_{T_I}-\dot{u}_{T_I})]\,d\gamma\\
&\qquad+\int_{{}_t\Omega}\rho_0\,f_I(v_I-\dot{u}_I)\,dV-\int_{{}_t\Omega}\rho_0\,t_I(v_I-\dot{u}_I)\,dV \;=\; 0, \qquad (3.4)
\end{aligned}$$

where $\dot{\mathbf{u}}, \mathbf{v} \in \mathbf{W} \subset H^{1/2}({}_t\Omega)$ and each element of $\mathbf{W}$ is defined on ${}_t\Gamma_U \times (t_n, t_{n+1})$. The integral term $\int_{{}_t\Gamma_U} F_I(v_I - \dot{u}_I)d\gamma$ equals zero as $\dot{u}_I = v_I = \varphi_I$ on ${}_t\Gamma_U \times (t_n, t_{n+1})$. The Sobolev space $H^{1/2}(\Omega)$ is the set of all vector elements in $L_2(\Omega)$ that have generalized derivatives of the first order in the real Hilbert space, $L_2(\Omega)$, which consists of vector functions $\mathbf{u} = (u_1, \ldots, u_K)$ with the norm $\|u\|_{2,\Omega} = (\int_\Omega |u(\mathbf{x})|^2 \, d\mathbf{x})^{1/2}$. The reason space $H^{1/2}(\Omega)$ is used is that in order to accommodate the velocities, $\dot{\mathbf{u}}$, the first derivative of the elements also needs to be L^2-integrable.

The operator expressed by equation (3.4) consists of terms related to stresses, forces and displacements that are inconvenient for seeking stationary points of minimisation in respect of displacement. For this purpose an iteration scheme must be used as only stress variables in the first term can be eliminated by using material constitutive equations. Such replacement requires a rate type formulation of the contact problem. The system of rate type equations can be solved step-by-step using incremental numerical techniques.

Incremental relations valid for finite deformation of an elastic-plastic material are constructed for stress:

$$ {}^{(n+1)}_{0}S_{IJ} = {}^{(n)}_{0}S_{IJ} + {}_0S_{IJ} $$

and strain

$$ {}^{(n+1)}_{0}E_{IJ} = {}^{(n)}_{0}E_{IJ} + {}_0E_{IJ} $$

Where the strain is separated into parts

$$ {}_0E_{IJ} = {}_0e_{IJ} + {}_0\eta_{IJ} $$

with

$$ {}_0\eta_{IJ} = \frac{1}{2}\,{}_0u_{I,K}\,{}_0u_{K,J} $$

and

$$ {}_0e_{IJ} = \tfrac{1}{2}({}_0u_{I,J} + {}_0u_{J,I} + {}^{(n)}_0u_{I,K}\,{}_0u_{K,J} + {}_0u_{I,K}\,{}^{(n)}_0u_{K,J}) $$

The term ${}^{(n)}_0u_{I,K}\,{}_0u_{K,J} + {}_0u_{I,K}\,{}^{(n)}_0u_{K,J}$, is usually neglected in the FEM implementation.

$$ {}_0S_{IJ} = L^E_{IJKL}({}_0E_{KL} - {}_0E^p_{KL}) $$

$$ {}^{(n)}Y({}^{(n)}_0S_{IJ}, {}^{(n)}\kappa) = 0 $$

$$ {}_0E^p_{KL} = \frac{\partial^{(n)}Y}{\partial^{(n)}_0S_{KL}} \frac{{}^{(n)}q_{IJ}L^E_{IJKL}\,{}_0E_{KL}}{{}^{(n)}p_{IJ}\,{}^{(n)}q_{IJ} + {}^{(n)}q_{IJ}L^E_{IJKL}\,{}^{(n)}q_{KL}} $$

$$ {}^{(n)}q_{IJ} = \frac{\partial^{(n)}Y}{\partial^{(n)}S_{IJ}} $$

$$ {}^{(n)}p_{IJ} = \frac{\partial^{(n)}Y}{\partial^{(n)}E^p_{IJ}} $$

$$ {}_0S_{IJ} = {}^{(n)}L^{\mathrm{EP}}_{IJKL}\,{}_0E_{KL} $$

$$ {}^{(n)}L^{\mathrm{EP}}_{IJKL} = L^{\mathrm{E}}_{IJKL} - \frac{L^{\mathrm{E}}_{IJMN}\,{}^{(n)}q_{MN}\,L^E_{KLPQ}\,{}^{(n)}q_{PQ}}{{}^{(n)}p_{MN}\,{}^{(n)}q_{MN} + {}^{(n)}q_{MN}\,L^{\mathrm{E}}_{MNPQ}\,{}^{(n)}q_{PQ}} $$

where ${}^{(n)}_{0}S_{IJ}$ is the second Piola-Kirchhoff stress tensor taken at instant t_n and referred to the initial configuration, ${}_0S_{IJ}$ is the increment of the second Piola-Kirchhoff stress, ${}_0E_{KL}$ is the increment of the Green-Lagrange strain, ${}_0E^p_{KL}$ is the increment of plastic strain, ${}^{(n)}Y$ is the yield surface at time t_n, ${}^{(n)}\kappa$ is the work-hardening parameter, ${}^{(n)}\Lambda$ is a scalar parameter of the elastic-plastic material flow law, L^E_{IJKL} is the constitutive modulus of elasticity, ${}^{(n)}L^{\mathrm{EP}}_{IJKL}$ is the elastic-plastic modulus.

Velocity $\dot{u}_I$ is approximated by a finite difference

$$ {}^{(n+1)}_{0}\dot{u}_I \approx \frac{1}{\Delta t}({}^{(n+1)}_{0}u_I + {}^{(n)}_{0}u_I). \tag{3.5} $$

The first term of equation (3.4) can be split into three parts

$$ \begin{aligned} \int_{{}_t\Omega} {}^{(n+1)}_{0}S_{KL}(\delta_{LI} + {}^{(n+1)}_{0}u_{L,I})\delta^{(n+1)}_{0}u_{K,I}\,dV = \\ \int_{{}_t\Omega} {}^{(n)}L^{EP}_{IJKL}\,{}_0E_{IJ}\,\delta_0E_{KL}\,dV + \int_{{}_t\Omega} {}^{(n)}_{0}S_{KL}\,\delta_0\eta_{KL}\,dV \\ + \int_{{}_t\Omega} {}^{(n)}_{0}S_{KL}\,\delta_0e_{KL}\,dV, \end{aligned} \tag{3.6} $$

where $\delta^{(n+1)}_{0}E_{IJ} = \delta_0E_{IJ}$, and $\delta^{(n+1)}_{0}u_{K,I} = v_{K,I} - u_{K,I}$.

Substituting this in equation (3.4) the following variational principle is obtained:

$$ \begin{aligned} & \int_{{}_t\Omega} {}^{(n)}L^{EP}_{IJKL}\,{}_0E_{IJ}\,\delta_0E_{KL}\,dV + \int_{{}_t\Omega} {}^{(n)}_{0}S_{KL}\,\delta_0\eta_{KL}\,dV + \int_{{}_t\Omega} {}^{(n)}_{0}S_{KL}\,\delta_0e_{KL}\,dV \\ - & \int_{{}_t\Gamma_T} {}^{(n)}_{0}F_I\,\delta_0u_I\,d\gamma - \int_{{}_t\Gamma_U} {}^{(n)}_{0}F_I\,\delta_0u_I\,d\gamma + \int_{{}_t\Omega} \rho_{0\,0}f_I\,\delta_0u_I\,dV \\ - & \int_{{}_t\Gamma_S} ({}^{(n)}_{0}T_N\,\delta_0u_N + {}^{(n)}_{0}T_{T_I}\,\delta_0u_{T_I})d\gamma - \int_{{}_t\Omega} \rho_{0\,0}t_I\,\delta_0u_I\,dV = 0. \end{aligned} \tag{3.7} $$

The Lagrangian formulation of a contact problem is reasonable unless body deformations are small enough to provide uniform transformation from the reference to the current configuration.

Equation (3.7) can be written in the compact form of variational inequality

$$a(\mathbf{u},\mathbf{v}-\mathbf{u})+j(\mathbf{v}_T)-j(\mathbf{u}_T)-\langle f,\mathbf{v}-\mathbf{u}\rangle \geq 0 \tag{3.8}$$

with

$$a(\mathbf{u},\mathbf{v}-\mathbf{u})=\int_{t\Omega} {}^{(n)}L^{EP}_{IJKL}\,{}_0E_{IJ}\,\delta_0 E_{KL}\,dV+\int_{t\Omega} {}^{(n)}_0 S_{KL}\,\delta_0\eta_{KL}\,dV,$$

$$\begin{aligned}\langle f,\mathbf{v}-\mathbf{u}\rangle \;=\; & \int_{t\Omega} {}^{(n)}_0 S_{KL}\,\delta_0 e_{KL}\,dV-\int_{t\Gamma_T} {}^{(n)}_0 F_I\,\delta_0 u_I\,d\gamma-\int_{t\Gamma_S} {}^{(n)}_0 T_N\,\delta_0 u_N\,d\gamma\\ & -\int_{t\Omega}\rho_{0\,0}t_I\,\delta_0 u_I\,dV+\int_{t\Omega}\rho_{0\,0}f_I\,\delta_0 u_I\,dV,\end{aligned}$$

$$j(\mathbf{v}_T)=\int_{t\Gamma_S}\mu|T_N||\mathbf{v}_T|\,d\gamma,\qquad j(\mathbf{u}_T)=\int_{t\Gamma_S}\mu|T_N||\mathbf{u}_T|\,d\gamma.$$

3.1.2 Solution technique

The nonstationary contact problem is solved by applying the FEM to approximate the function defined by the L.H.S. of equation (3.8)

$$\begin{aligned}\alpha(\mathbf{u},\lambda) \;=\; & a(\mathbf{u},\mathbf{v}-\mathbf{u})+\int_{t\Gamma_S}\lambda\mu|T_N||\hat{\gamma}\star\mathbf{v}_T|\,d\gamma\\ & -\int_{t\Gamma_S}\lambda\mu|T_N||\hat{\gamma}\star\mathbf{u}_T|\,d\gamma-\langle f,\mathbf{v}-\mathbf{u}\rangle,\end{aligned} \tag{3.9}$$

and seeking the minimum of $\alpha(\mathbf{u},\lambda)$ using the Lagrange multiplier method, where λ is the Lagrange multiplier. The trace operation $\hat{\gamma}\star\mathbf{w}$ is a mapping defined by

$$\hat{\gamma}:\{\mathbf{w}\in H^{1/2}(\Omega),\mathbf{w}|_{\Gamma_S}=0\}^{\perp}\rightarrow H^{1/2}(\Gamma_S)\subset L^2, \tag{3.10}$$

where $\mathbf{w}$ is $\mathbf{u}$ or $\mathbf{v}$ and $\{\mathbf{w}\in H^{1/2}(\Omega),\mathbf{w}|_{\Gamma_S}=0\}^{\perp}$ is the orthogonal complement of subspace $H^{1/2}$ which contains functions $\mathbf{w}$ that are not vanishing on the boundary Γ_S.

Algorithm for contact problem solution

The algorithm for the solution of the two-body contact problem consists of the following steps:

1. FE approximation of the function $\alpha(\mathbf{u},\lambda)$ given by equation (3.9),
2. minimisation of $\alpha(\mathbf{u},\lambda)$,
3. determination of contact surface Γ_S,
4. calculation of elastic-plastic body material functions,
5. solution of finite element equations.

3.1.3 Finite Element Discretisation

The contact problem is solved numerically by the finite element method. This involves the discretisation of the variational equation, which, for a single ele-

ment e, is given by

$$\Big\{\int_{(n)\Omega^e}[\boldsymbol{B}_L^e]^\top \mathsf{C}^{\mathrm{EP}}[\boldsymbol{B}_L^e]dV^e+\int_{(n)\Omega^e}[\boldsymbol{B}q_{NL}^e]^\top \boldsymbol{S}[\boldsymbol{B}_{NL}^e]dV^e\Big\}\boldsymbol{U}$$
$$+{}^0\rho\Big\{\int_{(n)\Omega^e}[\boldsymbol{H}^e]^\top[\boldsymbol{H}^e]dV^e\Big\}\ddot{\boldsymbol{U}}-\int_{(n)\Omega^e}[\boldsymbol{B}_L^e]^\top[\boldsymbol{S}]\,dV^e-\int_{(n)\Gamma_F^e}[\boldsymbol{H}_S^e]^\top\boldsymbol{F}\,dA^e$$
$$+\int_{(n)\Gamma_S^e}[\boldsymbol{H}_S^e]^\top\boldsymbol{T}_N\,dA^e-\int_{(n)\Gamma_S^e}\lambda[\boldsymbol{H}_S^e]^\top\boldsymbol{T}_T\,dA^e=0 \tag{3.11}$$

$[\boldsymbol{H}^e]$	matrix of volume interpolation functions
$[\boldsymbol{H}_S^e]$	matrix of surface interpolation functions
$[\boldsymbol{B}_L^e]$	linear strain-displacement transformation matrix
$[\boldsymbol{B}_{NL}^e]$	nonlinear strain-displacement transformation matrix
$[\boldsymbol{S}]$	stress tensor $\boldsymbol{S}$ expressed as a vector
C^{EP}	stress-strain elastic-plastic matrix
λ	Lagrange multiplier for the frictional contact constraints

Assembling the complete FE system consists of summing over all the elements [51, 55]:

$$\sum_e\Big\{\int_{(n)\Omega^e}[\boldsymbol{B}_L^e]^\top \mathsf{C}^{\mathrm{EP}}[\boldsymbol{B}_L^e]dV^e+\int_{(n)\Omega^e}[\boldsymbol{B}_{NL}^e]^\top \boldsymbol{S}[\boldsymbol{B}_{NL}^e]dV^e\Big\}\boldsymbol{U}$$
$$+\sum_e{}^0\rho\Big\{\int_{(n)\Omega^e}[\boldsymbol{H}^e]^\top[\boldsymbol{H}^e]dV^e\Big\}\ddot{\boldsymbol{U}}-\sum_e\int_{(n)\Omega^e}[\boldsymbol{B}_L^e]^\top[\boldsymbol{S}]\,dV^e-\sum_e\int_{(n)\Gamma_F^e}[\boldsymbol{H}_S^e]^\top\boldsymbol{F}\,dA^e$$
$$+\sum_e\int_{(n)\Gamma_S^e}[\boldsymbol{H}_S^e]^\top\boldsymbol{T}_N\,dA^e-\sum_e\int_{(n)\Gamma_S^e}\lambda[\boldsymbol{H}_S^e]^\top\boldsymbol{T}_T\,dA^e=0 \tag{3.12}$$

which can simply be rewritten as

$$\boldsymbol{M}\ddot{\boldsymbol{U}} + \boldsymbol{K}\boldsymbol{U} = \boldsymbol{R}, \tag{3.13}$$

where:

$$\begin{aligned}
&\boldsymbol{M} = \textstyle\sum_e {}^0\rho \int_{(n)\Omega^e} [\boldsymbol{H}^e]^\top [\boldsymbol{H}^e] d\,V^e \\
&\boldsymbol{K} = \boldsymbol{K}_L + \boldsymbol{K}_{NL} \\
&\boldsymbol{K}_L = \textstyle\sum_e \int_{(n)\Omega^e} [\boldsymbol{B}_L^e]^\top \mathsf{C}^{\mathrm{EP}} [\boldsymbol{B}_L^e] d\,V^e \qquad \boldsymbol{K}_{NL} = \textstyle\sum_e \int_{(n)\Omega^e} [\boldsymbol{B}_{NL}^e]^\top \boldsymbol{S} [\boldsymbol{B}_{NL}^e] d\,V^e \\
&\boldsymbol{R} = \boldsymbol{R}_I + \boldsymbol{R}_B + \boldsymbol{R}_S \\
&\boldsymbol{R}_I = \textstyle\sum_e \int_{(n)\Omega^e} [\boldsymbol{B}_L^e]^\top [\boldsymbol{S}]\, d\,V^e \qquad \boldsymbol{R}_B = \textstyle\sum_e \int_{(n)\Gamma_F^e} [\boldsymbol{H}_S^e]^\top \boldsymbol{F}\, d\,A^e, \\
&\boldsymbol{R}_S = \textstyle\sum_e \int_{(n)\Gamma_S^e} [\boldsymbol{H}_S^e]^\top \boldsymbol{T}_N\, d\,A^e + \sum_e \int_{(n)\Gamma_S^e} \lambda [\boldsymbol{H}_S^e]^\top \boldsymbol{T}_T\, d\,A^e
\end{aligned}$$

3.2 Friction models

Using concepts defined in the previous chapter: of a slip rule Ψ and a slip criterion Φ the three friction models considered — the standard classical Amontons-Coulomb (AC) model, a model proposed by Wriggers, vu Van and Stein [76] (WVS), and a work-hardening (WH) model proposed by de Souza Neto, et al. [63] — can be shown to be based on the same rules.

The Lagrangian description is used. In addition, as needed, a coordinate system local to the contact point is used as shown in Figure 3.1. Then the friction model rules are the following:

- the decomposition of the surface traction (stress vector) $T_I = S_{IJ} n_J$ into:
  - the normal component $T_{\mathrm{N}} = S_{IJ} n_I n_J$,
  - and the tangential component $T_{\mathrm{T}\,I} = T_I - T_{\mathrm{N}} n_I$,

- the decomposition of the relative displacement at the contact surface u_I into:
  - the normal component $u_{\mathrm{N}} = u_I n_I$,
  - and the tangential component $u_{\mathrm{T}I} = u_I - u_{\mathrm{N}} n_I$,
- the decomposition of the rate of tangential displacement $\dot{u}_\alpha = \dot{u}_\alpha^{\mathrm{ad}} + \dot{u}_\alpha^{\mathrm{sl}}$ that can be also expressed by increments $\Delta u_\alpha = \Delta u_\alpha^{\mathrm{ad}} + \Delta u_\alpha^{\mathrm{sl}}$
  - with the adhesive component defined by a linear relationship (ad)

$$\Delta u_\alpha^{\mathrm{ad}} = -\frac{1}{k_{\mathrm{T}}} \Delta T_\alpha, \tag{3.14}$$

  - and the slipping component (sl) defined by the slip rule

$$\dot{u}_\alpha^{\mathrm{sl}} = -\dot{\gamma} \frac{\partial \Psi}{\partial T_\alpha}, \quad \Delta u_\alpha^{\mathrm{sl}} \approx -\Delta\gamma \frac{\partial \Psi}{\partial T_\alpha}, \tag{3.15}$$

where S_{IJ} is the stress at the contact point, and n_J is the outward normal to the contact surface at the contact point, the tangential displacement in local contact coordinates is denoted by u_α, $\alpha = \mathrm{T}_1, \mathrm{T}_2$, k_{T} is the tangential contact stiffness, γ is an unknown function giving the magnitude of slip.

The slip rule plays a similar role in friction to the flow rule in plasticity. The slip potential Ψ is a function of the stress vector, and the derivatives of which give the direction of slipping. In addition a slip criterion Φ is defined to determine the state of friction:

$$\begin{aligned} \Phi \leq 0 \quad &\Rightarrow \quad \text{adhesive state,} \\ \Phi > 0 \quad &\Rightarrow \quad \text{slipping state.} \end{aligned} \tag{3.16}$$

Further, there exists the following conditions on the slipping/sticking states:

$$\begin{array}{lcl} \text{sticking} & \Rightarrow & \Psi < 0 \quad and \quad \dot{\gamma} = 0, \\ \text{slipping} & \Rightarrow & \Psi = 0 \quad and \quad \dot{\gamma} > 0. \end{array} \tag{3.17}$$

The following particular forms of Ψ and Φ are proposed for the three models considered:

1. the isotropic Coulomb friction

$$\begin{array}{rcl} \Psi(T_\alpha) & = & \sqrt{T_\alpha T_\alpha}, \\ \Phi(T_\alpha, T_{\text{N}}) & = & \sqrt{T_\alpha T_\alpha} - \mu T_{\text{N}}, \end{array} \tag{3.18}$$

   where μ is the coefficient of friction, which may depend on internal parameters such as wear, work-hardening, etc,

2. the WVS model

$$\begin{array}{rcl} \Psi(T_\alpha) & = & \sqrt{T_\alpha T_\alpha}, \\ \Phi(T_\alpha, T_{\text{N}}) & = & \sqrt{T_\alpha T_\alpha} - \alpha T_{\text{N}}^{\nu} + \beta T_{\text{N}}, \end{array} \tag{3.19}$$

   where α, ν and β are the parameters of the model, usually constant, but which may depend on internal parameters such as wear, work-hardening, etc,

3. the work-hardening (WH) model given in de Souza Neto, et al. [63]

$$\begin{array}{rcl} \Psi(T_\alpha) & = & \sqrt{T_\alpha T_\alpha}, \\ \Phi(T_\alpha, T_{\text{N}}, \omega) & = & \sqrt{T_\alpha T_\alpha} - \mu(\omega) T_{\text{N}}, \end{array} \tag{3.20}$$

   where the coefficient of friction $\mu(\omega)$ is now a function of the density of frictional work ω, which is the internal variable of this model,

$$\dot{\omega} = -T_\alpha \dot{u}_\alpha^{\text{sl}}; \qquad \Delta\omega \approx -T_\alpha \Delta u_\alpha^{\text{sl}} \tag{3.21}$$

A predictor-corrector algorithm is used to calculate the frictional stress and slip over a single time step. The algorithm for the AC model is given in figure 3.3. Given the current contact pressure ${T_{\mathrm{N}}}^{(n+1)}$ and contact increment displacement $\Delta {u_\alpha}^{(n+1)}$ at step t_{n+1}, the algorithm provides the frictional stress ${T_\alpha}^{(n+1)}$ and slip $\Delta u_\alpha^{\mathrm{sl}(n+1)}$ at step t_{n+1} using the values at the previous step t_n. Firstly the elastic predictor stress is found, then the slip criterion is calculated to determine the state of friction. The frictional stress is exactly the elastic predictor stress for the adhesive state. The frictional stress is set to the limiting stress μT_{N}, where the direction is along the elastic predictor, for the slipping state. Also the slip contribution is calculated. In a FEM program it is also necessary to provide the derivatives of the frictional stress T_α with respect to the contact pressure T_N and the sliding displacement u_α needed for the Newton-Raphson algorithm. Expressions for $\partial T_\alpha / \partial T_{\mathrm{N}}$ and $\partial T_\alpha / \partial u_\beta$ can be found from consistent linearisation of the frictional constitutive equations

Figure 3.4 gives the algorithm for the WVS model. It consists of identical steps to the AC algorithm except for the change in expressions involving μ.

Figure 3.5 shows the algorithm for the work-hardening friction model. The only difference between this and the AC model is the use of the frictional work internal variable ω. This is changed only when slipping occurs, and must be calculated during the slipping stage of step (iii) of the algorithm.

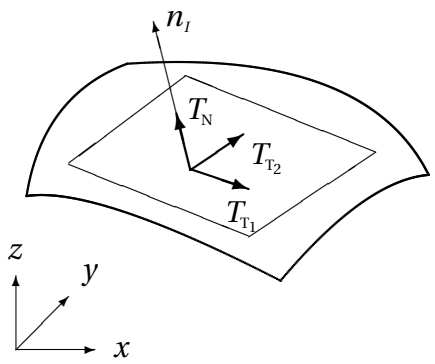

Figure 3.1: The local directions for the friction variables at the contact point.

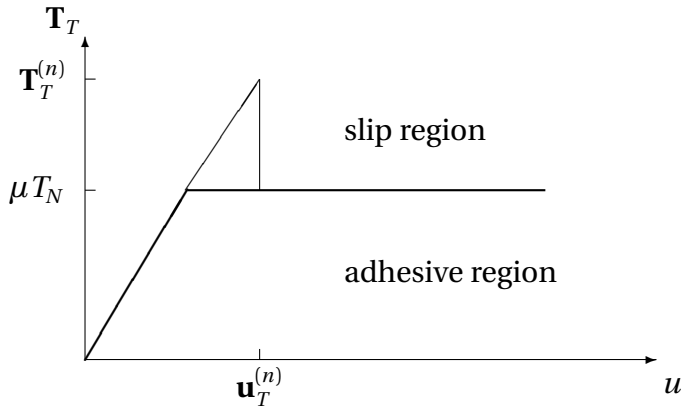

Figure 3.2: The predictor-corrector approach to determining the adhesive or slip region of frictional contact [37] and can be used with a generalised μ.

(i) Input: the current increment displacement and pressure

$\Delta u_\alpha{}^{(n+1)}$, $T_{\mathrm{N}}{}^{(n+1)}$

(ii) Calculate:

Elastic predictor

$$T_\alpha^{\mathrm{el}(n+1)} \leftarrow \left(T_\alpha{}^{(n)} - k_{\mathrm{T}} \Delta u_\alpha{}^{(n+1)}\right)$$

Slip function

$$\Phi \leftarrow \left(\sqrt{T_\beta^{\mathrm{el}(n+1)} T_\beta^{\mathrm{el}(n+1)}} - \mu T_{\mathrm{N}}{}^{(n+1)}\right)$$

(iii) Evaluate contact sub-regions:

If $\Phi \leq 0$ then adhesion region

set $T_\alpha{}^{(n+1)} \leftarrow T_\alpha^{\mathrm{el}(n+1)}$

Else slipping region

set $T_\alpha{}^{(n+1)} \leftarrow \left[\mu T_{\mathrm{N}}{}^{(n+1)} \left(T_\alpha^{\mathrm{el}(n+1)} \Big/ \sqrt{T_\beta^{\mathrm{el}(n+1)} T_\beta^{\mathrm{el}(n+1)}}\right)\right]$

solve for $\Delta\gamma$:

$$\sqrt{T_\beta^{\mathrm{el}(n+1)} T_\beta^{\mathrm{el}(n+1)}} - k_{\mathrm{T}} \Delta\gamma - \mu T_{\mathrm{N}}{}^{(n+1)} = 0$$

set $\Delta u_\alpha^{\mathrm{sl}(n+1)} \leftarrow -\Delta\gamma \left(T_\alpha^{\mathrm{el}(n+1)} \Big/ \sqrt{T_\beta^{\mathrm{el}(n+1)} T_\beta^{\mathrm{el}(n+1)}}\right)$

Figure 3.3: Algorithm for AC friction model over the interval $[t_n, t_{n+1}]$.

(i) Input: the current increment displacement and pressure

$\Delta u_\alpha{}^{(n+1)}$, $T_{\mathrm{N}}{}^{(n+1)}$

(ii) Calculate:

Elastic predictor

$$T_\alpha^{\mathrm{el}(n+1)} \leftarrow \left(T_\alpha{}^{(n)} - k_{\mathrm{T}} \Delta u_\alpha{}^{(n+1)}\right)$$

Slip function

$$\Phi \leftarrow \left(\sqrt{T_\beta^{\mathrm{el}(n+1)} T_\beta^{\mathrm{el}(n+1)}} - \alpha [T_{\mathrm{N}}{}^{(n+1)}]^\nu - \beta\, T_{\mathrm{N}}{}^{(n+1)}\right)$$

(iii) Evaluate contact sub-regions:

If $\Phi \leq 0$ then: adhesion

set $T_\alpha{}^{(n+1)} \leftarrow T_\alpha^{\mathrm{el}(n+1)}$

Else: slipping

$$\text{set } T_\alpha{}^{(n+1)} \leftarrow \left[\left(\alpha \{T_{\mathrm{N}}{}^{(n+1)}\}^\nu + \beta\, T_{\mathrm{N}}{}^{(n+1)}\right)\left(T_\alpha^{\mathrm{el}(n+1)} \Big/ \sqrt{T_\beta^{\mathrm{el}(n+1)} T_\beta^{\mathrm{el}(n+1)}}\right)\right]$$

solve for $\Delta\gamma$:

$$\sqrt{T_\beta^{\mathrm{el}(n+1)} T_\beta^{\mathrm{el}(n+1)}} - k_{\mathrm{T}} \Delta\gamma - \alpha (T_{\mathrm{N}}{}^{(n+1)})^\nu - \beta\, T_{\mathrm{N}}{}^{(n+1)} = 0$$

$$\text{set } \Delta u_\alpha^{\mathrm{sl}(n+1)} \leftarrow -\Delta\gamma \left(T_\alpha^{\mathrm{el}(n+1)} \Big/ \sqrt{T_\beta^{\mathrm{el}(n+1)} T_\beta^{\mathrm{el}(n+1)}}\right)$$

Figure 3.4: Algorithm for WVS friction model over the interval $[t_n, t_{n+1}]$.

(i) Input: the current increment displacement and pressure

$\Delta u_\alpha{}^{(n+1)}$, $T_{\mathrm{N}}{}^{(n+1)}$

(ii) Calculate:

Elastic predictor

$T_\alpha^{\mathrm{el}(n+1)} \leftarrow \left(T_\alpha{}^{(n)} - k_{\mathrm{T}} \Delta u_\alpha{}^{(n+1)}\right)$

Slip function

$\Phi \leftarrow \left(\sqrt{T_\beta^{\mathrm{el}(n+1)} T_\beta^{\mathrm{el}(n+1)}} - \mu(\omega^{(n)}) T_{\mathrm{N}}{}^{(n+1)}\right)$

(iii) Evaluate contact sub-regions:

If $\Phi \leq 0$ then: adhesion

set $T_\alpha{}^{(n+1)} \leftarrow T_\alpha^{\mathrm{el}(n+1)}$

Else: slipping

solve for $\Delta\gamma$ and $\omega^{(n+1)}$:

$0 = \sqrt{T_\beta^{\mathrm{el}(n+1)} T_\beta^{\mathrm{el}(n+1)}} - k_{\mathrm{T}} \Delta\gamma - \mu(\omega^{(n+1)}) T_{\mathrm{N}}{}^{(n+1)}$

$0 = \omega^{(n+1)} - \omega^{(n)} - \mu(\omega^{(n+1)}) T_{\mathrm{N}}{}^{(n+1)} \Delta\gamma$

set $T_\alpha{}^{(n+1)} \leftarrow \mu(\omega^{(n+1)}) T_{\mathrm{N}} \left(T_\alpha^{\mathrm{el}(n+1)} \Big/ \sqrt{T_\beta^{\mathrm{el}(n+1)} T_\beta^{\mathrm{el}(n+1)}}\right)$

set $\Delta u_\alpha^{\mathrm{sl}(n+1)} \leftarrow -\Delta\gamma \left(T_\alpha^{\mathrm{el}(n+1)} \Big/ \sqrt{T_\beta^{\mathrm{el}(n+1)} T_\beta^{\mathrm{el}(n+1)}}\right)$

Figure 3.5: Algorithm for WH friction model over the interval $[t_n, t_{n+1}]$.

3.2.1 Identification of Friction Parameters

The determination of the parameters for a friction model from experimental data is a classic inverse problem:

experimental result $\longrightarrow$ model parameters

The inverse problem can be summarized as:

- unknown model parameters α_i
- known observable data d_i
- there exists a relation $d_i = \Omega(\alpha_1, \ldots, \alpha_N)$ which is the *model*
- the numerical computation of Ω is the *simulation*
- we seek the solution to *inverse problem*

$$\alpha_i = \Omega^{-1}(d_1, \ldots, d_N)$$

Using a numerical optimization method we are able to construct the algorithm illustrated by Figure 3.6 to find an approximate solution to the inverse problem by calculating the difference between experimental and simulation results for some critical values of the model.

1. Choose initial values for friction parameters
2. Call Abaqus/Explicit to solve FEM simulation
3. Calculate objective function

4. Is it minimum?

   YES End, displaying parameters values found

   NO Repeat, using optimization method to choose new parameter values

The simplex method [47] was chosen for its robustness and simplicity.

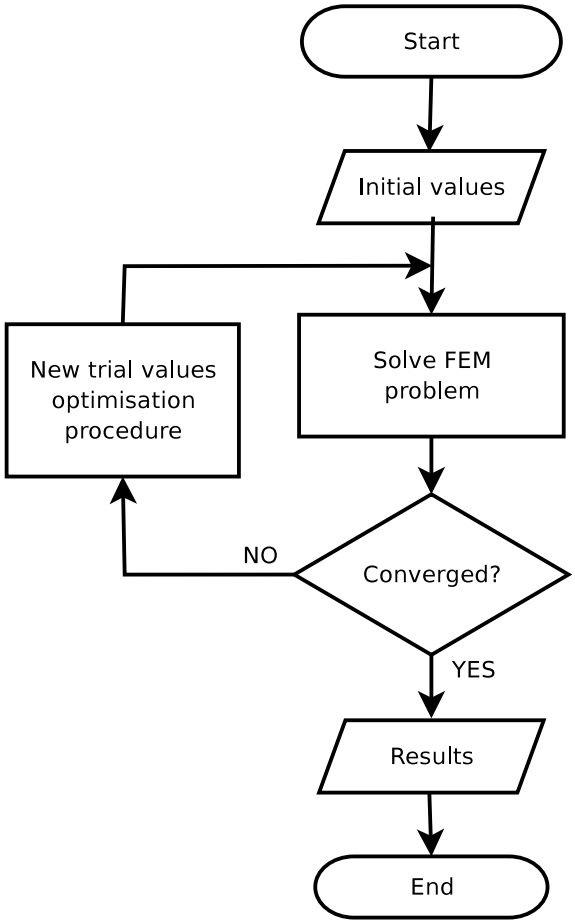

Figure 3.6: Flowchart of parameter identification algorithm

Chapter 4

Results

Different friction models—the classic one proposed by Amontons-Coulomb (AC) with a constant friction coefficient, a three-parameter model proposed by Wriggers et. al. [76], and a model based on the concept of 'work-hardening' proposed by de Souza Neto, *et al.* [63]—in the standard conventional and new corotational formulations are applied to simulate benchmark problems: the 3-D square-cup drawing (NUMISHEET '93) and S-rail stamping (NUMISHEET '96). The results obtained for these three models in both formulations are presented to illustrate the influence of the friction model on the drawing process.

4.1 Introduction

The purpose of this chapter is to compare the two formulations with three different constitutive friction models in the finite element method (FEM) simulation of a complex metal-forming process. The processes chosen are the prismatic square-cup deep-drawing experiment as proposed for the NUMISHEET '93 conference, and the S-rail stamping simulation chosen for the NUMISHEET '96 conference. As a result of these conferences data is available against which to compare the results of the simulations, and also a very detailed standard set of data is available describing the simulations.

Three different friction models are used: the classic Amontons-Coulomb model with a constant coefficient of friction, a nonlinear model proposed by Wriggers, vu Van and Stein [76] which uses three constant parameters (WVS), and a model proposed by de Souza Neto, *et al.* [63] which is based upon work-hardening (WH). This model is appropriate for coated sheet metal, and takes into consideration wear of the surface coating.

The foundation for the friction model is based upon that proposed by Michalowski and Mroz [37] and the work of Curnier [16]. The three models, AC, WVS, WH, are modifications of the basic model where the relationship between frictional limit stress and contact pressure is varied taking into account material behavior and experimental data.

All three friction models presented here are static and do not consider the kinetics of blank motion around punch and die roundings, where normals rotate through almost 90°, which affects particle velocity. The kinetic effects of rotation are considered in a co-rotational formulation [58].

The simulation is implemented in the finite element program Abaqus/Explicit [1] by using large strain shell elements and user friction routines. The

shell elements are general purpose linear 4-node shell elements (type S4R [1] §29.6.2) with finite membrane strains and 5 integration points through the thickness, and reduced integration with hourglass control. The material model used is von Mises isotropic elastic-plastic with hardening, with the given relation between yield stress and plastic strain as was provided by the NUMISHEET experimental data. The symmetry of the square-cup deep-drawing process allows one-quarter of the process to be used in the simulation. The tools: die, stamp, and blankholder, are modelled using rigid Bézier surfaces. The blank is modelled using the shell elements described. All tools dimensions, process parameters and material properties are approved by the automotive industries. The S-rail simulation has no symmetry and the entire tool set has to be used.

The results for major and minor strains, and also contour maps of thickness changes, for the two simulations with various friction models are presented and discussed.

The two NUMISHEET benchmarks [56] [32] were deliberately chosen for their similarity and relationship to real-world industrial stamping and drawing. They were specifically selected because these processes involve large frictional movement over curved tool surfaces which include 90 deg angles, and are large strain problems [58] with large displacements.

There are simpler benchmark simulations which appear often in the literature when modelling friction. The two most common ones are upsetting and indentation benchmarks. However, these simpler benchmarks lack the large rotations, are small strain, and mostly linear displacement, with short linear slipping at the contact surfaces, and these lack the rotational effects of deep-drawing or stamping, with large displacements of the workpiece sliding over curved contact surfaces.

4.2 Deep-drawing simulation

The simulation of the deep-drawing process is conducted for a three-dimensional prismatic square-cup. The FE model of prismatic-cup deep-drawing [57] consists of three tools: punch, die and blankholder, shown in figure 4.1, and a single workpiece: the blank. The dimensions for the tools and material parameters for this simulation are taken from the benchmark chosen for the NUMISHEET '93 conference.

The dimensions for the square-cup deep-drawing tools are:

Tool piece	Dimensions		Rounding radii	
	internal (mm)	external (mm)	corner (mm)	shoulder (mm)
die	66×66	170×170	12	5
blankholder	84×84	170×170	12	3
punch		70×70	10	8

The clearance between the die and the punch is 2 mm, and between the punch and the blankholder is 7 mm. The mesh for the three tools are shown in figure 4.1. The workpiece is 150×150 mm in size with a thickness of 0.78 mm and is made of mild sheet steel with the following material properties:

Young's modulus	206 GPa
Poisson's ratio	0.30
Yield stress	$\sigma = 565.32\,(\varepsilon_p + 0.007117)^{0.2589}$
	ε_p = plastic strain
Coefficient of friction	0.144

The material values are given for assumed isotropic material.

Only one quarter of the blank and tools are modelled for this FE simulation because there exist two axes of symmetry. Two thousand and five hundred shell elements are used to model the quarter of the blank with a uniform mesh of 50×50 shell elements. The tools are modelled using rigid Bézier surfaces.

The square-cup deep-drawing process uses a double-action press: the first step closes the blankholders; the second step moves the punch to its full stroke. This is illustrated in figure 4.6.

The stepping procedure for this FE simulation is as follows:

(1) Place blank on die; place blankholder above die.
(2) Move punch down by 0.01 mm.
(3) Fix punch in place; apply blankholder force.
(4) Move punch down to full stroke.

Step (1) sets up the tools and blank in the correct positions without the blankholder force. In step (2) the punch is moved down slightly at a speed of 0.05 mm/s to establish contact between the punch and blank, and also between the blankholder and blank. In step (3) the blankholder force of 19.6 kN is applied to the blankholder. The punch is then moved down to the full stroke at a speed of 5 mm/s in step (4). Step (2) is necessary to establish contact between the tools and the blank, before the blankholder force can be applied. The blankholder force can only be applied once there is contact between the blankholder and blank.

The AC friction coefficient μ is 0.144 as has been given in the benchmark data.

The values of α and β for WVS model inferred from material data are estimated to be $\alpha = 0.03$ and $\beta = 0.144$, where the second value is chosen so that

for high pressure the WVS model tends to the AC model. The value for ν for the case of metal-metal contact is $\nu = 0.80$.

Experimental measurements of $\mu(\omega)$ for the WH model for aluminium-killed steel sheet are given in de Souza Neto [63], where the linear fit

$$\mu(\omega) = \alpha\,\omega + \beta \tag{4.1}$$

is made. For ω measured in kN/mm, the constants have values and units:

$$\begin{aligned} \alpha &= -8.757 \times 10^{-2}\text{mm/kN} \\ \beta &= 0.1448 \end{aligned}$$

This fit for the function $\mu(\omega)$ actually represents a "work-softening", as the decrease in the value for μ as ω increases reflects the smoothing of the surface of the blank when the asperities are flattened by sliding.

In all the above models, the 'stiffness-in-stick' parameter is $k_T = 100$ GPa, which, while a numerical parameter, should be similar to the elastic coefficient of the metal.

4.3 S-Rail simulation

The S-rail simulation is taken from the NUMISHEET '96 conference benchmark and consists of a similar set of tools as shown in figure 4.2. There is no simple symmetry and the entire set is used in the simulation. Two meshes are used: a medium mesh and a fine mesh shown in figure 4.11 at the full

displacement. The medium mesh is that provided by the NUMISHEET '96 organisers [32] and the fine mesh was an automatic refinement of up to 2 levels.

The S-rail forming process is modelled with a single-action press: the die moves towards the punch in a single action which closes the blank-holders before the punch engages. This is illustrated in figure 4.7.

The blank has thickness of 1.0 mm and is made of mild sheet steel with the following material properties:

Young's modulus	206 GPa
Poisson's ratio	0.30
Yield stress	$\sigma = 526(\varepsilon_p + 0.015)^{0.239}$
Coefficient of friction	0.11

The AC friction coefficient μ is 0.11 as has been given in the benchmark data.

The values of α and β for WVS model inferred from material data are estimated to be $\alpha = 0.03$ and $\beta = 0.11$, where the second value is chosen so that for high pressure the WVS model tends to the AC model. The value for ν for the case of metal-metal contact is $\nu = 0.80$.

For the WH model, to ensure compatibility with the benchmark data, the constants are chosen, for ω measured in kN/mm, to have values and units:

$$\begin{aligned} \alpha &= -8 \times 10^{-2} \text{mm/kN} \\ \beta &= 0.11 \end{aligned}$$

In all the above models, the 'stiffness-in-stick' parameter, k, was set to 100 GPa.

4.4 Results

Results obtained for the square-cup deep-drawing and S-rail stamping benchmark problems are shown in the form of plots of principal strains vs. distance along both the diagonal and the side of the blank, contour maps of thinning, and tables with extremal values of principal strains and thinning. Figure 4.3 shows the cross-sections used to measure principle strains in the deep-drawing simulation. For the S-rail simulation figure 4.4 shows the cross-sections used.

4.4.1 Deep-drawing

Figures 4.8 and 4.9 illustrates that the AC model has the largest strain values, which is due to this model using a constant value for the coefficient of friction and not taking into account the variation of μ from pressure and wear as in the case of the WVS and WH models, respectively. The WH and AC results are similar because the WH model is a modification of the AC model with work-hardening included. The WVS results are different in shape from the AC and WH models as its non-linear term dominates.

The curves for the new formulation are almost indistinguishable from the curves of the standard formulation. The additional term arising from the new co-rotational model has clearly had a small overall effect on the results. The variation between constitutive models is much more pronounced. The results nevertheless confirm the new formulation has an effect albeit small, and that the constitutive model is the more important. The remainder of the analysis will thus focus on the difference between the constitutive model results.

These features are confirmed in the tables 4.1 and 4.2 which show the max-

ima and minima of the strains. Along the diagonal OD the WVS and WH models have smaller extrema than the AC model as shown in table 4.1 and figure 4.8. The WVS model's maximum is 47% smaller than the AC model, which indicates that the nonlinear term, $\alpha p_{\mathrm{N}}^{\nu}$, of the WVS model contributes significantly. The lower values of the extrema of the WH model indicate that slipping work has smoothed the surface and reduced the friction stresses.

Along the side OX it is found that the major strain maxima for the WVS and WH models differ by a small amount as shown in table 4.2 and figure 4.9. However, for the WVS model the minor strain extrema near the punch edge (approximately 27 mm from centre) is a minima compared to the maxima for the AC and WH models. This can be attributed to the nonlinear term dominating under the high pressure region where the blank bends over the punch.

These observations are confirmed by the Mises stress contours in figure 4.10. They show the overall higher values for the AC model, and the similar distribution for the WH model. The lower WVS values are also shown with the key area of peak values at the corner appearing smaller in size, showing lower distribution of stress.

4.4.2 S-Rail

The medium mesh reveals qualitatively similar results for the principle strains across cross-section IE in figure 4.12. The peaks are mostly at the same position with differences occurring in value. The relatively coarse mesh shown in figure 4.11 reveals the likely reason: the larger elements tend to smooth out the results and offer lower resolution. The differences in the finer mesh results of figure 4.13 are more dramatic. The greatest distinction in the the thinning curves where larger peaks for the WVS model are a result of its higher friction

forces for lower pressure regimes. This is clearly seen in the contour maps of thinning in figure 4.15 were the WVS model has the largest area of thinning above 5% in the wall of the s-rail.

Table 4.3 shows that the thinning peaks of WVS for both meshes to be some 11% 12% higher than AC. WH is close to AC with the more accurate result for the fine mesh showing it lower. Here the reduction in μ over larger slipping areas for the WH model has made a significant contribution to the result.

Globally, the energies for the simulation are clearly affected by the different models. Table 4.4 shows the proportion of the total deformation energy accounted for by frictional work. The total deformation energy consists of the internal plastic work and the contact sliding work. Table 4.4 shows that frictional dissipation varies from 20% to 28% of the total deformation. As expected the WVS model has highest values since the frictional forces are higher for lower pressure areas. The WH model shows lower values than AC as the lower μ value requires less frictional work.

4.5 Comments

Three friction models of different characteristics in two formulations were used in the deep-drawing and S-rail simulations. The AC model has a single constant coefficient of friction, the WVS model has three parameters with a nonlinear pressure-dependent term, and the WH model accounts for wear proportional to the frictional work. The standard formulation using a convectional description and a new formulation using a corotational were used.

The primary, and somewhat disappointing, discovery is that the difference in results between the two formulations is small. The additional of the rota-

tional terms has a mostly minor effect on the results. There is more noticeable and significant difference in results between different frictional *constitutive* models than the different kinematic models.

Using different friction models in the deep-drawing simulation it was found that the results for major strain along the diagonal differed by 25% to 47%, and the minor strain from 14% to 16%, compared to the AC model. Along the side the major strain differed by 21% to 30%, and the minor strain at the punch edge differed by 150% to 200%, compared to the AC model. These values have sufficient variation to indicate that more accurate models of friction are needed for this simulation.

WH generally gives similar results to AC, which is related to the history of deformation of the blank. This is because the value of μ for the AC model represents an 'average' of the function $\mu(\omega)$ for the WH model. The WVS model uses only the current state of pressure and does not consider the history of the surface deformation.

In the S-rail simulation results were presented for two mesh sizes. The less fine mesh showed little difference between the friction models, however, the finer mesh results showed differences almost a large as for deep-drawing. This indicates that large element sizes tend to reduce the contribution of friction and hence are less accurate.

The energy results show that the three friction models contribute significantly to the final result. Friction is thus an important part of the simulation and the need for more accurate friction models is crucial in the S-rail simulation.

The computational performance of the two simulations for different friction models is summarised in Figure 4.16 for the square-cup and Figure 4.17

for the S-rail simulations. This computational cost is examined for two measures: the total simulation time and the number of iterations taken. The total time is, of course, the more pertinent real-world measure as this impacts an engineer's workflow. The number of iterations, however, reveals the internal cost of convergence.

It can be seen for both simulations that the total time for the simulations using non-standard models is higher than for the default Abaqus model (label AC in the figures). This is an unfortunate characteristic of the software that user subroutines increase computational time. Comparing the AC model with the the same friction model but using the new formulation (label AC′) we see a small increase in number of iterations but a larger increase in time. The nonlinear models (WVS and WH) show greater increases in time which is mostly owing to the greater number of iterations needed. The increased computational cost needs to be balanced with the improved accuracy from advanced models.

For the two typical metal forming simulations it has been shown that friction plays a crucial role and that the different constitutive friction models influence the result as much as 25%. The accuracy of metal forming simulations thus depends as much on a more accurate, more realistic, friction model as on a sufficiently fine mesh. Further, this indicates that the various state variables used by the friction models—contact pressure, internal energy or effective contact area—matter in differing degrees. Simulations using advanced friction models should be selected by which state variables are considered more important for the type of materials used. See, for example, the recent work in [24] and [25] where a new model using additional state variables from the properties, distribution and shape of asperities is formulated.

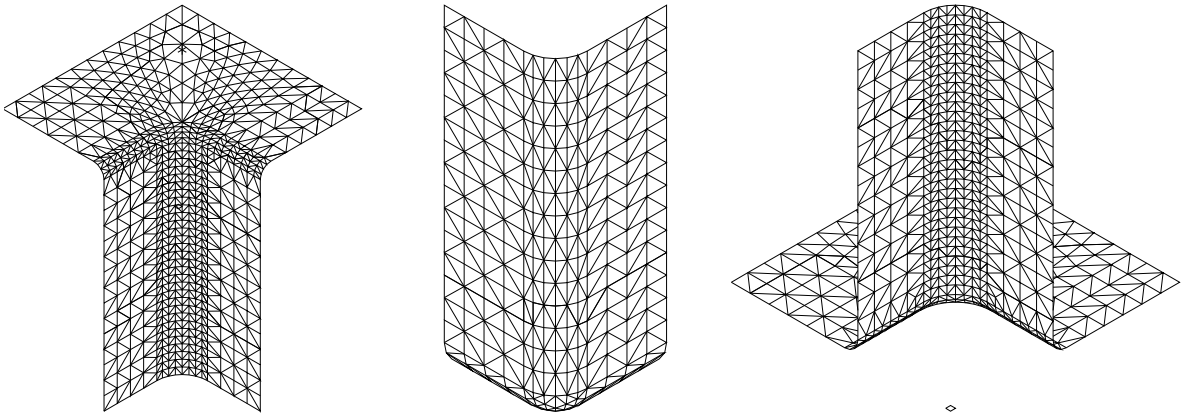

Figure 4.1: The die, punch, and blankholder used in the deep-drawing simulation (only one-quarter shown).

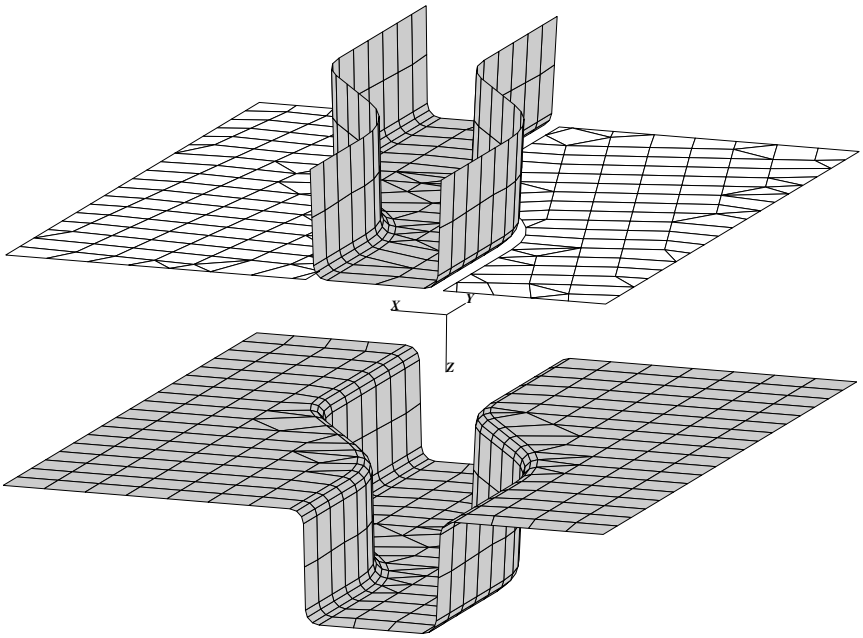

Figure 4.2: The die, punch, and blankholder used in the S-rail simulation.

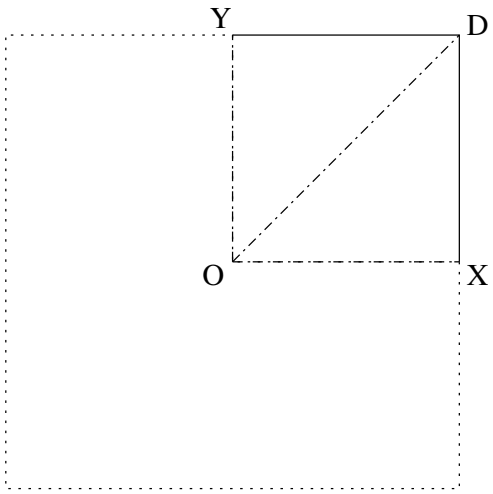

Figure 4.3: Schematic of the deep-drawing simulation showing the cross-sections OX and OD used for measuring principle strains. As shown, only one-quarter of the blank is modelled with suitable boundary conditions applied along OY and OX to accommodate the symmetry.

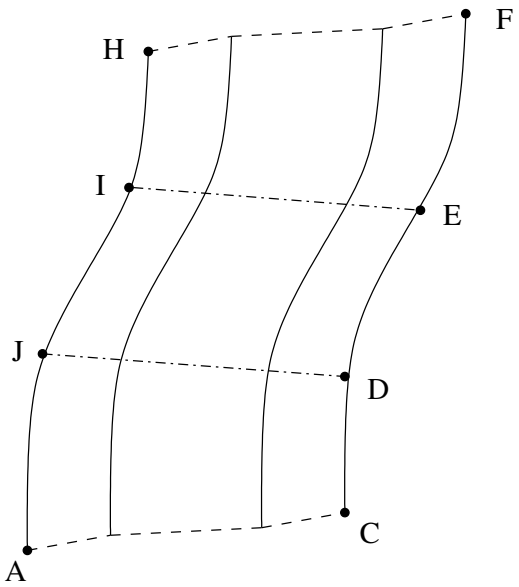

Figure 4.4: Schematic of the S-rail simulation showing the cross-sections EI and DJ used for measuring principle strains.

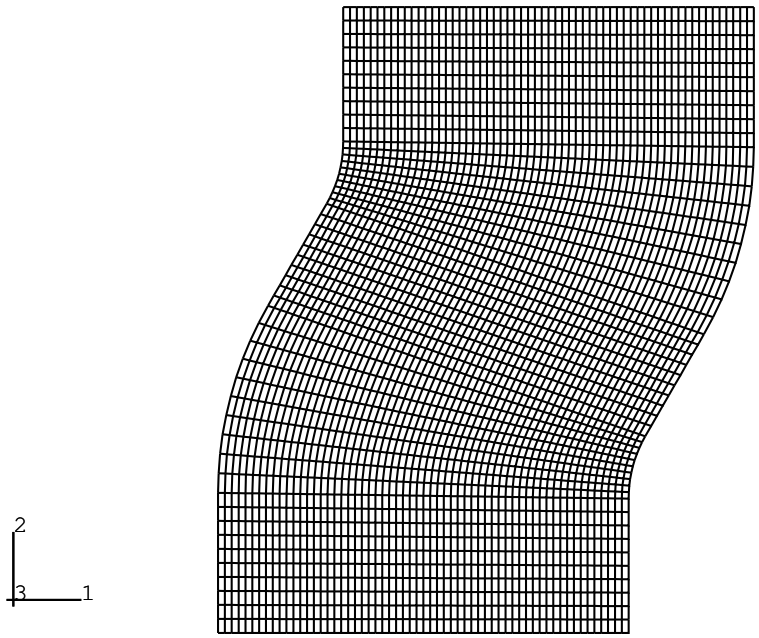

Figure 4.5: Initial mesh for the S-rail simulation workpiece blank.

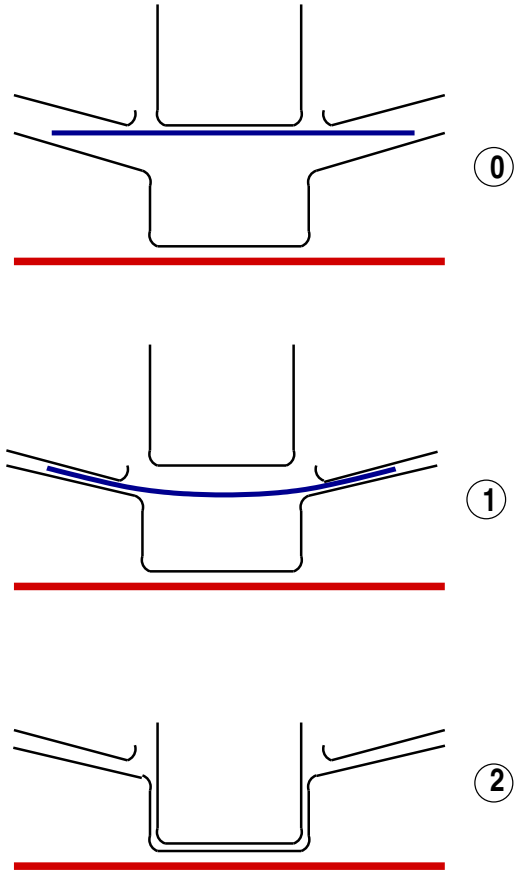

Figure 4.6: Steps of the double-action press used for the square-cup deep-drawing process.

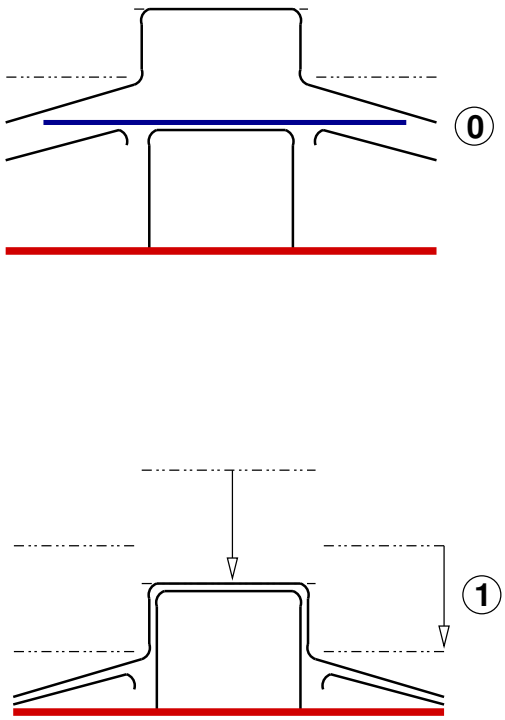

Figure 4.7: Steps of the single-action press used for the S-rail stamping process.

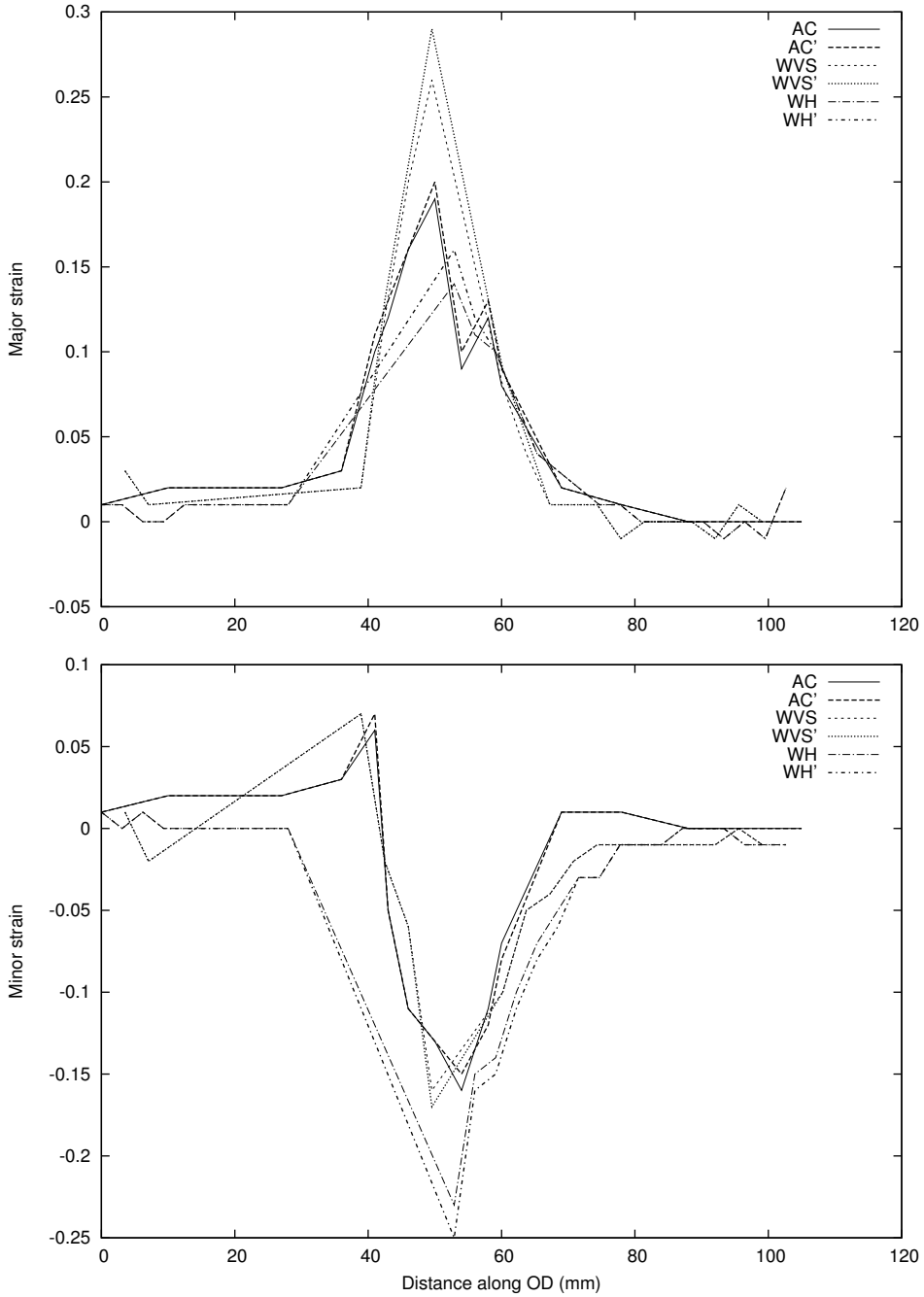

Figure 4.8: Graphs showing the principal strains for the diagonal of the deep-drawing blank. The curves labelled AC′, WVS′ and WH′ refer to the new co-rotational formulation.

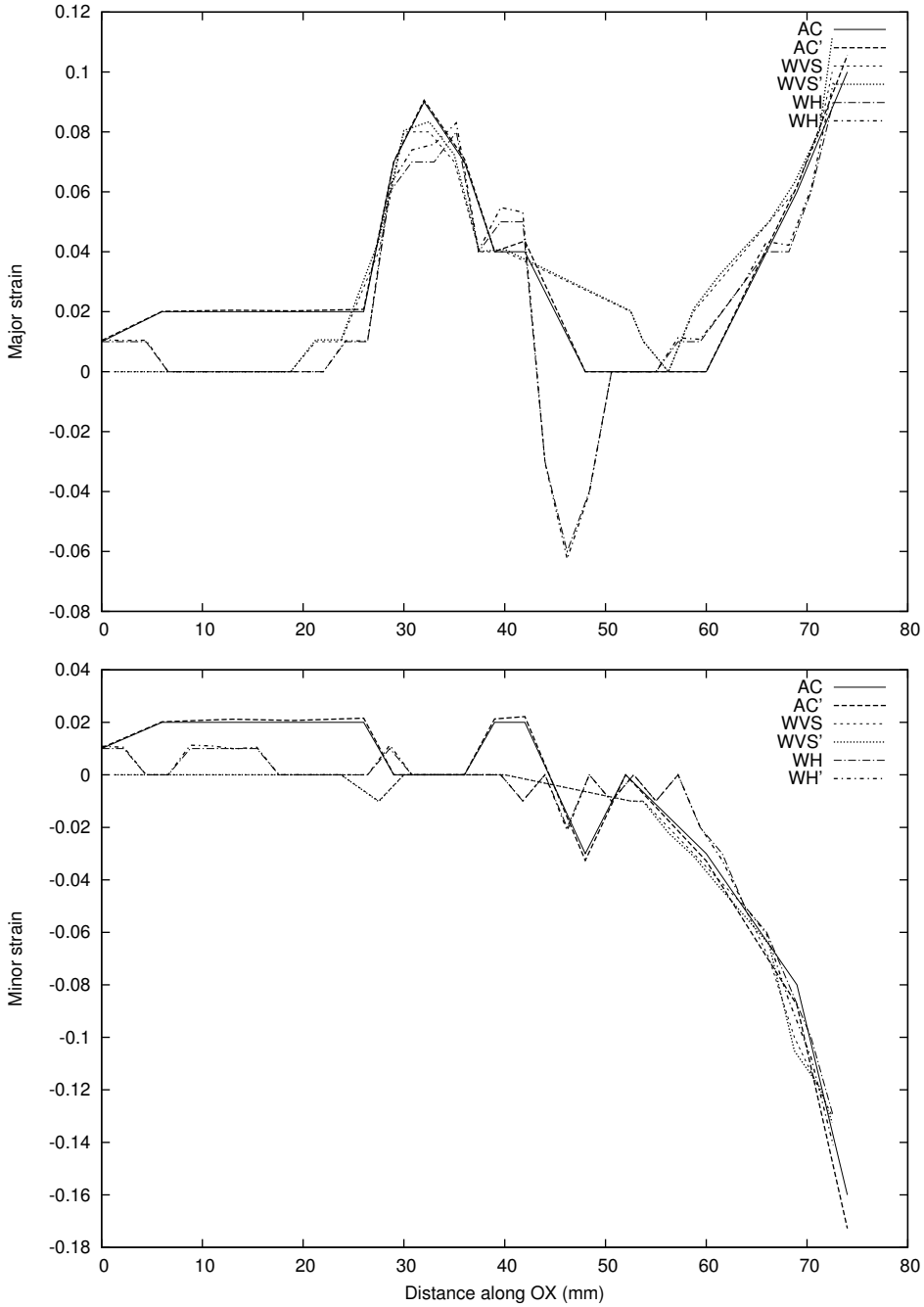

Figure 4.9: Graphs showing the principal strains for the side OX of the deep-drawing blank. The curves labelled AC′, WVS′ and WH′ refer to the new co-rotational formulation.

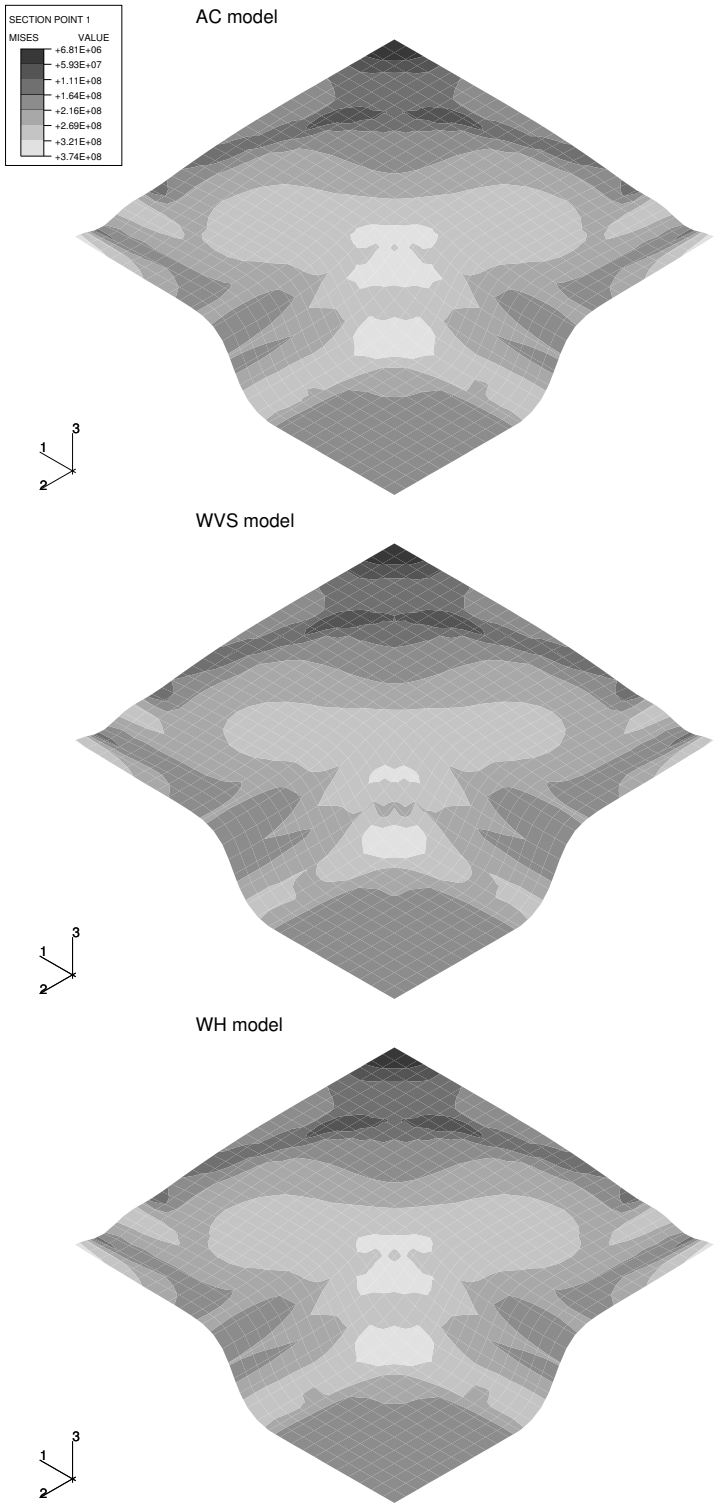

Figure 4.10: Contour plots of Mises stress distribution for the deep-drawing simulation.

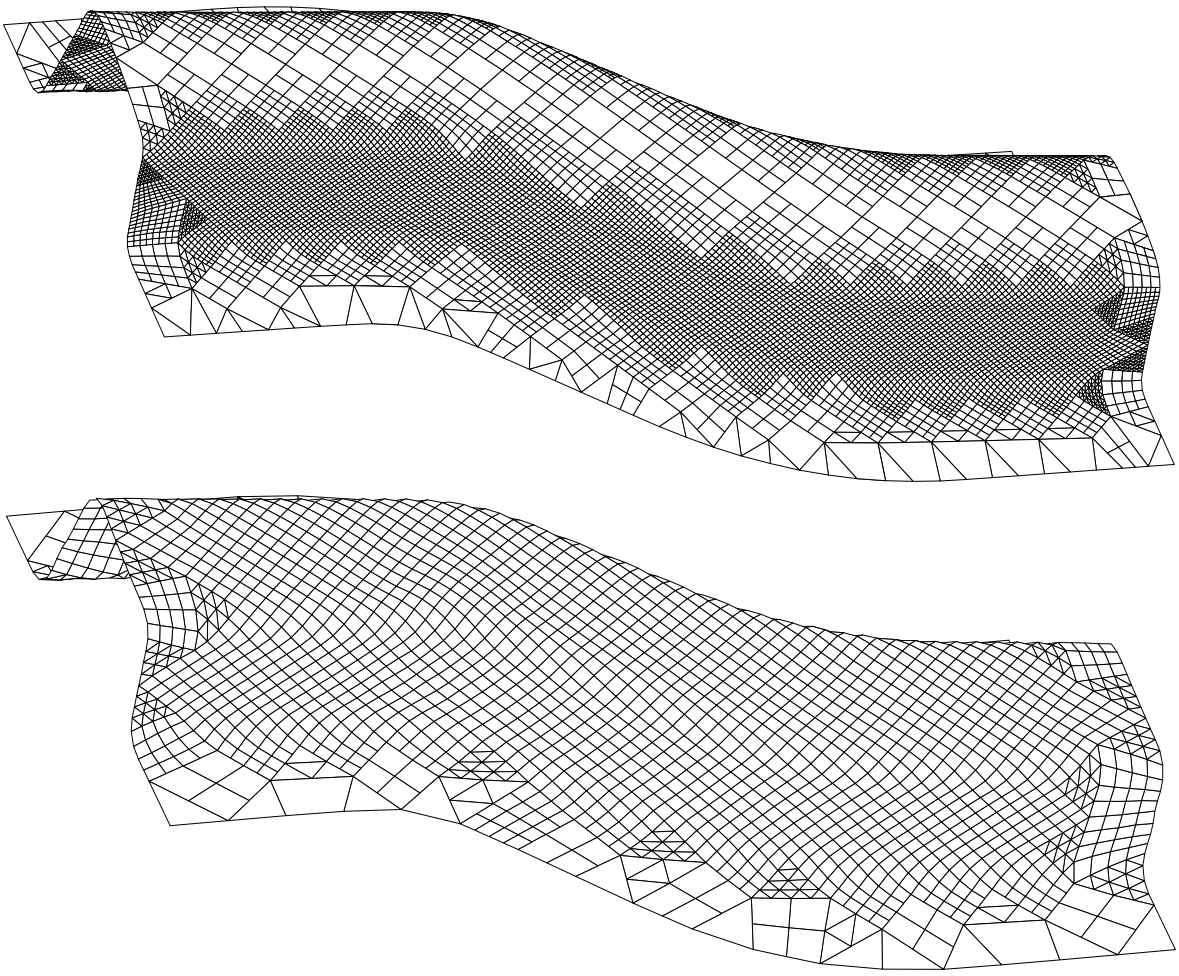

Figure 4.11: Comparison of the coarse and fine meshes showing the final deformed shape of the work piece.

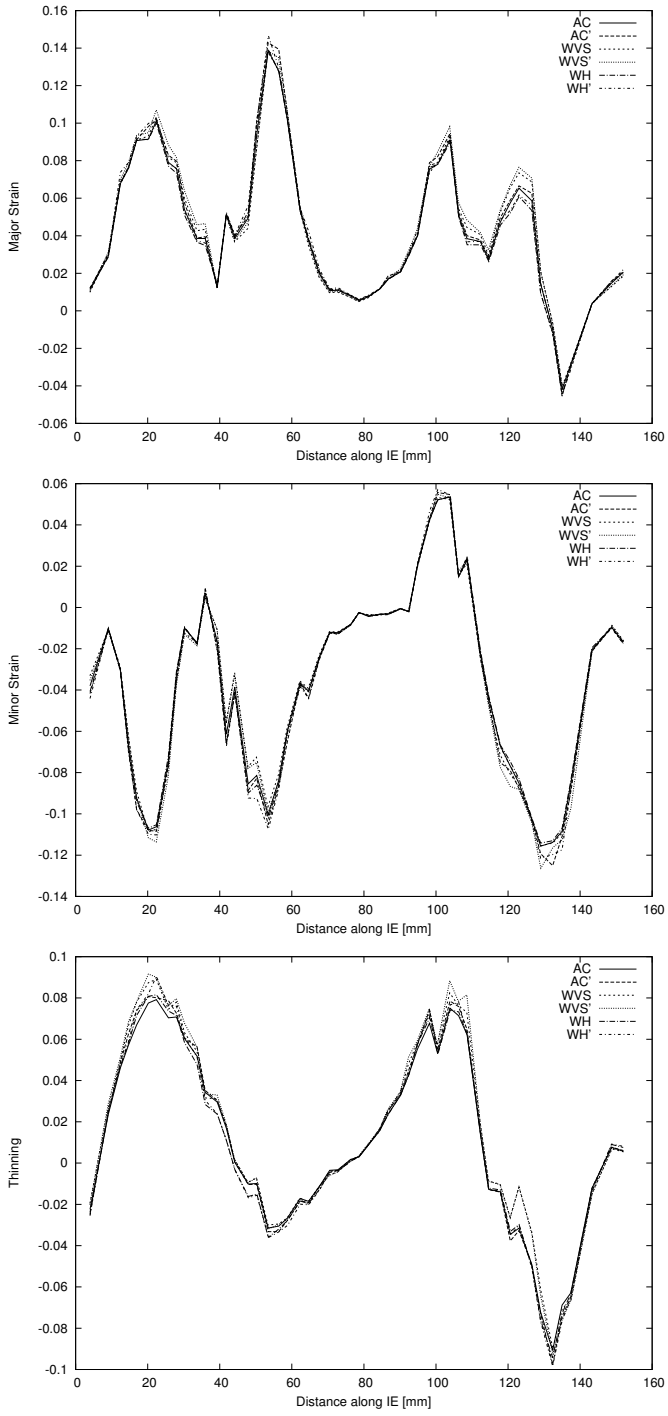

Figure 4.12: Graphs showing the principal strains for the section IE of the S-rail blank with coarse mesh. The curves labelled AC′, WVS′ and WH′ refer to the new co-rotational formulation.

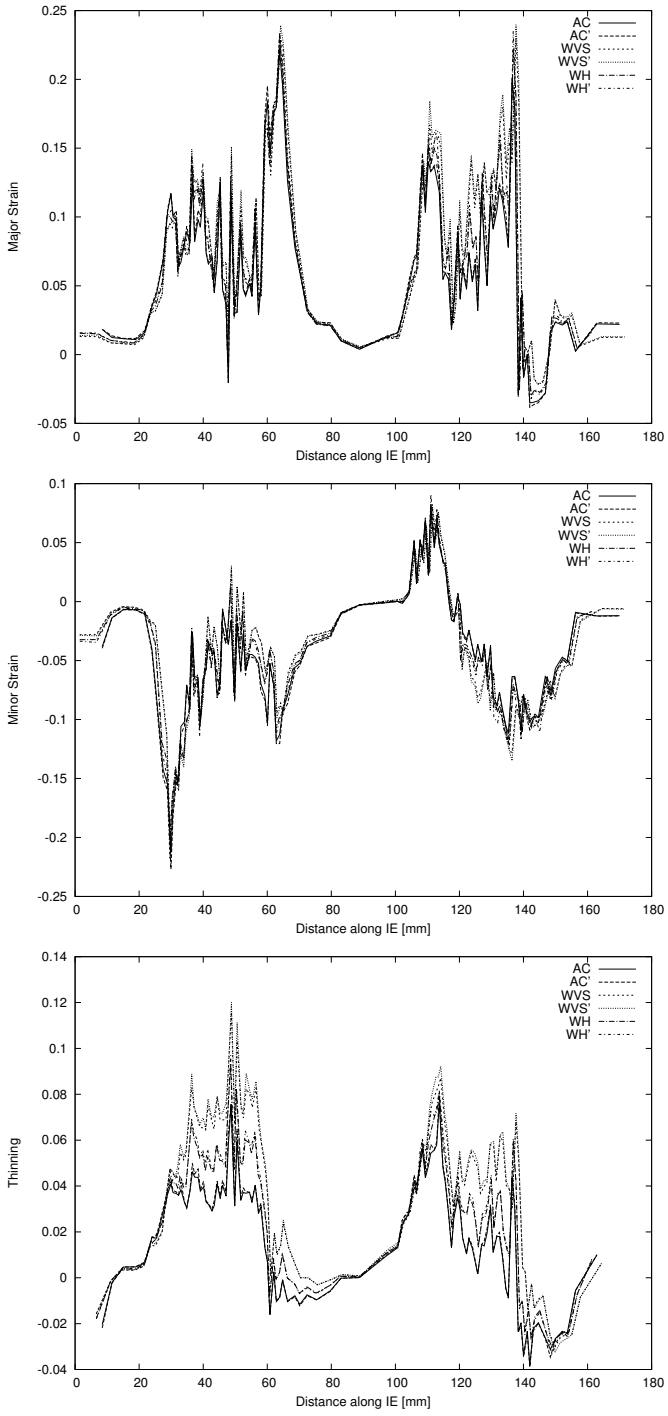

Figure 4.13: Graphs showing the principal strains for the section IE of the S-rail blank with fine mesh. The curves labelled AC′, WVS′ and WH′ refer to the new co-rotational formulation.

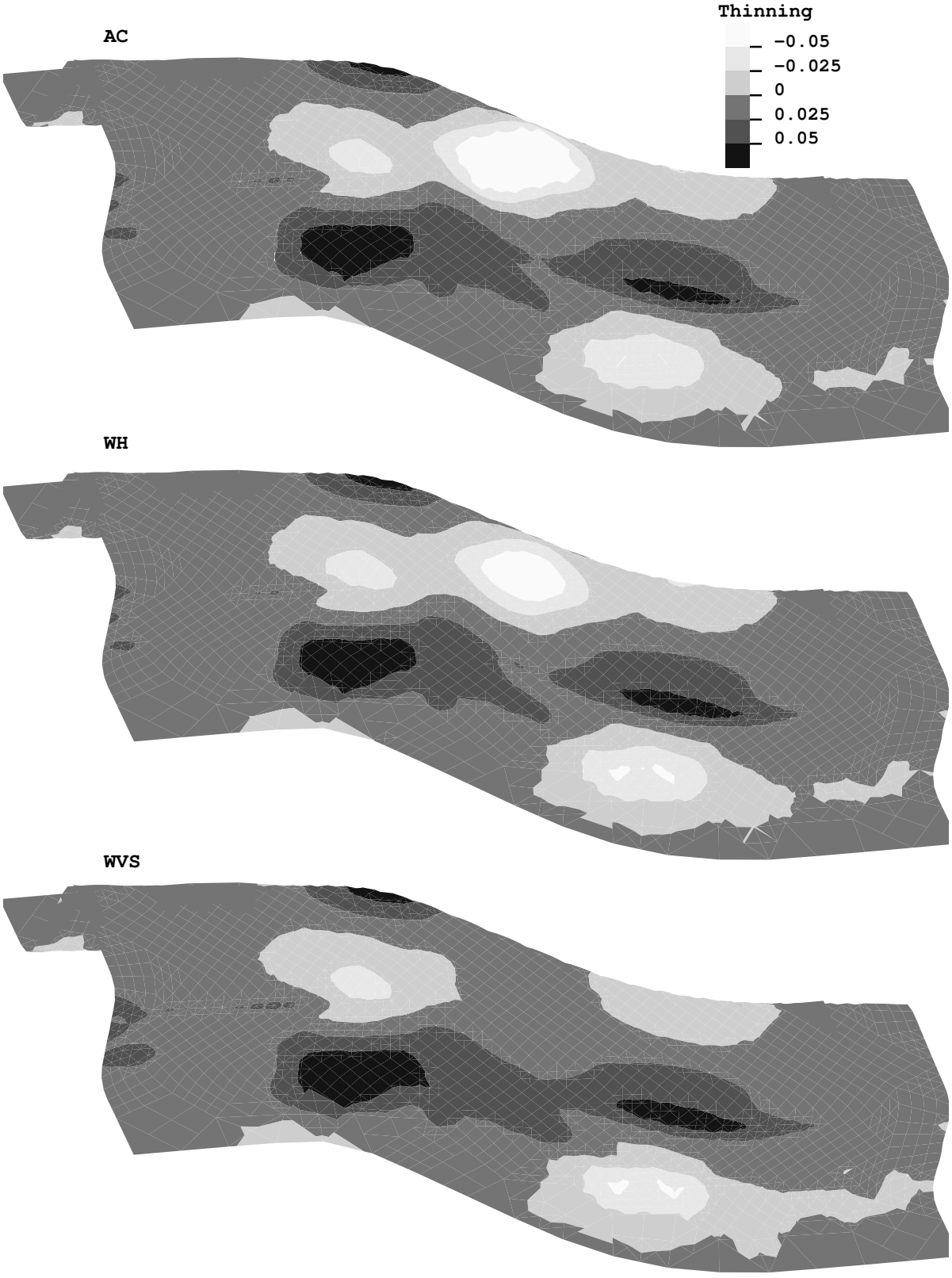

Figure 4.14: Contour plots of thinning for the coarse mesh S-rail simulation.

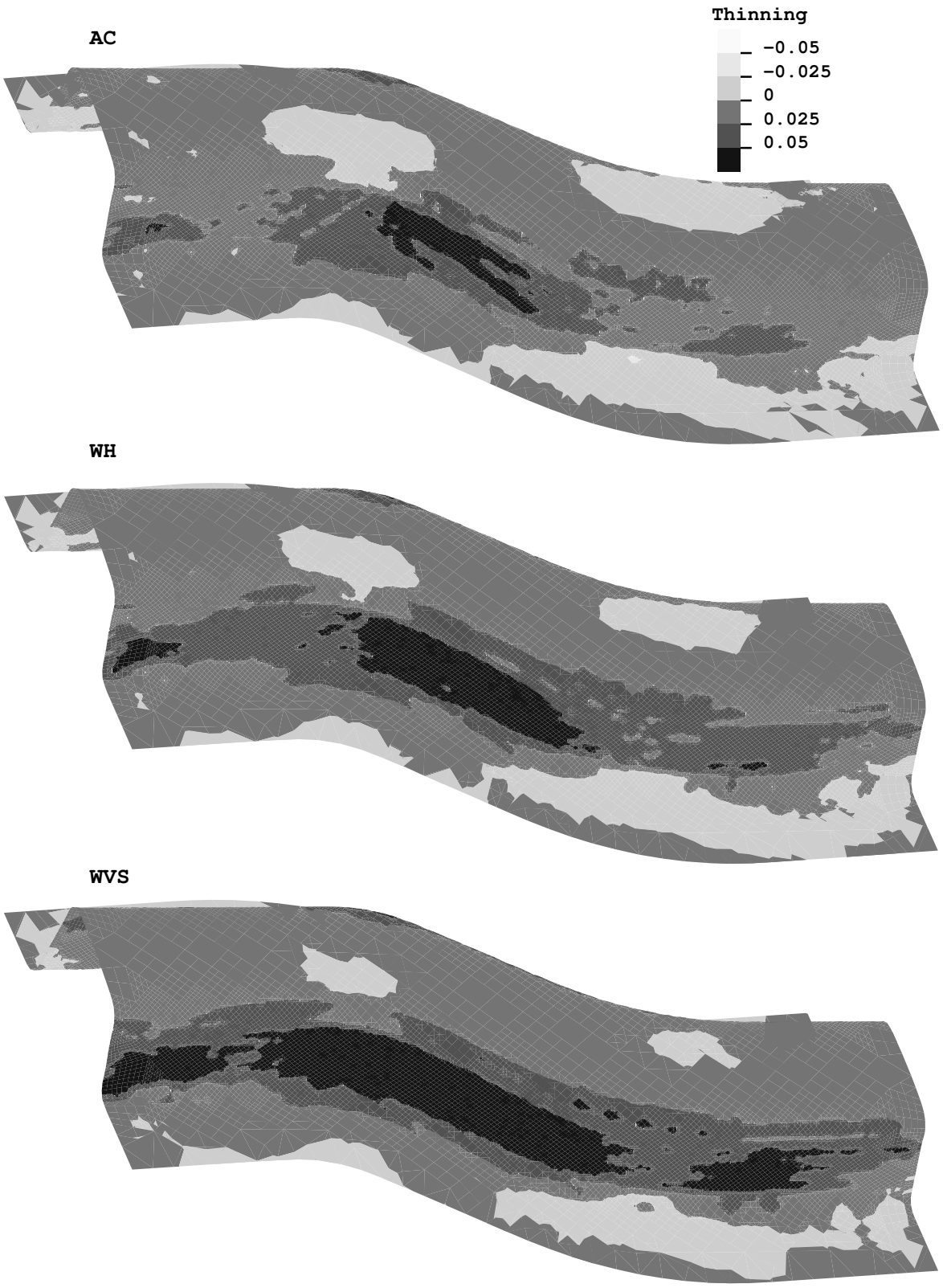

Figure 4.15: Contour plots of thinning for the fine mesh S-rail simulation.

	Along diagonal OD			
Friction model	major strain		minor strain	
	maxima	% resp. to AC	minima	% resp. to AC
AC	0.263	100	−0.262	100
WVS	0.140	53	−0.225	86
WH	0.197	75	−0.220	84

Table 4.1: Extreme values for the principal strains along the diagonal of the deep-drawing workpiece.

	Along side OX			
Friction model	major strain		minor strain at punch edge	
	maxima	% resp. to AC	extrema	% resp. to AC
AC	0.1013	100	0.0033	100
WVS	0.0800	79	−0.0100	303
WH	0.0713	70	0.0083	251

Table 4.2: Extreme values for the principal strains along the side of the deep-drawing workpiece.

	Coarse Mesh			
Friction model	major strain		thinning	
	maxima	% resp. to AC	extrema	% resp. to AC
AC	0.1278	100	0.07920	100
WVS	0.1379	108	0.08904	112
WH	0.1393	109	0.08156	103
	Fine Mesh			
Friction model	major strain		thinning	
	maxima	% resp. to AC	extrema	% resp. to AC
AC	0.2203	100	0.07502	100
WVS	0.2296	104	0.08300	111
WH	0.2245	102	0.07063	94

Table 4.3: Extreme values for the major principal strain and thinning along the line EI of the S-rail workpiece.

Friction model	coarse mesh	fine mesh
	% fric. energy	% fric. energy
AC	24.75	22.49
WVS	27.75	26.23
WH	20.01	19.93

Table 4.4: Proportion of energy devoted to frictional dissipation with respect to internal energy of the S-rail simulation.

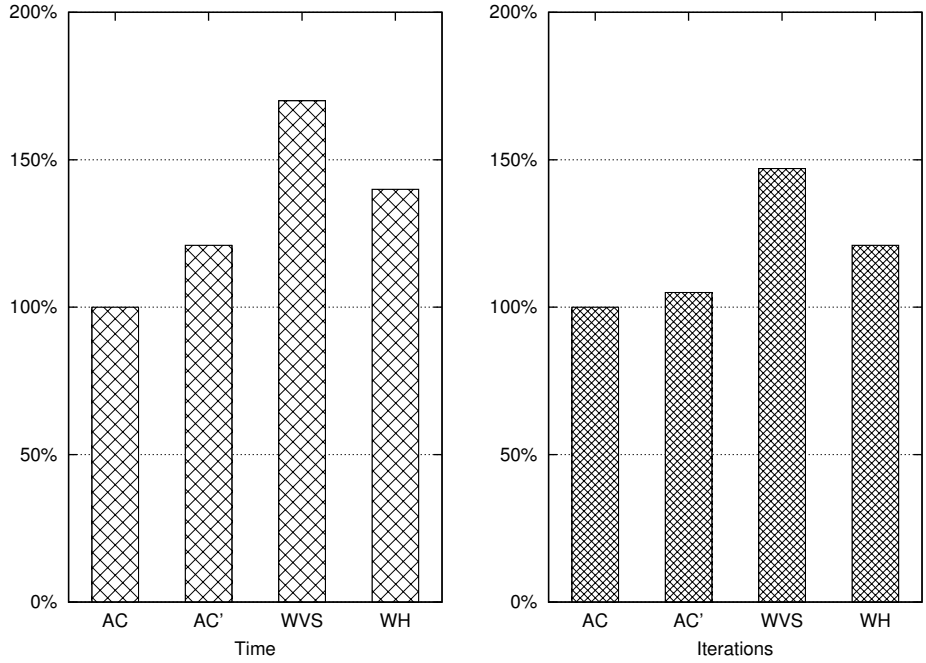

Figure 4.16: Computational performance of the square-cup deep-drawing simulation with the standard Abaqus formulation and friction model (AC), in comparison with the new formulation (AC′) and the nonlinear models (WVS and WH) which are implemented using user subroutines. Results for time and iterations are given scaled relative to the AC results (100%).

4.6 Identification of friction parameters

Experimental results from the NUMISHEET '96 conference provide measurements of the principal strains for the s-rail stamping benchmark. The values are provided along the measurement cross-section paths: figure 4.18 shows the measured values for the path IE for the 6 data sets provided. The average and standard error were calculated and are presented in figure 4.19, which also

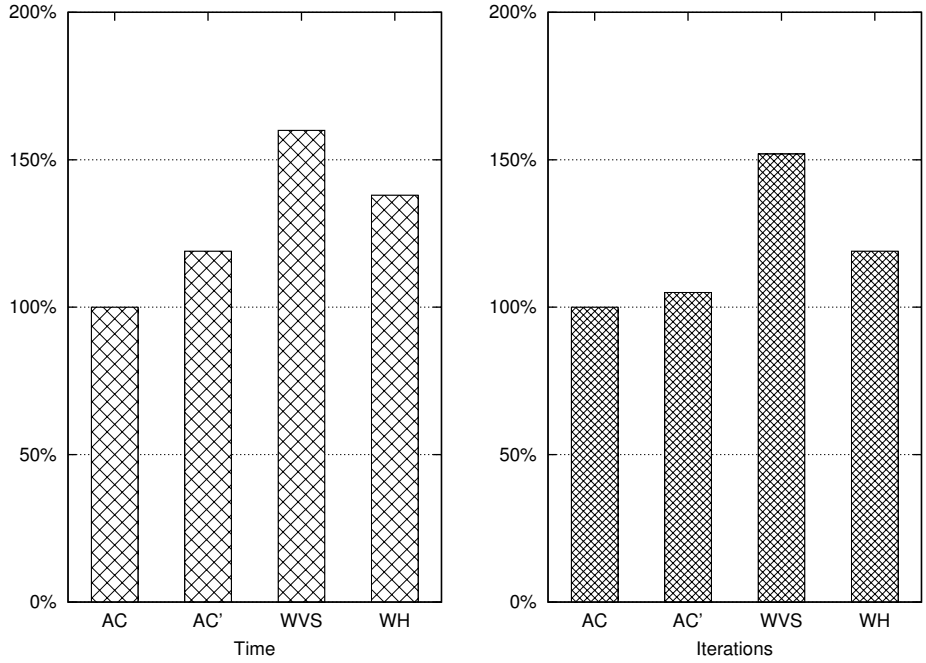

Figure 4.17: Computational performance of the S-rail stamping simulation with the standard Abaqus formulation and friction model (AC), in comparison with the new formulation (AC′) and the nonlinear models (WVS and WH) which are implemented using user subroutines. Results for time and number of iterations are given scaled relative to the AC results (100%).

shows the smoothed (interpolation) curve provided by the conference organisers.

The most significant aspect of these results is the large deviation between experimental sets and the large experimental error. It is thus difficult to say which is the “best” experimental set.

The results are presented in the table below, which shows the initial and final parameters values, as well as the percentage change in each parameter.

Also, the percentage change in the objective function is given. As this is averaged error between the simulation result and the experimental results, it indicates the degree of improvement.

		initial	final	Δ	ΔE
AC	$\mu = 0.11$		0.122	+10.9%	−8.1%
WVS	$\mu(T_N) = \alpha\, T_N^{\nu-1} + \beta$				
	$\alpha = 0.03$		0.091	+203%	−21%
	$\beta = 0.11$		0.27	+145%	
	$\nu = 0.80$		0.51	−36%	
WH	$\mu(\omega) = \alpha\,\omega + \beta$				
	$\alpha = -8.0$		-1.7×10^{-2} mm/kN	−78.8%	−17%
	$\beta = 0.11$		0.187	+70%	

There are some surprising results here. Firstly, as expected not much change for the simple AC model with its single parameter. However, the second and third results, for the WVS and WH models, differ from the initial values. In particular the WVS shows a larger difference. Now, this model has a non-linear component which is expected to be more sensitive to experimental error and also the three parameters allows for more degrees of freedom for any fit. The WH model with its two parameters and simple linear model shows a less dramatic change, but it does differ enough from the initial to make one suspect again the large experimental error.

The reduction in the objective function is modest for all three: the AC shows the least change, while the WVS and WH show larger changes. The latter two, with more parameters, allowed for more optimisation in the fit. It is

unsurprising that the objective is not much changed as it represents the average difference between simulation and experimental.

The change in parameters are more useful as this is a numerical experiment in measuring the sensitivity of these parameters to friction state variables.

Further work in this area can be undertaken, especially to make use of error and uncertainty. One approach is to eliminate outliers to "clean-up" the data by removing extreme results. Another is to include the standard error for each measurement in the analysis and make use of a more sophisticated statistical model when constructing the objective function. However, as can be seen from the experimental results of the NUMISHEET conferences, the variation between experimental data sets from different laboratories is larger than the variation between simulation result sets. This despite the latter using different formulations and models, and is the result of the large number of parameters and physical conditions that affect experiments. Statistical methods may have limited improvements to offer.

It is also the case that the rheological and tribological properties of materials are strongly correlated. For example, Knibloe & Wagoner [28] have shown that the same strain distribution can be obtained with very different friction coefficients depending on whether a quadratic or non-quadratic yield function is used in the case of a forming process with a hemispherical punch.

In conclusion, it must be kept in mind that friction is a local phenomenon, and any parameter fit from this approach is limited to this particular simulation and forming process. It would not be applicable to a different forming process, even with the same workpiece material, as forming is a path-dependent problem and a different process would undergo different stress and strain paths. The value of these numerical experiments may only be in

identifying which parameters are significant.

4.6.1 Sensitivity

An aid to identifying the significance of frictional parameters is a simple numerical sensitivity analysis [27]. Similarly to the inverse problem solution, in sensitivity analysis the gradient of the objective function is calculated, but now for the purpose of studying the effects of process parameters in the state of the final product.

There are three methods [6] usually used for calculating the sensitivities: (a) finite differences approximation, (b) the adjoint variable method or (c) the direct differentiation method. In the finite difference method, the numerical simulation is computed for two different sets of process parameters, with nearby values, and the difference of the numerical results obtained is used to calculate the sensitivities. This approach, while the simplest, usually has the largest computational cost as multiple complete simulations are made. However, as modern computers are quite powerful, and repeated numerical simulations have already been completed for the inverse problem solution, the finite differences were calculated by reusing the inverse problem intermediate results.

Model	Parameter	Sensitivity
AC	μ	6.6%
WVS	$\mu(T_N) = \alpha\, T_N^{\nu-1} + \beta$	
	α	3.4%
	β	1.3%
	ν	7.2%
WH	$\mu(\omega) = \alpha\,\omega + \beta$	
	α	2.7%
	β	2.2%

The sensitivity results compliment the inverse problem results. In the latter, modification of objective to match the experimental data drives the change in the friction parameters. In the sensitivity analysis, we measure the change in simulation result compared to a change in the friction parameters. This is confirmed in the above table: the change in AC parameter has a larger effect on final result. For WVS model the α and β parameters have a smaller effect then the exponent ν of the nonlinear term. In the case of the WH model the slope of the "smoothing" term α has a larger effect then the constant term β since, of course, for no smoothing, the WH model is equivalent to the AC model.

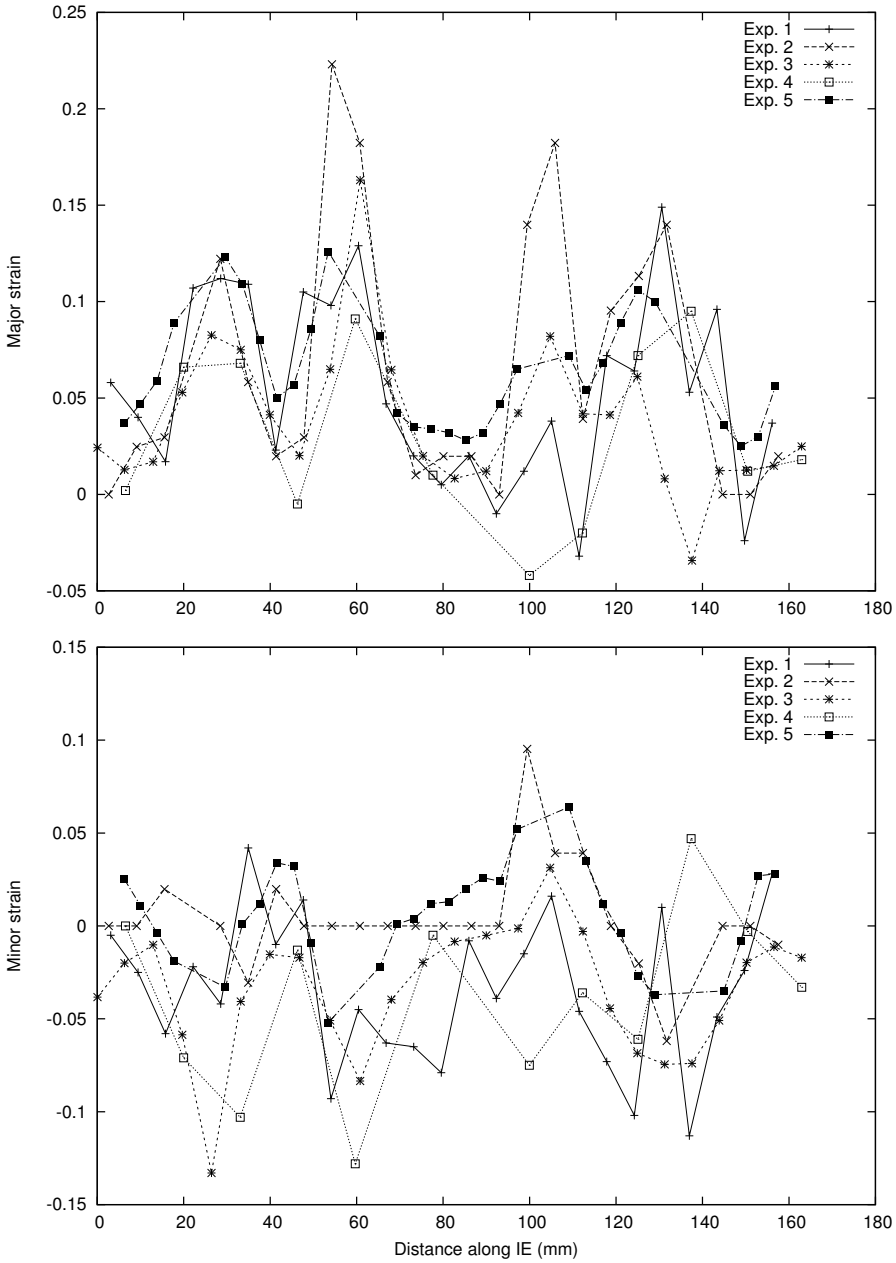

Figure 4.18: Experimental results of principal strains along path IE for the s-rail stamping benchmark from the NUMISHEET '96 conference.

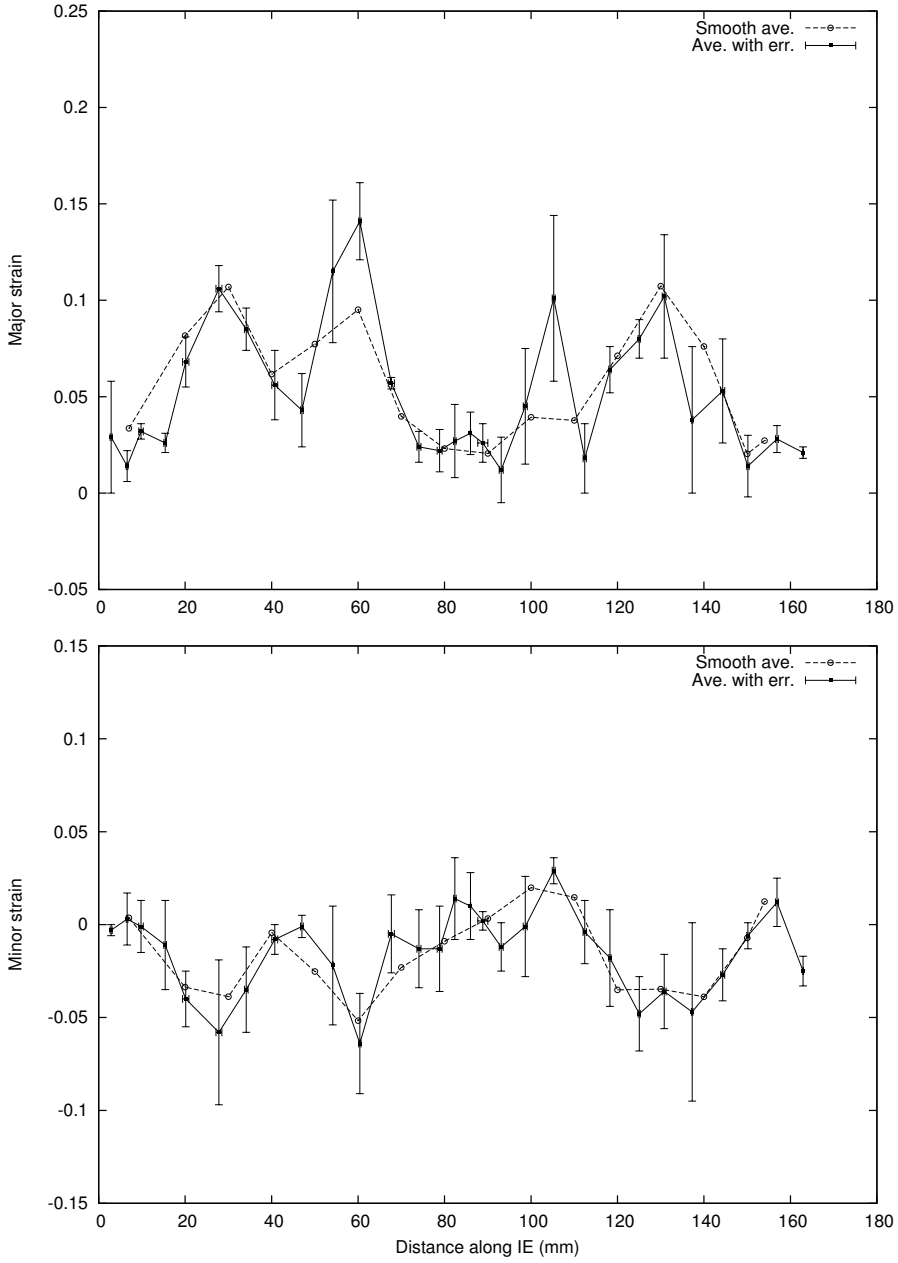

Figure 4.19: The calculated average and standard error of the experimental principal strains along diagonal IE for the s-rail stamping benchmark from the NUMISHEET '96 conference. The 'smooth' average curve is as presented by the organisers [32].

Chapter 5

Conclusions

In this report a new friction model has been presented whose kinematical formulation takes into account rotational effects by including surface and material spins. This new formulation allows for different constitutive models of friction that describe the material interaction to be incorporated.

Two benchmark metal forming simulations were simulated using the new friction model along with various constitutive friction models. Different friction models—the classic one proposed by Amontons-Coulomb (AC) with a constant friction coefficient, a three-parameter model proposed by Wriggers et. al. [76], and a model based on the concept of work-hardening' proposed by de Souza Neto, *et al.* [63]—in the standard convectional and new corotational formulations are applied to simulate benchmark problems: the 3-D square-cup drawing (NUMISHEET '93) and S-rail stamping (NUMISHEET '96). These benchmarks were conducted with both the new and standard kinematic formulations using the three constitutive friction models. The benchmark simulations were implemented in the finite element program Abaqus/Explicit [1] by using large strain shell elements and user friction routines. The results ob-

tained for three friction models in both formulations were presented to illustrate the influence of the friction model on the drawing process. The results for major and minor strains, and also contour maps of thickness changes, for the two simulations with the three friction models in the old and new formulations were presented and discussed.

For the square-cup deep-drawing results it was found that the strain results showed greatest value for the AC model, and were similar to the WH model, which is a linear extension of the AC model. In contrast, the WVS results are different in shape from the AC and WH models as its non-linear pressure-dependent term contributes additional frictional traction.

The curves for the new co-rotational formulation are almost indistinguishable from the curves of the standard formulation. The additional term arising from the new co-rotational model has a small overall effect on the results. The variation between constitutive models is much more pronounced. The results confirm that the new formulation has an effect albeit small, and that the constitutive model is the more important.

The quantitative results in the tables of extrema show the effect of the non-linear term in the WVS model, which is significant at regions of high contact pressure, like the edge of the punch. For the WH model the reduced friction for areas that experience increased sliding over the tool pieces is seen, as expected because this model accounts for smoothing ("work-softening") effects.

These observations are confirmed by the Mises stress contours that show the overall higher values for the AC model, and the similar distribution for the WH model. The lower WVS values are also shown with the key area of peak values at the corner appearing smaller in size, showing lower distribution of stress.

The s-rail results were presented for both a medium and fine element mesh. This revealed the importance of increased resolution from finer mesh as the larger elements tended to smooth out the results. The greatest distinction in the the thinning curves were larger peaks for the WVS model as a result of its higher friction forces for lower pressure regimes. This is also seen in the contour maps of thinning where the WVS model has the largest area of thinning above 5% in the wall of the s-rail.

The quantitative results show that the thinning peaks of WVS for both meshes to be some 11% 12% higher than AC, while the WH model result is close to AC but lower as the reduction in μ over larger slipping areas (representing smoothing of the workpiece surface) for the WH model has made a significant contribution to the result. This is confirmed by the table of energies: the WVS model has the highest values since the frictional forces are overall higher for lower pressure areas compared to the other two model, and the WH model shows lower values than AC as the lower μ value from the smoothing effect requires less frictional work.

The computation time for the models showed the AC model is the most efficient with shortest runtime and fewest iterations to converge. Comparing the AC model to the non-linear models (WVS and WH) there are greater increases in runtime which is mostly owing to the greater number of iterations needed. The increased computational cost needs to be balanced with the improved accuracy from advanced models.

Overall, for both benchmarks, the results show a small but measurable difference between the formulations, but this was less significant compared to the larger difference from the constitutive models. This difference illustrates the dominance of the contact frictional forces over the kinematics. Given the additional computational cost of the new formulation and the small increase

in accuracy, it can not be recommended as a general replacement.

Using experimental data from the NUMISHEET conference an inverse problem solution was performed for the three friction models in order to identify what values the friction model parameters would be in order for the simulation results to better match the experimental results.

The results presented for the inverse problem solution compared the initial values for these friction parameters, as derived from measurements of frictional contact and material data, to the inverse problem result. The simple AC model with its single parameter, μ had the smallest change of 11%. The WVS, which has a non-linear term, had larger change to its three parameters, α, β, and μ, from 36% to 206%. While the WH model, with two parameters and linear relation, deviated by 79% and 70%.

The identification of friction parameters proved to be less feasible than hoped owing to two main factors. Firstly, the experimental data have large variation, as was demonstrated by the analysis of the S-rail data. Secondly, drawing simulations are strongly path dependant computations with internal factors contributing to the overall result in a not insignificant measure. It can not be assumed that only surface interaction variation matters.

The results for the WVS and WH models proved to provide some challenging numbers. While experimental error is large, the initial values chosen for the friction parameters were based on best available data for these models. This topic requires further work. However, one promising result is the identification of which parameters, measured by difference, are more sensitive.

The sensitivity analysis showed that the solution is strongly sensitive to the AC model constant μ, which is not surprising as this is the only parameter an adjusting it would directly affect frictional contact. The non-linear pressure

dependent term of the WVS model had the largest sensitivity as expected. The WH model showed that both its parameters where almost equally significant in affecting the result, which differs slightly from the inverse problem result where one term changed more than the other. The latter is most likely due to the wide range of variation in the experimental data.

This research has made two contributions to the modelling of friction in metal-forming simulations. Firstly, a new co-rotational kinematic formulation of the friction evolution equations has been proposed and implemented in the finite element method. Secondly, two benchmark drawing problems have been simulated using three different friction models in the standard and new kinematic formulations. This comparison of friction models includes a numerical inverse problem solution to identify friction parameters from experimental data, and a sensitivity analysis to identify which parameters of the friction models are more significant in their effect on the simulated metal-processing results.

The overall conclusion of this work is that frictional kinematics can be improved, although the effective improvement in accuracy is small relative to the standard approach.

Future work on this approach to modelling would start with applying the new formulation to other benchmark problems that are known to depend on frictional effects. The Numisheet conferences provide a range of benchmarks to explore.

The one concern is that experimental data has wide variation owing to many factors and that a definite answer to which model is best will be elusive.

It is also worth exploring the sensitivities [34] of the benchmark simulations to specific parameters. The inverse problem results suggest strongly

that some parameters are more significant. However, as this varies between benchmarks this has to be done carefully and the results should be analysed in detail to determine the friction model specific sensitivities from the overall work flow sensitivities. Deep-drawing simulations are very path-dependent problems and bulk effects can influence contact effects non-linearly.

Another area of future work involves simulation of the test and calibration procedures used to determine frictional parameters. The WH model, for example, depends on a specific measurement procedure [63](§4) and curve-fitting is used to determine the appropriate parameters. Instead, as the measurement process is a much simpler problem than the complex drawing process, an inverse-problem approach may reveal better fits. The simpler process is cheaper and easier to perform than drawing and can thus be repeated more often under controlled laboratory conditions with better experimental data the result.

An interesting alternative to the classical inverse problem is the use of a machine learning (ML) models [41]. The ML model is trained using the usual FEM simulation of the benchmark with the chosen friction model over a wide range of friction parameters. This set should be large enough to cover the full range of experimental deviations. Then the ML model is used in inference mode on the experimental data to derive an estimation for the friction parameters. This approach has had success when applied to linear and non-linear mixed conduction-convection problems in which the boundary conditions are determined by providing only a few temperature measurements [66].

Appendix A

Case study: Production stamping defect simulation with finite element method

Note:

This appendix describes a real-world stamping simulation where frictional effects contribute in a significant manner to the generation of defects in the production process. It is the exploration of the role that friction plays that provides motivation for more accurate friction modelling and this case study preceded and stimulated the work presented in this thesis. The case study is included here as an appendix to provide additional background for the interested reader.

A real production problem is illustrated using the finite element code PAM-STAMP (version 1999) to simulate and redesign the tool pieces for the stamping of an inner panel for a light motor vehicle. The design aim is to eliminate

problems such as splitting and wrinkling associated with the variability in the steel supply.

A.1 Introduction

The finite element method (FEM) is a successful numerical method for the solution of partial differential equations (PDEs) associated with the simulation of solid mechanical problems. The FEM has matured to the point where quality commercial codes are available addressing a wide range of simulation problems. One of the most popular applications of these codes is to stamping processes as this is a widespread manufacturing technique, with design challenges. Problems in stamping arise from the intricate shapes desired, and variability in material properties of the sheet metal which occurs between suppliers and batches. However, while such codes allow quick and easy simulation of stamping processes, analysis by an engineer experienced with the actual process is necessary.

Stamping can exhibit many problems and defects as competitiveness forces manufacturing to design more complicated parts at lower production cost, i.e. with thinner and less material. In the motor industry the panels that make up the body of vehicles may have elaborate shape and serve the function of holding other parts in place. Thus channels, grooves, dips and other indentations are required not for the strength of the panel but to accommodate other parts of the vehicle. Cost considerations require that each panel be formed in one stamping operation, if possible.

The more complex the shape the more likely that the defects of tearing and wrinkling occur as small-sized features on the panel introduce local regions of high resistance affecting material flow. The traditional method of controlling

these is to introduce drawbeads [67, 68] and other features to increase resistance in key areas, and to flatten and smooth other areas, increasing radii of curves, in order to reduce resistance.

Friction plays a key role in the stamping processes [57] and more realistic models of friction have been implemented to increase the accuracy of metal working simulations [58].

A.2 Stamping Process

A panel from the inside wall of the engine compartment of a light commercial vehicle is to be manufactured by a single stamping operation on a triple-action press. The press is fixed, and the parameters that can be varied include the load on the holders and the speed of the ram moving the punch. The sheet metal is supplied in bulk but the quality varies over a wider range than anticipated. The original design cannot be changed much as it must fit in with other parts of the vehicle. Figure A.1 shows the shape of the die; this represents the desired shape for the final panel and cannot be modified to alleviate defects. However, the blank holders can be changed and their shape and size will influence the flow of the blank. Figure A.4 shows the initial holder shape.

Triple action press

The triple action press consists of three stages which are performed as part of a single stamping operation with variations of load and speed over each stage. Figure A.2 illustrates each stage of the stamping. Initially the tools are at rest in predetermined positions. The first part of the operation is the closing of the binders clamping the workpiece between them. The curvature of the holders

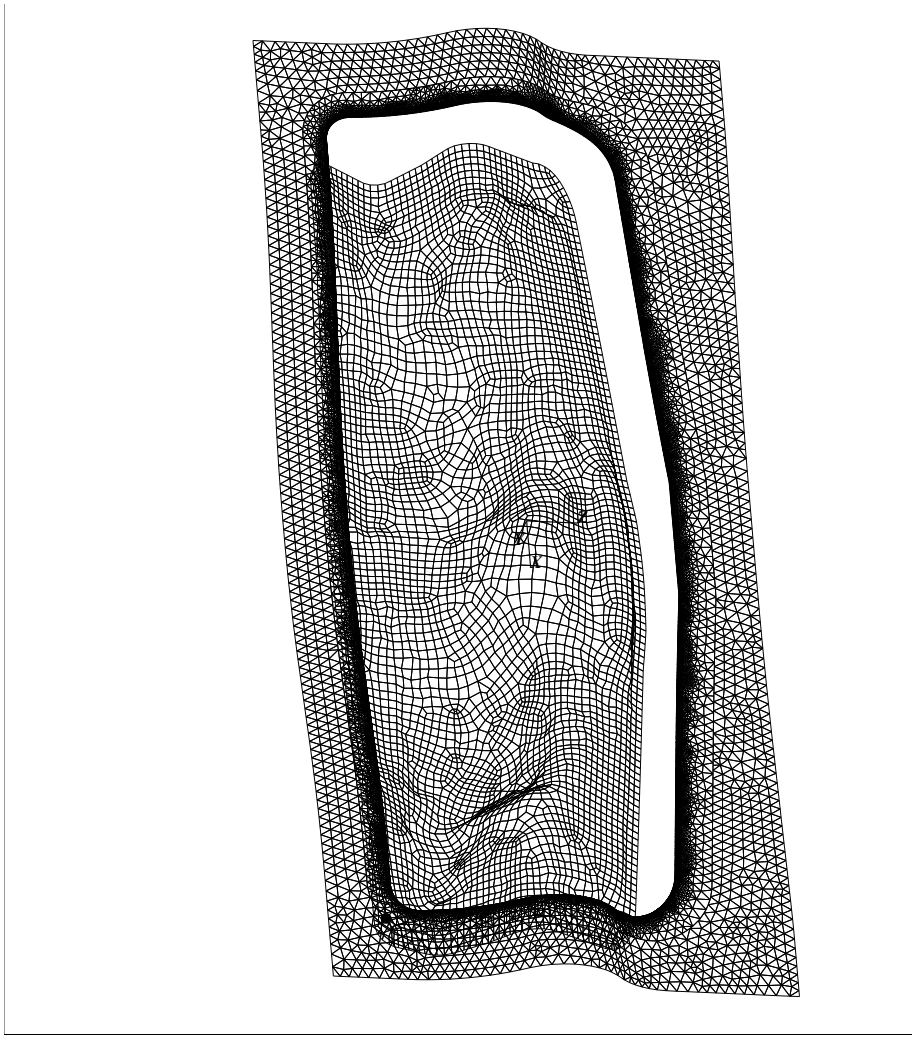

Figure A.1: Shape of the die. The complexity of the shape required many elements to model. The blankholder is also shown in its initial position.

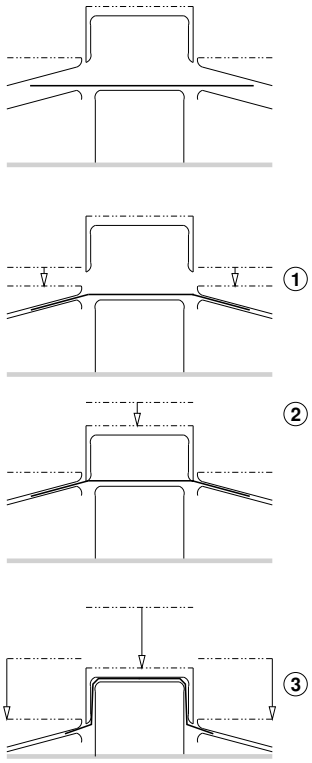

Figure A.2: Schematic showing the steps involved with the triple action press: (1) close holders; (2) move die into position; (3) form shape against punch.

induces some deformation in the blank during this step. The second stage of the press involves the motion of the die downwards until it touches the blank. Little deformation occurs here. The third stage is the forming step and the die, holders and blank move together over the punch.

PAM-Stamp is able to set up a triple-action press simulation with little effort using the basic parameters. Where necessary, the load and velocity curves were modified to conform to the known conditions.

Loading and boundary conditions

The load on the holders is not constant and is provided by gas springs which start with a low load and then increase until 'bottoming out' at the maximum. This was simulated by using the curve in figure A.3 which shows the factor applied to the set load of 400 N as it varies over the time of the stamping.

The punch is fixed, and velocity boundary conditions are applied to the die and upper blank holder. The speed during the holding stage is 2 m/s, and during the forming step is 5 m/s.

Draw beads

Two shapes of drawbeads were used with radii of 6 and 8 mm. PAM-Stamp version 1999 did not model drawbeads directly[1] as their small features would require a very fine FE mesh with an increased computational expense. Instead special FE bar elements are laid along the path of the drawbeads and these apply an equivalent force tangential and normal to the surface representing

[1] More recent versions of PAM-STAMP have improved contact accuracy and this is no longer necessary [18].

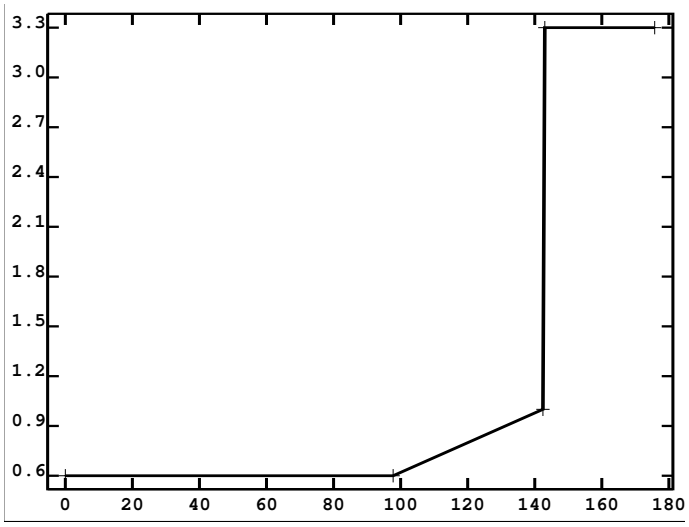

Figure A.3: Loading factor over time for the blankholder. Load is factor times 400 N.

Drawbead size	F_T	F_N
6 mm	0.05 N/mm	0.03 N/mm
8 mm	0.07 N/mm	0.07 N/mm

Table A.1: Equivalent drawbead calibration results for pulling (F_T) and clamping (F_N) resistances.

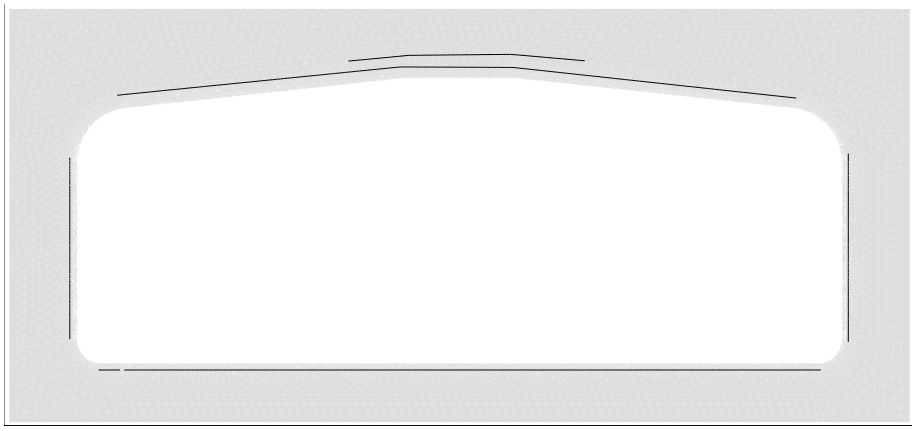

Figure A.4: Initial blankholder showing drawbead shape and position.

the resistance to drawing and closing. A separate application uses the geometry of the drawbead and the properties of the blank to calculate these forces. Once 'calibrated' this way the values can be used and easily modified to reflect changes in the drawbeads. This use of equivalent drawbeads is efficient and accurate [36]. The calibrated values for the two drawbeads are shown in table A.1.

Drawbeads are the preferred way of adjusting material flow as they can easily be removed (by grinding) and applied (by welding) whereas any changes to the holders requires more extensive operations: casting and machining.

Friction

The complexity and large element sets of the simulation preclude more realistic, but more computationally expensive, friction models. The standard Amontons-Coulomb model was used with $\mu = 0.1$ from measurements of similar steel-steel contact with synthetic solid lubricant.

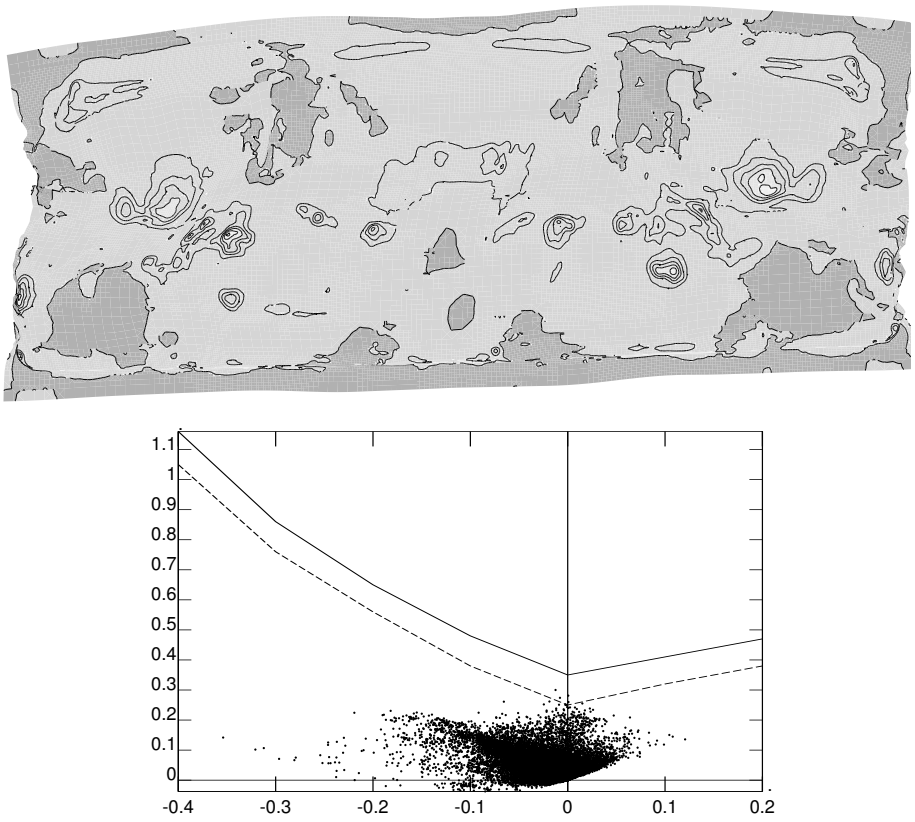

Figure A.5: Original drawbead configuration: contour plot of thickness (above), and FLD (solid line is FLC, dashed line is safety margin).

A.3 Results

Original configuration

Figure A.4 shows the position and lengths of the original drawbead configuration on the lower blank holder. All beads have 6 mm radii. The long beads on the left and right sections were an attempt to prevent the early separation of

blank from those edges of the holder.

This was unsuccessful as figure A.5 shows that the short edges of the blank are wrinkled. Figure A.5 plots the thickness of the formed panel at the end of the stamping process.

The forming limit diagram (FLD) in figure A.5 shows the lack of tearing with no points above the forming limit curve (FLC), but here the problem is wrinkling, as indicated by the many data points in negative minor strain.

Final configuration

In order to reduce the wrinkling the drawbeads on the short edges were increased to 8 mm radii. However, this introduced excessive thinning leading to cracking and tearing and so the drawbeads along the longer side were reduced in length to allow more material to flow at the corners as shown in figure A.6. The increased resistance from the new drawbeads controlled wrinkling as can be seen in figure A.7.

The distribution of the final thickness shown in figure A.7 an improvement over the initial results. however, there are some small spots of excessive thinning shown in figure A.7 which could be problematic.

The FLD in figure A.7 shows some dangerous tendencies towards splitting with a few points above the FLC, however, the overall distribution is reasonable.

The new drawbeads were implemented and experimental pressings showed that these areas did not in reality become as thin as suggested by the contour plot or the FLD in figure A.7.

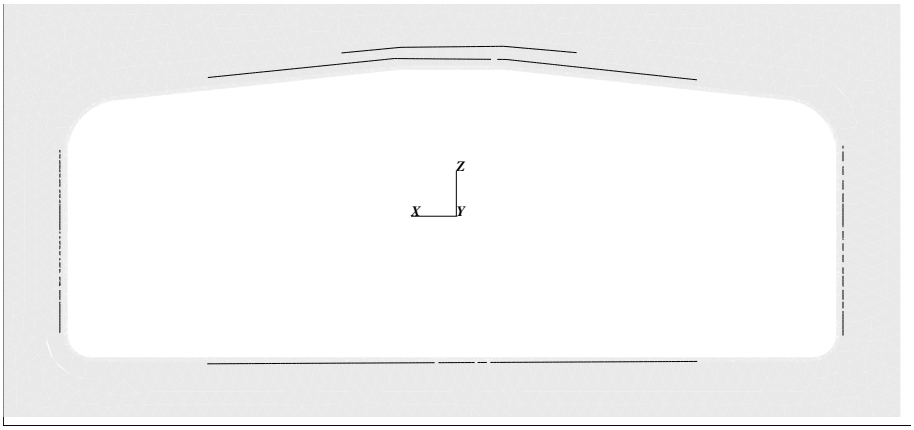

Figure A.6: Final blankholder showing new drawbead shape and position.

A.4 Comments

An industrial stamping process with production problems has been successfully analyzed with the aid of FEM simulation. The entire setup, simulation and virtual testing took three months of time and was carried out by an experienced engineer working with the FEM analyst. The engineer used his knowledge of stamping faults and previous cures to guide the redesign of the process. Since PAM-Stamp models drawbeads with simple bar elements it was very easy and quick to change these without having to redo the CAD file and mesh creation.

The final results of the simulation indicated the preferred configuration of drawbeads which was confirmed by experiment. After some minor modifications made on the factory floor, that configuration was implemented in the production press and proved itself.

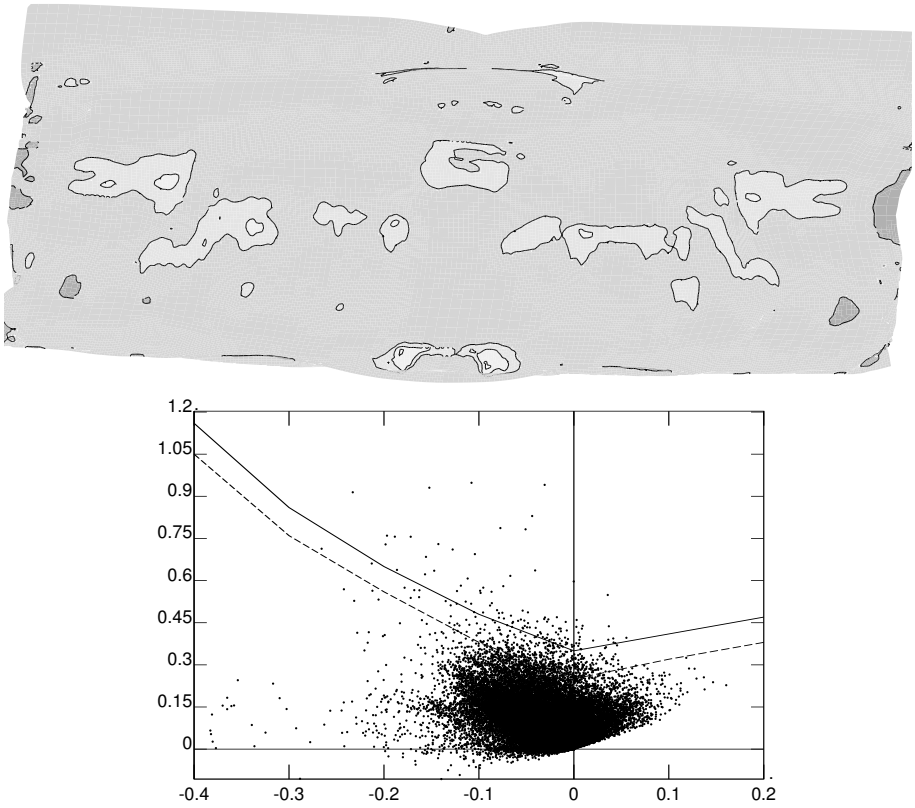

Figure A.7: New drawbead configuration: contour plot of thickness (above), and FLD (solid line is FLC, dashed line is safety margin).

Bibliography

[1] Abaqus 6.11 documentation: *Abaqus Analysis User's Manual.* and *Abaqus Theory Manual.* (Dassault Systèmes, Providence, RI, USA.) 2011.

[2] AGELET DE SARACIBAR, C., A new frictional time integration algorithm for large slip multi-body frictional contact problems, *Comput. Methods Appl. Mech. Engrg.* **142** (1997) 303–334.

[3] L. ANAND, A constitutive model for interface friction, *Computational Mechanics* **12** (1993) 197–213.

[4] B. AVITZUR, *Handbook of Metal-Forming Processes.* (New York, NY: John Wiley & Sons) 1983.

[5] A.I. BALTOV, A.G. NEDEV An approach to the modelling of contact friction during rolling *Journal of Materials Processing Technology* ***53*** (1995) 695–711.

[6] S. BADRINARAYANAN, NICHOLAS ZABARAS A sensitivity analysis for the optimal design of metal-forming processes *Comput. Methods Appl. Mech. Engrg.* ***129*** (1996) 319–348.

[7] K-J. BATHE, *Finite Element Procedures in Engineering Analysis.* (Englewood Cliffs, NJ: Prentice-Hall) 1982.

[8] TED BELYTSCHKO, WING KAM LIU, BRIAN MORAN & KHALIL ELKHODARY *Nonlinear Finite Elements for Continua and Structures, 2nd Edition.* (New York: John Wiley & Sons) 2014.

[9] F.P. BOWDEN & D. TABOR. *The Friction and Lubrication of Solids, Part I.* (London: Oxford University Press) 1950.

[10] F.P. BOWDEN & D. TABOR. *The Friction and Lubrication of Solids, Part II.* (London: Oxford University Press) 1964.

[11] F.P. BOWDEN & D. TABOR, *Friction and Lubrication.* (London: Methuen) 1967.

[12] R. BUCZKOWSKI & M. KLIEBER, Finite element analysis of elastic-plastic plane contact problem with nonlinear interface complience. *Journal of Theoretical and Applied Mechanics* **30**(4) (1992) 855–883.

[13] A. CAMERON, *Basic Lubrication Theory,* third edition. (Chichester: Ellis Horwood) 1981.

[14] H. CHRISTENSEN, Stochastic models for hydrodynamic lubrication of rough surfaces. *Proceedings of the Institute of Mechanical Engineers* **104** 1 (1970) 1013–1022.

[15] K.W. COLVILLE *The Influence of Friction on Metal-Forming Process Simulations.* (Cape Town: University of Cape Town *M.Sc.* dissertation) 1994.

[16] A. CURNIER, A theory of friction. *International Journal of Solids and Structures* **20**(7) (1984) 637–647.

[17] E.A. DE SOUZA NETO, K. HASHIMOTO, D. PERIC & D.R.J. OWEN, A phenomenological model for frictional contact of coated steel sheets. Presented at NUMISHEET '93, the Second International Conference on

Numerical Simulation of 3-D Sheet Metal Forming Processes, Isehara, Japan, 31 August – 2 September 1993.

[18] ESI PAM-STAMP, "Geometrical Drawbeads". Retrieved from https://www.esi-group.com/software-solutions/virtual-manufacturing/sheet-metal-forming/pam-stamp/geometrical-drawbeads

[19] D.D. FULLER, Friction. In: T. Baumeister, E.A. Avallone & T. Baumeister III (eds.), *Mark's Standard Handbook for Mechanical Engineers,* 8th edition. (New York, NY: McGraw-Hill) 1978.

[20] GONOSKOV, A., WALLIN, E., POLOVINKIN, A. *et al.* Employing machine learning for theory validation and identification of experimental conditions in laser-plasma physics. *Scientific Reports* **9**, 7043 (2019).

[21] J.H. HEEGAARD & A. CURNIER, Geometric properties of 2D and 3D unilateral large slip contact operator. *Computer Methods in Applied Mechanics and Engineering* **131** (1996) 263–286.

[22] A. HEEGE & P. ALART, A frictional contact element for strongly curved contact problems. *International Journal for Numerical Methods in Engineering* **39**(1) (1996) 165–184.

[23] P. HEILMANN & D.A. RIGNEY, An energy-based model of friction and its application to coated systems. *Wear* **72** (1981) 195–217.

[24] J. HOL, M.V. CID ALFARO, MATTHIAS B. DE ROOIJ, VINCENT T. MEINDERS, Advanced friction modelling for sheet metal forming. *Wear* **286–287** (2012) 66–78.

[25] J. HOL, T. MEINDERS, M.B. DE ROOIJ, A.H. VAN DEN BOOGAARD Multi-scale friction modeling for sheet metal forming: The boundary lubrication regime. *Tribology International* **81** (2015) 112–128.

[26] N. KIKUCHI & J.T. ODEN, *Contact Problems in Elasticity: A Study of Variational Inequalities and Finite Element Methods.* SIAM Studies in Applied Mathematics 8 (Philadelphia: SIAM) 1988.

[27] KLEIBER, M. & SOSNOWSKI, W. Parameter sensitivity analysis in frictional contact problems of sheet metal forming. *Computational Mechanics.* ***16*** *(1995) 297–306.*

[28] J.R. KNIBLOE & R.H. WAGONER, Experimental investigation and finite element modeling of hemispherically stretched steel sheet, *Metallurgical Transactions A* **20** (1989) 1509–1521.

[29] KLARBRING, A. Large displacement frictional contact: a continuum framework for finite element discretization, *Eur. J. Mech., A/Solids* **14** (1995) 237–253.

[30] I.V. KRAGELSKY, M.N. DOBYCHIN & V.S. KOMBALOV, *Friction and Wear: calculation methods.* Translated from the Russian by N.S. Standen (Oxford: Pergamon Press) 1982.

[31] LAURSEN, T.A., The convected description in large deformation frictional contact problems, *Int. J. Solids Structures* **31** (1994) 669–681.

[32] J.K. LEE, Benchmark Data and Results [CD-ROM] NUMISHEET '96, September 29 – October 3, 1996, Dearborn, Michigan, USA.

[33] LEVANOV, A.N., Tests for contact friction in metal pressure forming, *Kuznechno-Shtampovochnoe Proizvod. — Obrab. Mater. Davleniem,* 2013, **2**, 43–47.

[34] A. MAIA, M.C. OLIVEIRA, A. ANDRADE-CAMPOS, L.F. MENEZES Sensitivity Analysis for Numerical Sheet Metal Forming Processes *Key Engineering Materials* **651-653** 2015 1369–1374 [From the 18th International

ESAFORM Conference on Material Forming (ESAFORM 2015), April 15-17, 2015, Graz, Austria.]

[35] S.M. MAHDAVIAN & Z.M. SHAO, Isoviscous hydrodynamic lubrication of deep drawing and its comparison with experiment. *Journal of Tribology* **115** (1993) 111–118.

[36] MEINDERS, T. AND GEIJSELAERS, H.J.M. AND HUÉTINK, J., Equivalent drawbead performance in deep drawing simulation. Ed.: Gelin, J.C. and Picart, P., *Proceedings of NUMISHEET '99* (1999) 243–248.

[37] MICHALOWSKI, R. AND Z. MROZ, Associated and nonassociated sliding rules in contact friction problems, *Arch. Mech.* **30** (1978) 259–276.

[38] J.T. ODEN & E.B. PIRES, Nonlocal and nonlinear friction laws and variational principles for contact problems in elasticity. *Journal of Applied Mechanics* **50** (1983) 67–76.

[39] J.T. ODEN & E.B. PIRES, Numerical analysis of certain contact problems in elasticity with non-classical friction laws. *Computers & Structures* **16** (1983) 481–485.

[40] J.T. ODEN & E.B. PIRES, Algorithms and numerical results for finite element approximations of contact problems with non-classical friction laws. *Computers & Structures* **19** (1984) 137–147.

[41] OISHI, ATSUYA & YAGAWA, GENKI. Computational mechanics enhanced by deep learning. *Computer Methods in Applied Mechanics and Engineering* ***327***. (2017)

[42] N. PATIR & H.S. CHENG, An average flow model for determining effects of three-dimensional roughness on partial hydrodynamic lubrication. *Journal of Lubrication Technology* **100** (1978) 12–17.

[43] N. PATIR & H.S. CHENG, Application of an average flow model to lubrication between rough sliding surfaces. *Journal of Lubrication Technology* **101** (1979) 220–230.

[44] D. PERIC & D.R.J. OWEN, Computational model for 3-D contact problems with friction based on the penalty method. *International Journal for Numerical Methods in Engineering* **35** (1992) 1289–1309.

[45] D. PERIC, D.R.J. OWEN, M. SCHONAUER & E.A. DE SOUZA NETO, Computational strategies for finite strain plasticity problems including adaptivity concepts. Presented at FEMSA93, the Twelfth Symposium on Finite Elements in South Africa, University of Pretoria, 7–9 July 1993.

[46] ELENA POPOVA & VALENTIN L. POPOV The research works of Coulomb and Amontons and generalized laws of friction *Friction **3**(2)* (2015) 183–190

[47] W.H. PRESS, S.A. TEUKOLSKY, W.T. VETTERING & B.P. FLANNERY, *Numerical Recipes—The Art of Scientific Computation, Third Edition. (New York, NY, U.S.A.: Cambridge University Press) 2007.*

[48] ALBERT RICH, *Derive User Manual (Version 3).* (Soft Warehouse, Inc., Honolulu, Hawaii) 1995.

[49] T. RODIC & D.R.J. OWEN, A plasticity theory of friction and joint elements. In: *Computational Plasticity: Fundamentals and Applications* [Proceedings of the second international conference held in Barcelona, Spain.] (Swansea, U.K.: Pineridge Press) 1989.

[50] J. RONDA, O. MAHRENHOLTZ, M. BRZOZOWSKI & R. BOGACZ, The rolling contact problem for an elastic-plastic strip and a rigid roller. *Mechanics Research Communications* **13** (1986) 119–132.

[51] J. RONDA, Friction in nonstationary contact problems. (In Polish). Habilatation thesis, Reports of the Institute of Fundamental Technology 1/1990 (Warsaw: IPPT PAN) 1990.

[52] J. RONDA, R. BOGACZ & M. BRZOZOWSKI, Infinitesimal and large strain in rolling contact problems. *Ingenier-Archiv* **56** (1986) 241–253.

[53] J. RONDA & K.W. COLVILLE, Influence of friction models on nonstationary contact problems solution. In: *Computational Plasticity: Fundamentals and Applications,* Proceedings of the third international conference held in Barcelona, Spain. (Swansea, U.K.: Pineridge Press) 1993.

[54] J. RONDA & K.W. COLVILLE, Modelling of friction phenomena in plastic working. Presented at FEMSA93, the Twelfth Symposium on Finite Elements in South Africa, University of Pretoria, 7–9 July 1993.

[55] RONDA, J. AND K.W. COLVILLE, Comparison of friction models for deep-drawing, *GAMM-Mitteilungen* **18** (1995) 9–59.

[56] J. RONDA, C.D. MERCER, A.S. BOTHMA, G.J. OLIVER & K.W. COLVILLE, Simulation of square cup deep drawing with various friction and material models. Presented at NUMISHEET '93, the Second International Conference on Numerical Simulation of 3-D Sheet Metal Forming Processes, Isehara, Japan, 31 August – 2 September 1993.

[57] RONDA, J. AND MERCER, C.D. AND BOTHMA, A.S. AND COLVILLE, K.W., Simulation of square cup deep drawing with various friction and material models. Ed.: Makinouchi, A. and Nakamachi, E. and Onate, E. and Wagoner, R.H. *Proceedings of NUMISHEET '93* (1993) 85–95.

[58] RONDA, J. AND COLVILLE, K.W. AND MROZ, Z., Co-rotational friction model for metal forming. Ed.: Lee, J.K. and Kinzel, G.L. and Wagoner, R.H. *Proceedings of NUMISHEET '96* (1996) 47–54.

[59] J.A. SCHEY, *Tribology in Metalworking: Friction, Lubrication and Wear.* (Metals Park, OH: American Society for Metals) 1983.

[60] H. SHIM & E. SUH, Contact treatment algorithm for the trimmed NURBS surface. *Journal of Materials Processing Technology* **104** (2000) 200–206.

[61] W. SOSNOWSKI, E. OÑATE & C. AGELET DE SARACIBAR, *Numerical Simulation of Industrial Sheet Forming Processes, Part I: Description of the Experiments.* International Center for Numerical Methods in Engineering, Barcelona, Spain. Technical report, May 1992.

[62] ALBERT TARANTOLA, *Inverse Problem Theory.* (Society for Industrial and Applied Mathematics) 2005.

[63] E.A. DE SOUZA NETO, K. HASHIMOTO, DJORDJE PERIĆ, D.R.J. OWEN, A phenomenological model for frictional contact of coated steel sheets. *Journal of Materials Processing Technology* **50** (1995) 252–263.

[64] E.A. DE SOUZA NETO, K. HASHIMOTO, DJORDJE PERIĆ, D.R.J. OWEN, A Phenomenological Model for Frictional Contact Accounting for Wear Effects *Philosophical Transactions of The Royal Society A Mathematical Physical and Engineering Sciences* **354** (1996) 819–843.

[65] D. TABOR, Friction, surface science and tribology—a personal view. *Journal of Mechanical Engineering Science* **205** (1991) 365–378.

[66] HAMID REZA TAMADDON-JAHROMI, NEERAJ KAVAN CHAKSHU, IGOR SAZONOV, LLION M. EVANS, HYWEL THOMAS, PERUMAL NITHIARASU Data-driven inverse modelling through neural network (deep learning) and computational heat transfer *Computer Methods in Applied Mechanics and Engineering* ***369***. (2020)

[67] TRIANTAFYLLIDIS, N. AND MAKER, B. AND SAMANTA, S.K., An analysis of drawbeads in sheet metal forming: part I—problem formulation. *Journal of Engineering Materials and Technology* **108** (1986) 321–327.

[68] TRIANTAFYLLIDIS, N. AND MAKER, B. AND SAMANTA, S.K., An analysis of drawbeads in sheet metal forming: part II. *Journal of Engineering Materials and Technology* **109** (1987) 164–170.

[69] J.H. TRIP, Surface roughness effects in hydrodynamic lubrication: the flow factor method. *Journal of Lubrication Technology* **101** (1983) 458–465.

[70] W.R.D WILSON, Friction models for metalforming in the boundary lubrication regime. *Journal of Engineering Materials and Technology* **113** 1 (1991) 60–68.

[71] W.R.D WILSON, Mixed lubrication in metal forming. In: *Advanced Technology of Plasticity 1990,* volume 4. (Japanese Society of Technical Plasticity) 1990, pp1667–1675.

[72] W.R.D. WILSON, T.C. HSU & X.B. HUANG, A realistic friction model for computer simulation of sheet metal forming processes. Unpublished preprint (1992).

[73] W.R.D. WILSON & S. SHEU, Real area of contact and boundary friction in metal forming. *International Journal of Mechanical Sciences* **30** (1988) 475–489.

[74] W.R.D. WILSON & J.J. WANG, Hydrodynamic lubrication in simple stretch forming processes. *Journal of Tribology* **106** (1984) 70–77.

[75] K.L. WOO & T.R. THOMAS, Contact of rough surfaces: a review of experimental works. *Wear* **58** (1980) 331–340.

[76] P. WRIGGERS, T. VU VAN & E. STEIN, Finite element formulation of large deformation impact-contact problems with friction. *Computers & Structures* **37** 3 (1990) 319–331.

[77] V.A. YASTREBOV *Numerical Methods in Contact Mechanics.* (ISTE/Wiley) 2013.

[78] J. ZHANG, F.A. MOSLEHY & S.L. RICE, A model for friction in quasi-steady-state sliding. Part I: Derivation. *Wear* **149** (1991) 1–12.

[79] J. ZHANG, F.A. MOSLEHY & S.L. RICE, A model for friction in quasi-steady-state sliding. Part II: Numerical results and discussion. *Wear* **149** (1991) 13–25.

Notation

n_I	unit normal at contact point
p_I	surface traction
p_{N}	contact pressure
$p_{\mathrm{T}I}$, p_α	friction stress vector
S_{IJ}	2nd Piola-Kirchoff stress tensor
u_I	displacement in Lagrangian frame
u_{N}	displacement normal to surface
$u_{\mathrm{T}I}$, u_α	displacement in contact plane = frictional sliding
$\dot{u}_\alpha$	rate of frictional sliding
$\dot{u}_\alpha^{\mathrm{ad}}$	rate of elastic adhesive state sliding
$\dot{u}_\alpha^{\mathrm{sl}}$	rate of frictional slip (non-recoverable sliding)
k_{T}	tangential contact stiffness constant
γ	magnitude of slip
Ψ	slip potential function
Φ	slip yield function
μ	coefficient of friction (c.o.f.)
α, β, ν	parameters of the WVS model
ω	density of frictional work
$\mu(\omega)$	friction function of WH model

δ_{IJ}	identity tensor
ρ_0	density of material at $t = 0$
$\rho_0 t_I$	body forces
$\rho_0 f_I$	inertia forces
E_{IJ}	Green-Lagrange strain
$\mathbf{L}^{\mathrm{EP}}_{KLMN}$	elastic-plastic hyper-operator
${}^t\Omega$	body at time t
${}^t\Gamma$	surface of body at time t
${}^t\Gamma_U$	surface subject to displacement boundary conditions
$\phi(\mathbf{X}, t)$	prescribed displacement boundary condition
${}^t\Gamma_F$	surface subject to force boundary conditions
G_I	prescribed force boundary condition
${}^t\Gamma_C$	contact surface subject to friction
T_{T_i}	frictional stress, also p_α
$\boldsymbol{\varepsilon}$	strain

List of Figures

List of Tables